TECHNISCHE UNIVERSITÄT WIEN
Vienna University of Technology

DIPLOMARBEIT

Investigation of the Front Contact Grid on GaAs Wafers as a Cap of III-V/Si Tandem Solar Cells by Low Cost Processes

Ausgeführt am

Atominstitut

Der Technischen Universität Wien

unter Betreuung von

Ao.Univ.Prof. Dipl.-Ing. Dr.techn. Johann Summhammer

und durchgeführt bei

Dr. Roman Tratting

Am Materials-Institut von JOANNEUM RESEARCH Forschungsgesellschaft mbH

durch

Saiedeh Kheirkhah

Matr.Nr.01229713

Mengergasse 56/7

1210 Wien

AUSTRIA

Wien, am 3.Juni 2019 ----------

Table of contents

Abstract

Many different solar cell technologies have been developed over the last years, all aiming to improve efficiency in energy conversion, while reducing material expense and cost of production, which is difficult task to fulfil. In order to gain this goal, the SiTaSol project explores to increase the efficiency of inexpensive c-Si solar cells up to 30% by integrating III-V semiconductors as top absorbers.

The aim of this thesis is to investigate the metallization of front contact solar cells by low cost deposition methods like inkjet and spin-coating. The copper nanoparticles ink was printed on different substrate such as glass, GaAs and Si. Afterwards were examined the sintering of printed copper nanoparticles ink by using a laser as a high speeds sintering technique. The resistivity of sintered structures was measured and plotted to determine the sheet resistance and contact resistance in the GaAs and Si substrate. Therefore, this work presents experimental investigation of the sintering processing window of pico-second pulsed Nd-YAG laser. The dependence of processing window on Cu layer thickness, different substrates and laser exposure duration has also been studied. This study indicated that, the higher thickness of printed copper NPs enabled to obtain the lower contact resistance and the sintering process under higher laser power with higher exposure time (lower scan speed) decreased the resistivity obviously and caused superior outcomes.

In addition, the behavior of pure Copper and Silver, which were deposited with electron-beam physical vapor deposition (EBPVD) technique on GaAs was surveyed to demonstrate the possibility of ohmic contact of copper and silver on two types of GaAs substrate. Furthermore, to improve the contact resistance and adhesion of copper some post processing and surface treatment were done. Various measurements were shown, the lowest contact resistance was gained between pure deposited copper and high doped GaAs (Azur) without post annealing. Also it was indicated that, the copper is the better candidate for these types of GaAs wafers to obtain the ohmic contact with the low resistivity.

1. Introduction

Thesis Motivation

As the title:" investigation the front contact grid on GaAs wafers as a cap of tandem solar cells by low cost processes" indicates, this thesis addresses the field of renewable energy resources which is one of today's major challenges of humankind to maintain a world, worth living in for next generations. With the growing energy demand and the need for new and clean energy resources, solar power is experiencing remarkable growth throughout the world. Never before we have seen more solar power being installed in a single year than in 2016 [1]. The global solar PV market grew much more than expected – by 50% to 76.6 GW year-on-year. While all these solar growth numbers sound very impressive, the fact is that solar still has a long way to go to fully tap its potential. The 306.5 GW of grid-connected PV capacity installed end of 2016 generated around 2% of the world's electricity demand. From today's perspective, we expect total global installed PV capacity to exceed 400 GW in 2018, 500 GW in 2019, 600 GW in 2020 and 700 GW in 2021. [1]. To ensure that solar power can be a sustainable solution to the growing energy demand for future, innovative ways are being explored to increase the overall PV installations. These provide new possibilities of generating solar power, however, the generated energy needs to be affordable as well. Significant research is being conducted to make solar cells more efficient and thereby reduce the cost per unit of solar energy [2]. To render solar cell technology economically competitive, the manufacturing costs of PV must be reduced to reach comparable values as for other energy sources, like gas, biogas, wind, water, nuclear power as well as brown and hard coal. Solar cell module costs can be divided into 40% for the module manufacturing process, 40% for the wafer and 20% for the solar cell technology [3]. Reduce further the solar cell panel cost ($/Wp) (dollar/watt peak) become harder and harder with conventional crystalline silicon PV technology. The highest impact on cost can be achieved by increasing the efficiency of the solar cell with using high quality material and reducing the wafer thickness at the same time. Among various other possibilities to decrease the cost of solar cells is optimization of solar cell metallization, since in the manufacturing of solar cell, metallization is the second most expensive step in the fabrication of a solar cell [4], therefore utilizing the low cost fabrication technology con play a main role in solar cells industry. The research goal of this thesis is the development of up-scalable low cost non-lithographic processes for the front contact grid of the Tandem Solar cells. Such processes include ink-jet and spin- coating techniques. One of the major challenges in such fabrication processes is to obtain an ohmic contact between the metal and the semiconductor while keeping the contact resistance of the electrodes less than 1 Ohm cm^2.

2. Background

This thesis is about Tandem (multijunction) solar cells with Two-Terminal III-V Si Triple Junctions. In this chapter the working of basic solar cell, I-V curves and losses are explained. Furthermore, a detailed description of multijunction solar cell, metallization process and Metal-Semiconductor contact are described.

2.1 Fundamentals

A solar cell or photovoltaic cell is a device that directly transforms electromagnetic radiation into electrical energy without any thermal cycles, mechanical cycles or chemical reactions [5]. Solar cells perform this feat by means of a very specific phenomenon, the so-called photovoltaic effect. A typical industrial solar cell structure fabricated on p-type crystalline silicon is illustrated in Fig.2.1. This solar cell is in principle a large-area diode with a relatively thin n-doped emitter and a thick p-doped base substrate. Between the n-doped emitter and the p-doped base a space-charge region is formed. The emitter is located on the irradiated side. Electron-hole pairs are generated under irradiation. The minority carriers diffuse to the space charge region and reach the other region. The minority carriers become majority carriers, which reduces the recombination probability dramatically. [6]

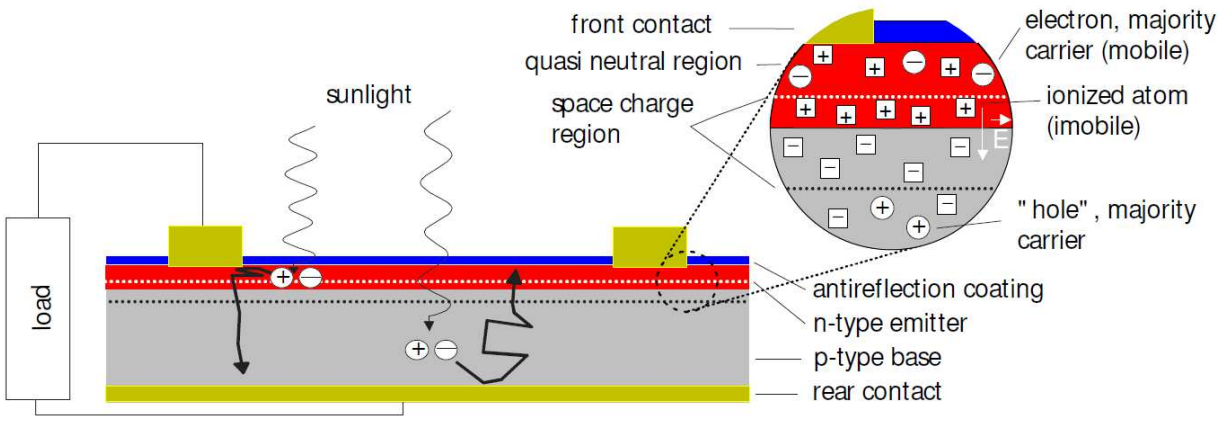

Fig.2.1: Schematic drawing of a solar cell. Created electron-hole pairs are separated by the electric field of the space charge region and extracted at the metal contacts. The enlarged section illustrates the p-n-junction. While the space charge region can be regarded as carrier-free, majority carriers are electrons in the n-region and "holes" in the p-region.

The photon-generated current flow can be extracted at the front and rear side contacts via an external load. The rear contact usually covers the whole rear side, whereas the front contact is made up of a fine metal mesh to reduce shading losses. To further reduce optical losses on the front side, the emitter surface is textured and an antireflection coating is applied. [6]

2.1.1 Photovoltaic Technologies

At present, materials used for photovoltaic cells are monocrystalline silicon, polycrystalline silicon, amorphous silicon, cadmium telluride and copper indium gallium selenide. [7] Fig.2.2 provides how different types of solar cells are constructed. In this study is presented the metallization of multijunction (III-V Si Triple Junctions) solar cells, which are considered as thin film solar cells generation with significantly enhanced efficiencies by overcoming partly the limitation of single-bandgap devices and using the ideal band gaps.

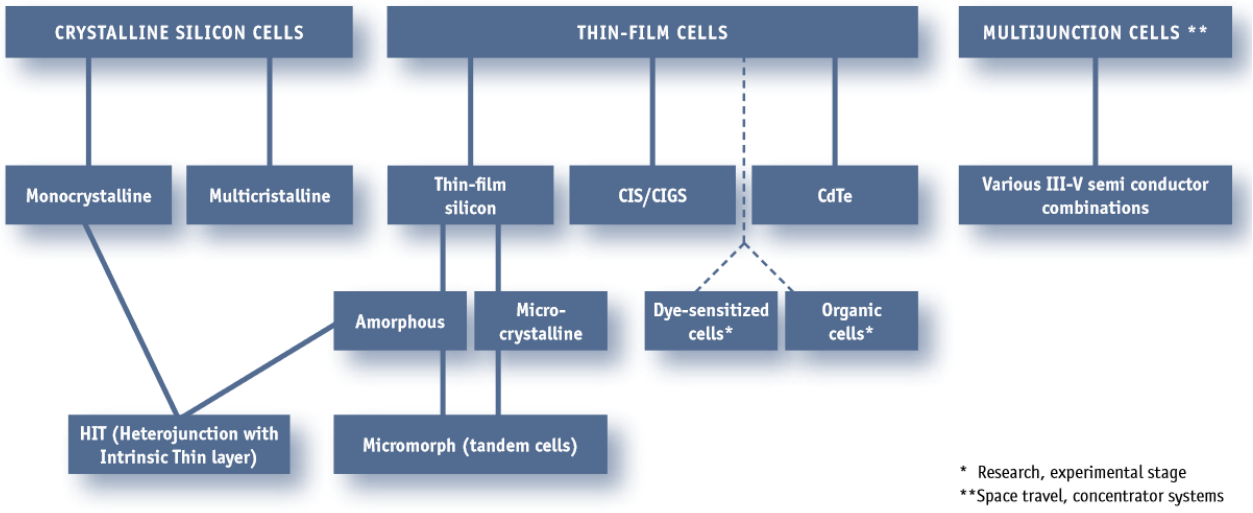

Fig. 2.2: Types of solar cell [8]

2.1.2 Solar Cell Optimum Bandgap

In order to create electron-hole pairs in a semiconductor material exposed to light, the photons involved need to have an energy greater than the bandgap energy of the semiconductor.

The photons with energies lower than the bandgap will not be absorbed (in fact, they can be absorbed by other processes, such as free carrier absorption, but will not contribute to the photovoltaic effect). Since they do not have energy enough to promote the jump between the valence and conduction bands and all intermediate energy levels are forbidden. In other words, the bandgap represents the minimum energy that can be absorbed from a photon to produce a free carrier for conduction. It could be thought that the optimum bandgap of a solar cell should be small in order to maximize photon absorption. This is not the case, the reason behind that discrepancy is that the bandgap not only determines the number of excited charge carriers (by modulating photon absorption) but also the potential energy that those excited carriers have as compared to their ground state [9]. The key phenomenon behind this process is called *thermalization*. In essence, thermalization means that no matter how high the energy of the absorbed photon is, the resulting excited charge carrier will quickly relax to the base energy level at the band edge losing the excess energy in the form of heat [9]. In other words, the excited carriers cool down fast (within femtoseconds) to an energy level in which they can live stably for much longer times; the relevant energy level for electrons is the bottom of the conduction band and for holes the top of the valence band. Therefore, after a few femtoseconds, excited carriers produced by a very high energy photon are indistinguishable (energy-wise) from excited carriers produced by a photon with the energy of the bandgap. They all form a population of excited carriers with an average potential energy very close to the bandgap energy.[2] Accordingly, the bandgap defines a second key consequence in terms of solar cell efficiency as it determines the potential energy of the charge carriers produced by each absorbed photon [9].

So, in summary, low bandgap materials can absorb most photons in the solar spectrum (providing a large number of excited charge carriers) but the potential energy per charge carrier is low. On the other hand, high bandgap semiconductors will only absorb the high energy photons in the solar spectrum (providing a small number of excited charge carriers); but after thermalization, the potential energy per charge carrier is high. Therefore, for a given spectral distribution, there must be an optimum bandgap energy. On earth this optimum bandgap energy is Eg~1.3 eV and represents the band gap energy where the product of the number of generated carriers and energy per carrier is maximized [9].

2.1.3 Basic Solar Cell I-V Curve

The voltage and current levels at which this power is delivered depend on the current–voltage characteristic or *I-V* curve of the solar cell and that of the load. The *I-V* curve of several solar cells under illumination are schematically depicted in Fig.2.3 Each of these curves has three characteristic points which are:

1- the short circuit current (I_{sc}) which is the current produced by the solar cell at zero voltage

2- the open circuit voltage (V_{oc}) which is the voltage produced by the solar cell at zero current

3- the maximum power point or MPP ($P_{mpp}=V_{mpp} \times I_{mpp}$) which is the point at which the power delivered by the solar cell is maximum.

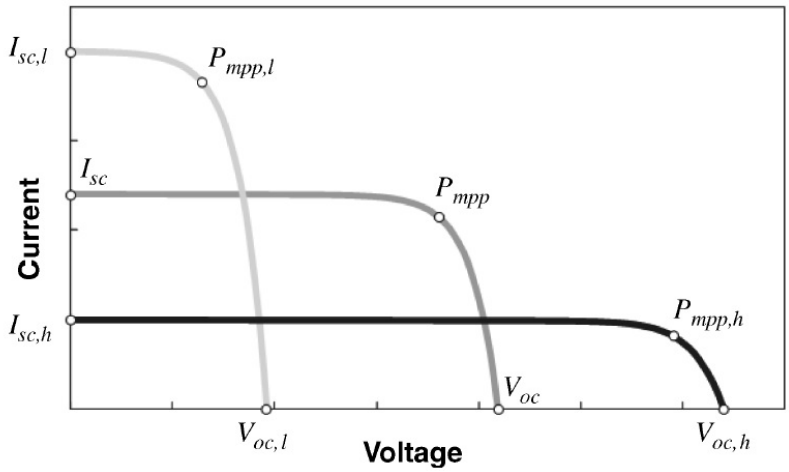

Fig. 2.3 Solar cell I-V curves for three devices made with semiconductors of different bandgaps, namely, low bandgap (light grey); medium bandgap (dark grey); and high bandgap (black)[5].

As in Fig.3.2 shown, it is straightforward to see that:

1- the *I-V* curve of three solar cells made of different semiconductor materials with different bandgaps: the lower the bandgap results in a larger the short circuit current ($I_{sc,l} > I_{sc} > I_{sc,h}$) since more photons are absorbed in low bandgap materials

2- the higher bandgap results in a larger the open circuit voltage ($V_{oc,h} > V_{oc} > V_{oc,l}$) since V_{oc} is closely related to the bandgap and thus is a measure of the potential energy of the photogenerated carriers.

2.1.4 Loss Mechanisms in Solar Cells

The maximum efficiency attainable by a single junction solar cell is 30.1% [10]. The main sources of losses in solar cells are defined as below:

1- Physical and technological losses:

1-1 Absorption losses: photons with energy below the bandgap will be lost, in other words, Photons with energy smaller than the band gap cannot generate an electron-hole pair.

1-2 Thermalization losses: the excess energy of photons above the bandgap is lost in the form of heat.

1-3*Recombination losses: The maximum achievable open-circuit voltage is far below the bandgap, since not the separation of the band gap but only the separation of the quasi-Fermi levels defines the maximum achievable voltage (The excited carriers can find ways to release their extra energy and return to the ground state before they reach the solar cell contacts, therefore no power can be delivered to the external load and the extra energy is internally dissipated in the form of light (a photon or heat)).

1-4 Fill factor losses: The maximum power that can be collected from a solar cell is not equal to the product of open-circuit voltage and short-circuit current density, as the current depends exponentially on the voltage, the IV-curve has not a rectangular characteristic. This limits the fill factor to about 85% due to non-avoidable recombination currents.

2- Optical losses:

2-1 Reflection losses: Loss due to the reflection of the light incident at the front surface. In addition, the antireflection coating on the surface will not be perfect for all wavelengths, generating also some undesired reflections in non-metallized areas.

2-2 Shading losses: Loss due to the coverage of front surface with the contact metal.

2-3 Loss due to the escape of photons from the cell (incomplete absorption) due to the limited solar cell thickness.

3- Electrical losses. As a result of current flowing through semiconductor and metal layers of limited conductivity of front and back contact.

---

*Recombination mechanisms occur in a semiconductor in different ways:1- radiative recombination. 2-Auger recombination. 3- recombination via recombination centers in the bulk. 4- via surface states.

All losses mechanisms in solar cells and their solutions are indicated in Fig.2.4.

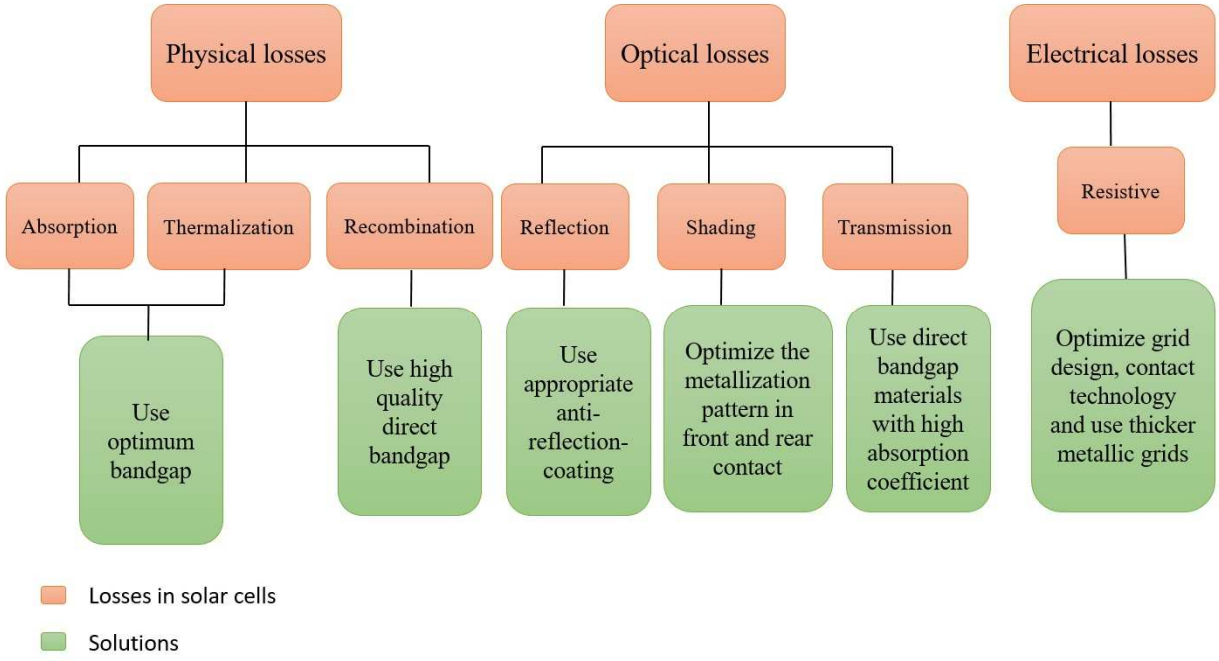

Fig.2.4. losses mechanisms in solar cells and their solutions

Since this thesis deals with the improvement of the front side metallization of tandem solar cells a detailed presentation of multijunction solar cells with focus on the front side metallization process to reduce all losses is needed. As in above chart is demonstrated, metallization plays both optical and electrical roles in the performance of a solar cell. Optically, the gridline width and shape contributes to shading, which impacts the short circuit current and electrically, the series resistance of metal grid lines and the contact resistance between grid lines and semiconductor, which influences the fill factor. It should be noted that, in this work only the reduction of electrical losses is considered.

2.2 Multijunction Solar Cells

2.2.1 Why III-V Multijunction Solar Cells?

Multijunction solar cells are currently favoured over single junction cells as they are more efficient and have a lower temperature coefficient (less loss in efficiency with an increase in temperature). [11]

Multijunction solar cells built from III–V semiconductors are being evaluated globally in CPV (concentrating photovoltaics) systems. The bandgaps of the binary III-V semiconductors are conveniently scattered around the solar spectrum with further bandgap tuning possible through alloys of group III and V elements [12]. The majority of III-V materials have direct bandgaps, leading simultaneously to large absorption coefficients.

For photons with energies in excess of the bandgap and short radiative lifetimes (ns). The III-V semiconductor family covers the ultraviolet, visible and infrared wavelengths offering the possibility to efficiently absorb the broad solar spectrum [12].

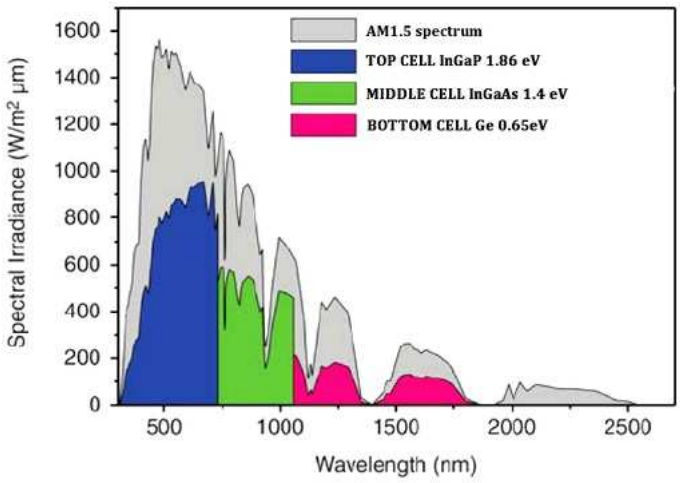

Figure 2.5. spectral response of triple junction GaInP/InGaAs/Ge.[12]

In designing multijunction solar cells, two or more semiconducting layers are stacked as p–n junctions to collect light. These cells as semiconductors with different band gaps can harvest more of the solar spectrum.

2.2.2 Fabrication Multijunction Solar Cells

In general, Multijunction solar cells are fabricated monolithically, meaning that the semiconductor (n-p) junctions are epitaxially-grown one upon another [13]. A typical 3-junction solar cell structure comprises three n–p junctions made from GaInP, GaInAs and Ge stacked on top of each other—each layer with a band gap energy higher than the layer below it—and assembled with low resistive tunnel junctions. These junctions are formed on a substrate by epitaxial growth techniques to produce a series-connected, monolithically grown, GaInP/GaInAs/Ge stack. The top p–n junction has the highest band gap energy that collects light from the shortest wavelengths in the solar spectrum. Photons with energy lower than the band gap pass to the lower junction, and photons with energy lower than this threshold traverse to the lowest junction in the stack. (see Fig.2.6)

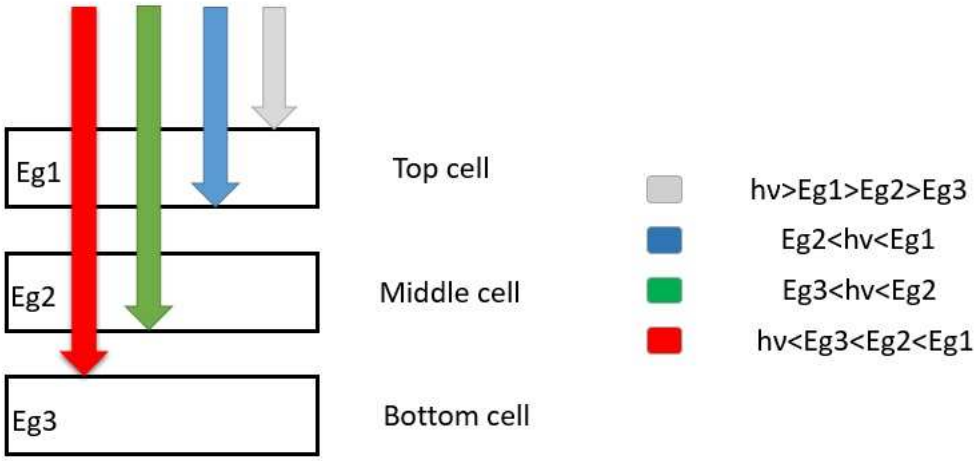

Fig.2.6. simplified schematic of a three-bandgap tandem solar cell. The bandgap of each cell decreases from the front to the back, giving both spectrum splitting and photon selectivity.

Challenges

To fabricate a monolithic device, there are four main material requirement challenges to implement such structures:

1. The semiconductor materials needed for the different subcells have to be structurally compatible, so that they can be grown in the same epitaxial process [9].

2. High material quality of layers is necessary for minority carrier electrons and holes to be collected efficiently [13].

3. Since the subcells in the stack are connected in series they should be designed to produce the same current, or in other words, they should be *current-matched*. (In two terminal devices, the voltage of cells adds in series, the devices being designed to carry the same value of current in order to avoid the problem of internally circulating currents) [9].

4. Wide ranges in doping levels must be attainable and controllable, since the device is monolithic, it is necessary to interconnect each sub-junction in the stack which requires layers to reserve the n–p polarity between the subcells*, these layers are tunnel-junctions which act as diodes hooked up in reverse polarity to the original configuration of the stack. They allow tunnelling of carriers through the junction so that current is transported vertically through the device [13].

Epitaxy growth process

The p/n III-V solar cells are fabricated by epitaxial processes such as metal organic vapour phase epitaxy (MOVPE). Epitaxial techniques are very expensive but give very high quality crystalline material. Epitaxial growth requires control of the lattice parameter at a constant value and bandgap control is also required for a tandem cell.

The junctions can grow in different types, such as:

- Lattice- matched (maximum material quality but not optimum bandgap designing)
- Lattice – mismatched (produces dislocations in crystal structure, which lower minority-carrier lifetime and cell efficiency but flexible in bandgap selection)

* if a P/N and second p/n junction were put together to make P/N/p/n. there would be an intermediate N/p junction and that would generate a voltage opposite to the other junction and this would be problem. increasing the impurity (called doping) concentration until the N and p layer would become metallic. This would create P/N N+/p+ p/n structure when the intermediate voltage is reduced to zero. This N+/p+ junction is really called a tunnel junction.

2.2.3 Multijunction Subcells Modelling

As in Fig 2.7. (a) illustrated most multijunction III-V solar cells consist of sub cells, which are described as below:

1- Window layer: a window layer is used in order to reduce the surface recombination velocity. In addition, the window layer should be largely transparent to the light (that is why it is called a window) that would be absorbed by the underlying p-n junction. The choice of material for the window layer is often limited and different from silicon solar cells, so that usually high-bandgap and preferably indirect materials lattice matched to the p-n junction material are used. ($E_{g\ window} > E_{g\ emitter}$)

2- Emitter and base layers: since Light is incident through a thin emitter layer and absorbed completely in the base, the doping of the emitter layer is usually an order of magnitude higher than the base and correspondingly has a shorter diffusion length; the optimum thicknesses of the layers depends upon the diffusion length and photogeneration in each layer

3- back surface field (BSF) layer: BSF is used to decrease the scattering of carriers towards the tunnel junction and Minority carrier diffusion towards the substrate, thus a back surface field (BSF) is often employed, usually via a doping gradient or sometimes using a wide-bandgap heterostucture [12]. The BSF should be transparent for the light that needs to reach the underlying subcells. ($E_{g\ BSF} > E_{g\ emitter}$)

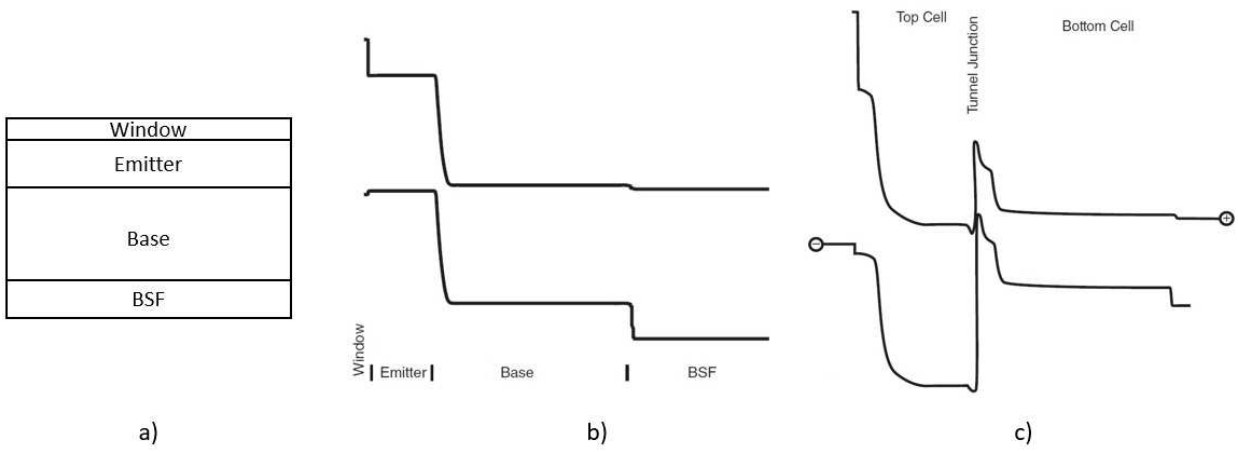

Fig.2.7. (a) Layer structure for a p/n subcell of tandem solar cells, (b) its associated band diagram drawn under short-circuit conditions (V = 0) and (c) is an example diagram of double junction solar cell

Multijunction Electrical Subcells Modelling (Single Diode)

According to what has been described about multijunction, to mathematically explain the schematic representation of Fig.2.8. (a). can be transformed into the equivalent circuit as shown in Fig.2.8. (b)

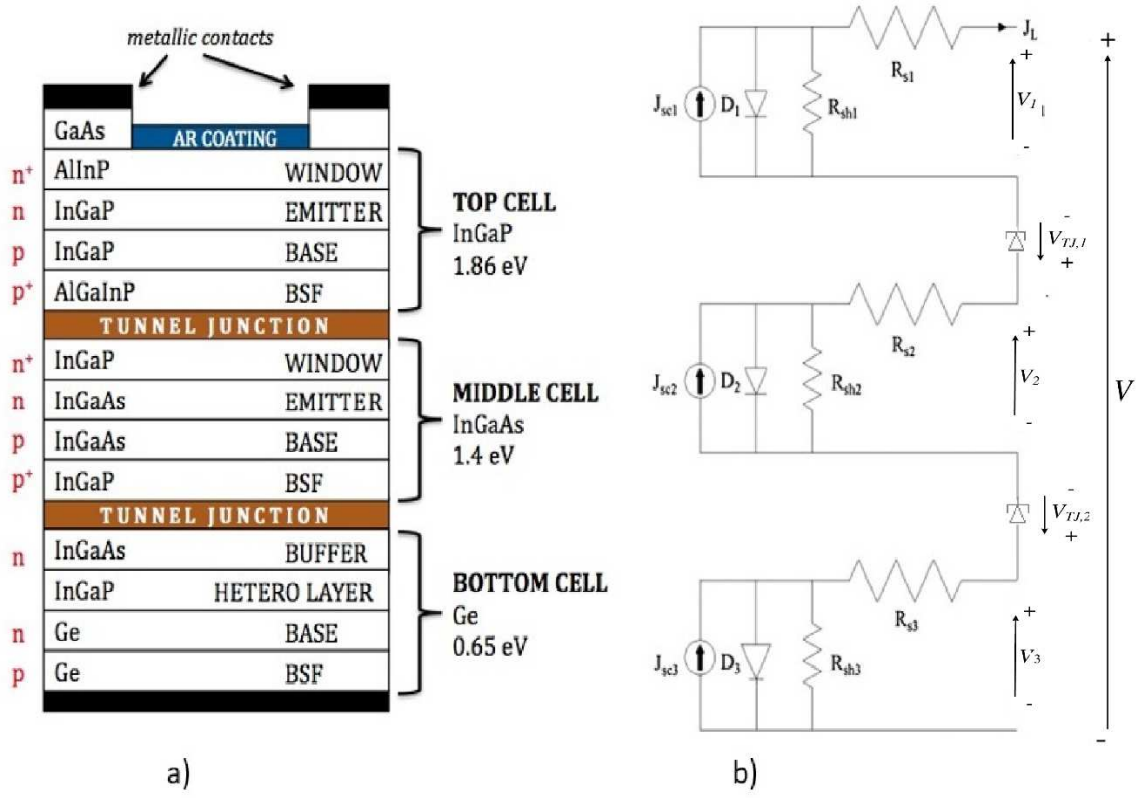

Fig .2.8. (a) layer structure of triple GaInP/GaAs/Ge, (b) equivalent circuit of a real triple junction solar cell

Equivalent Circuit Models

A two-terminal equivalent circuit model for a triple-junction cell with a single-diode for each junction is given by:

$$J_L = J_{sc,i} - J_{0,i}\left(e^{\frac{q(V_i + J_L A R_{s,i})}{n_i k_B T}} - 1\right) - \frac{V + J_L A R_{s,i}}{A R_{sh,i}} \qquad (2\text{-}1)$$

Where i represents the subcell number (1=top, 2=medium and 3=bottom). J_{sc}, J_0 and J_L are the short circuit, the diode reverse saturation and the load current densities (currents per unit cell area), respectively. q is the electric charge (1.602×10^{-19} coulombs), V is the voltage (v), n is the diode ideality factor (typically between 1 and 2), k_B is Boltzmann's constant (1.38×10^{-23} J/K), T is the absolute temperature (kelvin) and A is the cell area (cm^2).

R_s and R_{sh} are the series and the shunt resistances, respectively. It is assumed that the cell temperature is uniform.

The reverse saturation current is strongly temperature dependent and is given by:

$$J_{0,i} = k_i T^{(3+\frac{\gamma_i}{2})} e^{(\frac{-E_g}{n_i K_B T})} \quad (2\text{-}2)$$

where E_g is the energy band gap and k and γ are constants where g is typically between 0 and 2[14].

In Eq. (2-1) the reverse saturation current is modelled by a single term, it represents recombination in both the depletion and the quasi-neutral regions. If the shunt resistance is sufficiently large to be neglected, the single-junction voltage can be extracted from Eq. (2-1) as follows:

$$V=\sum_{i=1}^{3} Vi \quad (2\text{-}3)$$

$$V_i = \frac{niK_BT}{q} \ln(\frac{Jsc,i-Jl}{J0,i} + 1) - J_l A R_{s,i} \quad (2\text{-}4)$$

Rearranging Eq. (2-3) we get:

$$V= K_BT[n_1 ln(\frac{Jsc,1-Jl}{J0,1} + 1) + n_2 ln(\frac{Jsc,2-Jl}{J0,2} + 1) + n_3 ln(\frac{Jsc,3-Jl}{J0,3} + 1)] \quad (2\text{-}5)$$

The total series resistance is $R_s=R_{s,1}+R_{s,2}+R_{s,3}$. The tunnel diodes located between the subcells are modelled as resistors as part of R_s [14]. The open circuit voltage is obtained by setting $J_L=0$

$$V_{oc} = K_BT [n_1 ln(\frac{Jsc,1}{J0,1} + 1) + n_2 ln(\frac{Jsc,2}{J0,2} + 1) + n_3 ln(\frac{Jsc,3}{J0,3} + 1)] \quad (2\text{-}6)$$

The maximum power point (MPP) is obtained by setting $dP/dJ_L=0$ where the power is, $P=J_LVA$. The resulting equation is:

$$\frac{K_B T}{q}[n_1 ln(\frac{Jsc,1-Jl}{J0,1} + 1) + n_2 ln(\frac{Jsc,2-Jl}{J0,2} + 1) + n_3 ln(\frac{Jsc,3-Jl}{J0,3} + 1)]- J_l[\frac{K_BT}{q}(\frac{n1}{Jsc,1-Jl+J0,1} + \frac{n2}{Jsc,2-Jl+J0,2} + \frac{n3}{Jsc,3-Jl+J0,3}) + 2AR_s] =0 \quad (2\text{-}7)$$

This has to be solved numerically for the current at the MPP, J_m. The voltage at the MPP, V_m is then obtained by substituting $J_L=J_m$ in Eq. (2-7). The single-diode model contains 10 empirical parameters that need to be determined by calibration against experimentally measured data: k_i, γ_i, n_i and R_s [14].

As the device junctions are connected in series, the voltages of the diodes add up and the current is clamped by the subcell that produces the lowest current in the string. Note that since the tunnel junctions are assembled in reverse polarity they subtract whatever amount of voltage drop there is across them from the total device voltage. This can be expressed as:

$$V_T = V_{tc} - V_{tj1} + V_{mc} - V_{tj2} + V_{bc}$$

therefore, it is necessary that tunnel junction voltage drops are minimized. In essence, the advantage for a monolithic multijunction with subcells connected in series is the gain in voltage but produces lower current [13].

The best combination of band gaps should be chosen to produce the optimum current in each subcell, and then the stacked p-n junctions would be connected by tunnel junctions. As we know, the current density of the subcell scales with the band gap, so lower current densities result from wider band gap materials, therefore the current produced within the Ge subcell is typically in excess by a factor of two than the upper junctions. Since it is the lowest band gap in the stack, the power from higher energy light that could be captured by a more optimal middle junction is lost and turned to heat [13]. In ideal case the tunnel junction must have high transparency when light is passing through the device from the upper to lower junction, it means that tunnel junction would be formed of materials with a band gap higher than upper subcell, which it is completely transparent to light passing through, but it is important to notice that wider band gap materials cannot be doped sufficiently high, as the peak tunnelling current is a direct function of doping, it is an engineering challenges to optimize peak tunnelling current ,transparency, and other parameters such as cost, reliability, and manufacturability.

2.2.4 Multijunction Solar Cell I-V Curve

As discussed about the equivalent circuit, now will be explained the J-V curve of a multijunction solar cell. Fig.2.9. represents the case of a lattice matched triple-junction GaInP/GaInAs/Ge solar cell including in the same graph the J-V curves of the individual subcells. In this design, as a result of the low bandgap of germanium, the bottom cell produces a lot more photogenerated current as compared to top and middle cells, which are normally fabricated to be current matched. The key benefit of multijunction solar cells is the subcell voltages are additive according to Kirchhoff's voltage law as illustrated in Fig.2.9., but the current is clamped by the subcell that produces the lowest current in the series subcells [13].

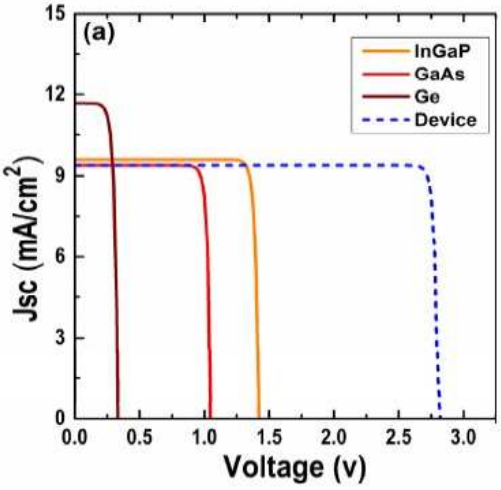

Figure.2.9. J-V curve of a lattice matched triple-junction GaInP/GaInAs/Ge solar cell [15].

2.3 Device Modelling

2.3.1 Wafer fabrication

In this study we used a 3-junction solar cell structure which comprises three n–p junctions made from GaInP, GaInAs and Si stacked with low resistive tunnel junctions.

Now the main question is that why we use Si as a bottom cell in this study?

1- Ge has a low bandgap energy of 0.66 eV hence Ge bottom cell produces a high excess current compared with the two upper subcells. The excess current cannot be used in the series-connected device as the current is limited by one of the upper cells [16].

2- the combination of GaInP/GaAs/Si is that the upper two subcells can be grown lattice matched on a GaAs substrate. This lattice-matched growth prevents the formation of dislocations and allows a high minority carrier lifetime. After the substrate removal by selective etching, the GaInP/GaAs stack is bonded to a separately prepared silicon bottom p-n junction [16].

3- Ge is an expensive material with limited availability in comparison to silicon with high availability.

The growth of III–V semiconductors on silicon is very difficult because:

1- The high thermal expansion coefficient mismatch leads to strain and may result in cracks and bowing [17].

2- The large lattice mismatch between Si and GaAs (~4%)creates dislocations and, thus, recombination centers [17].

3- The transition between nonpolar Si and polar III–V crystals induces antiphase domains [17].

Although the understanding and control of lattice- mismatched hetero-epitaxy has improved over the past years [18], III–V growth on Si remains challenging. Another attractive approach to overcome hetero-epitaxy issues consists in joining independently processed Si and III–V solar cells by bonding/gluing techniques [17].

In this study, we focus on a two-terminal configuration, which corresponds to the silicon module manufacturing standard and thus would be the best option for implementing silicon wafer- based tandem cells into existing PV module technology.

An overview of the fabrication process of our wafer-bonded GaInP/GaIn$_x$As/Si triple junction cells is presented in Fig.2.10:

(a) The GaInP/GaIn$_x$As top tandem cells were grown lattice matched with inverted layer direction on GaAs substrates using metal–organic vapour phase epitaxy. The silicon bottom cells were prepared independently.

(b) GaAs and Si wafers were then brought in contact with a force under high vacuum ambient (∼10−8mbar)

(c) The GaAs growth substrate is then etched away and the few-micrometres-thick GaInP/GaIn$_x$As top cells remain on the silicon bottom p-n diode. After this etching step, the silicon rear side was passivated.

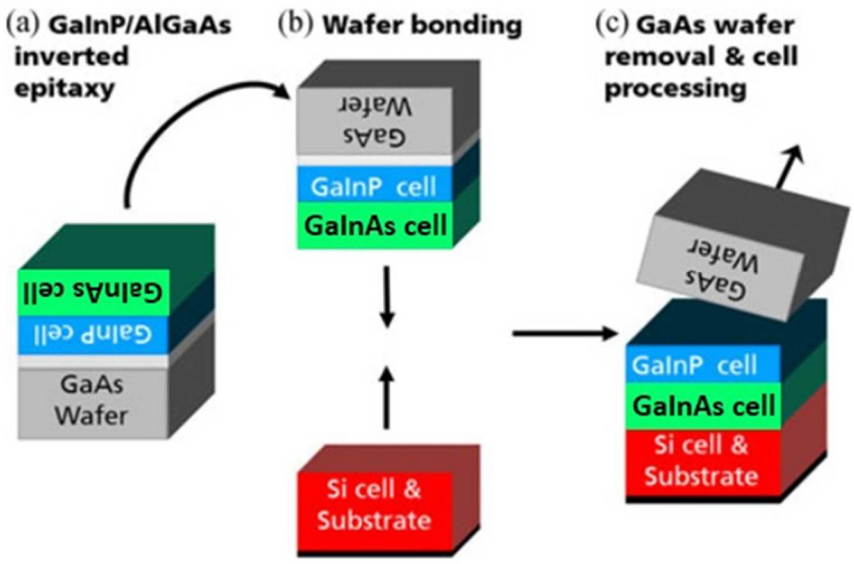

Fig.2.10. overview of the fabrication process of wafer-bonded GaInP/GaInxAs/Si to produce solar cells with Two-Terminal

2.3.2 Loss Mechanisms (Due to Front Side Metallization)

As previous mentioned a detailed presentation of only electrical losses due to the front side contacts is needed, optical losses will not be investigated. Finite element analysis may be used in determining electric field profiles and current flow within the many layers of a multijunction cell. As in Fig.2.11. depicted power losses due to series resistance occurs in three segments:

(1) Resistance in the semiconductor layers. (R_{Sem})

(2) Contact resistance at the semiconductor–metal interface. (R_c)

(3) Resistance in the metal gridlines. (R_m)

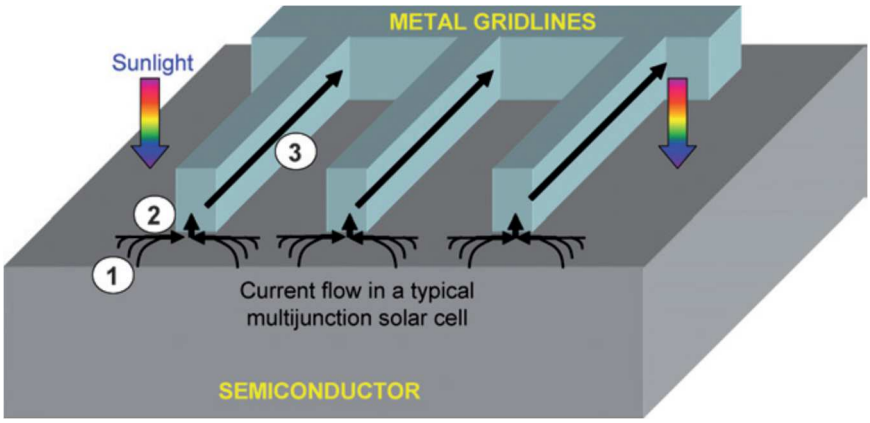

fig.2.11. Series resistance components of front contact solarcell [13].

Each of the three resistive loss mechanisms may be reduced by appropriate changes in the cell architecture. To reduce resistance in the semiconductor, for example, the emitter and window layer thicknesses as well as doping may be increased [13]. Similarly, the metal resistance (sheet resistance of metal) and contact resistance between metal and semiconductor have to be taken into consideration. So that multijunction solar cells (MJSC) require an ohmic contact or junction between the grid metallization and the underlying semiconductor.

2.3.3 Metal Semiconductor Contacts

For the front side metallization of industrial solar cells, the contact resistivity is very important. Whereas the resistivity for evaporated and lithographically produced contacts is low, the contact resistivity of industrial printing such as inkjet and screen printing solar cells is not negligible. Thus current flow mechanism and contact resistivity calculation of a metal- semiconductor will be presented briefly in this section. Conduction mechanism for metal-semiconductor contacts was explained by a potential barrier formed in 1938 by Schottky. This model is illustrated in Fig. 2.12. and is known as the Schottky barrier. The potential barrier Φ_B that is formed can be described for an n-type semiconductor by:

$$q\Phi_B = q\Phi_M - q\chi_S$$

with $q\Phi_M$ being the metal work function, representing the potential necessary to excite an electron from the Fermi level to the vacuum level and $q\chi$ the electron affinity defined as potential difference between the bottom of the conduction band and the vacuum level. V_{bi} is the built-in potential in the semiconductor, and V_n is the voltage between the bottom edge of the conduction band and the Fermi level.

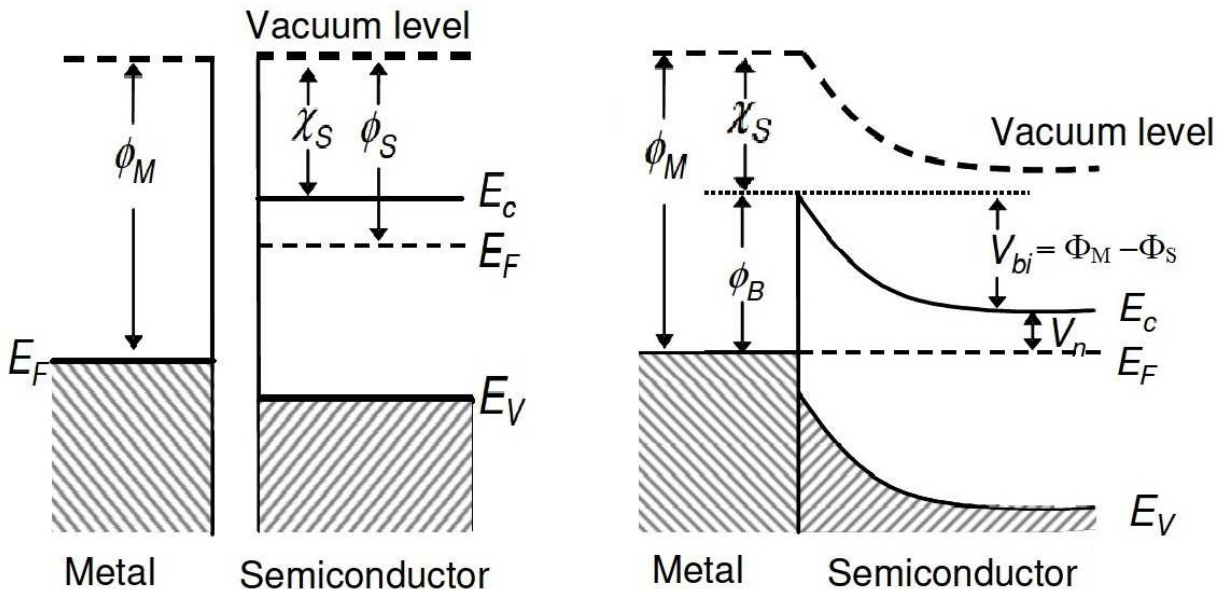

Fig. 2.12: Energy band diagram of a metal-semiconductor contact before and after bringing into intimate contact. The Schottky barrier height Φ_B is illustrated.

2.3.4 Current Flow Mechanism and Contact Resistance

The current flow over the metal-semiconductor contact is primarily defined by majority carriers and can be described by three processes (see Fig.2.13):

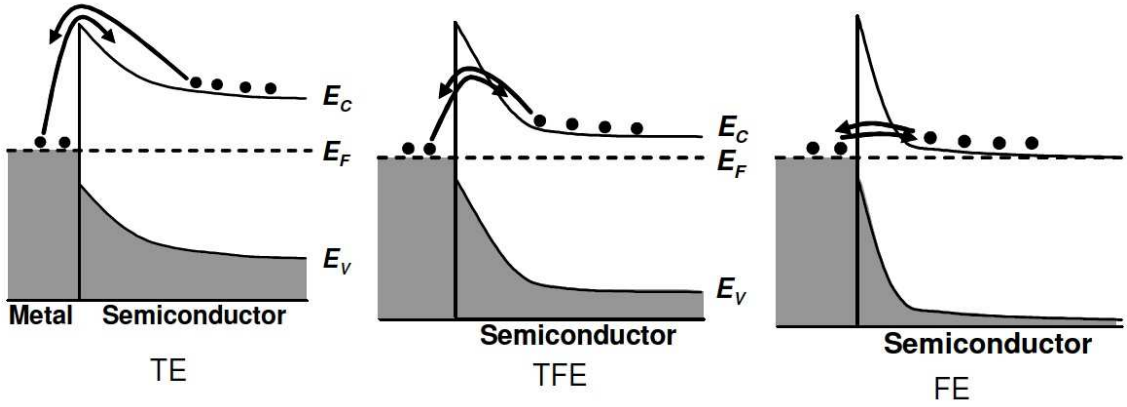

Fig. 2.13 : Current flow mechanism between metal and semiconductor. From left to right:thermionic emission (TE), thermionic field emission (TFE) and field emission (FE).

-Thermionic Emission (TE): The thermionic field emission theory assumes that the current crossing the metal semiconductor interface depends on the height of the potential barrier (Schottky barrier) [19]. Only electrons with energy greater than the barrier height contribute to the current transport.

- Field Emission (FE): For very low temperatures and/ or high doping concentration the current flow cannot be described by the thermionic emission model [6]. The transport mechanism has changed, so that by increasing doping concentration N_D and w width of the space charge region shrinks. At a doping concentration of $N_D \geq 10^{19}$ cm^{-3} the width of the space-charge region of the metal-semiconductor interface is strongly reduced, that the probability for quantum mechanical tunnelling is significant.

- Thermionic field emission (TFE): The thermionic field emission is a combination of the two previously described transport processes. The electrons are thermally activated, and the width w of the potential barrier is thin enough to allow quantum mechanical tunnelling.

To achieve minimal resistance across the metal -semiconductor (M-S) contact, the work function of the metal must be close to or smaller than the electron affinity of the semiconductor for an n-type semiconductor. While for a p-type semiconductor, it requires the work function of the metal to be close to or smaller than the sum of the electron affinity and the bandgap energy [19].

2.3.5 Ohmic Contacts on Multijunction Solar Cells

Most multijunction solar cells use GaAs as a capping layer since this material is lattice matched to many of the technologically important III–V binary and ternary compounds [13]. Formation of ohmic contacts to compound semiconductors (like GaAs) is considerably more difficult than with silicon or germanium due to the reactivity of their constituents and inter - diffusion with the metal [20]. When a metal and semiconductor are brought into contact, the atomic positions and the charge distributions of the surfaces in touch will change in an unknown way and additionally have some degree of surface interaction [20]. Therefore, cannot be expected to explain and predict barrier heights at such interfaces. In an attempt to overcome this problem, it was suggested that the electronegativity of the metal could be used to predict M-S contact performance, rather than its work function [21]. No definite explanation regarding the properties of M-S contacts has yet emerged [20]. This is likely due to the lack of detailed information on the nature of M-S contacts on the atomic level and differences in deposition techniques for contacts [20].

There are common techniques to make ohmic contacts on GaAs

- The key to achieving good quasi-ohmic behaviour is to dope the semiconductor substantially high. High doping will narrow the depletion region at the junction and allow electrons to flow easily in both directions at any potential by tunnelling through the barrier.
- Choosing a metal with work function close to that of semiconductor, so that there would be very small potential barrier height between metal and semiconductor
- Deposit a thin layer of narrow bandgap material between metal and semiconductor thus a layer of this material near its surface can promote ohmic behaviour.
- Post annealing, Typically, metal adhesion is poor for non-alloyed contacts and annealing is required. Since the level of doping of GaAs during epitaxy growth is limited, thermal processing of metallic layers, i.e., annealing, plays a crucial role in contact formation. However, it cannot be forgotten that deep diffusion of metal into epitaxial layers can also damage a device.

Generally, ohmic metal contacts for GaAs are deposited by sputtering or evaporation processes and are photolithography patterned, which are precise and common but expensive and non-manufacturable. In this study are investigated the alternatives that are less expensive and manufacturable such as inkjet and spin-coating.

2.3.6 Methods of Contact Formation (Studied in This Work)

In this work were carried out three investigation phases as below:

1- Printing copper nanoparticles ink by inkjet on glass substrates with different thickness and sintering by several laser parameters window to generate the conductive copper thin film and define the sheet resistance of that by four-point prob.

2- Printing copper nanoparticles ink by inkjet and spin-coating (as a alternative method) on GaAs substrates with different thickness then sintering (patterning) by several laser parameters. Afterward, rinsing the non-sintered copper with adequate solvent and subsequently measuring the I-V curves of structures to determine the contact resistance.

3- Depositing the pure copper and silver by e-beam PVD (physical vapour deposition) method to prove the ohmic contact and low contact resistance between thin films and two different type of GaAs.

The process flow is indicated in Fig.2.14.

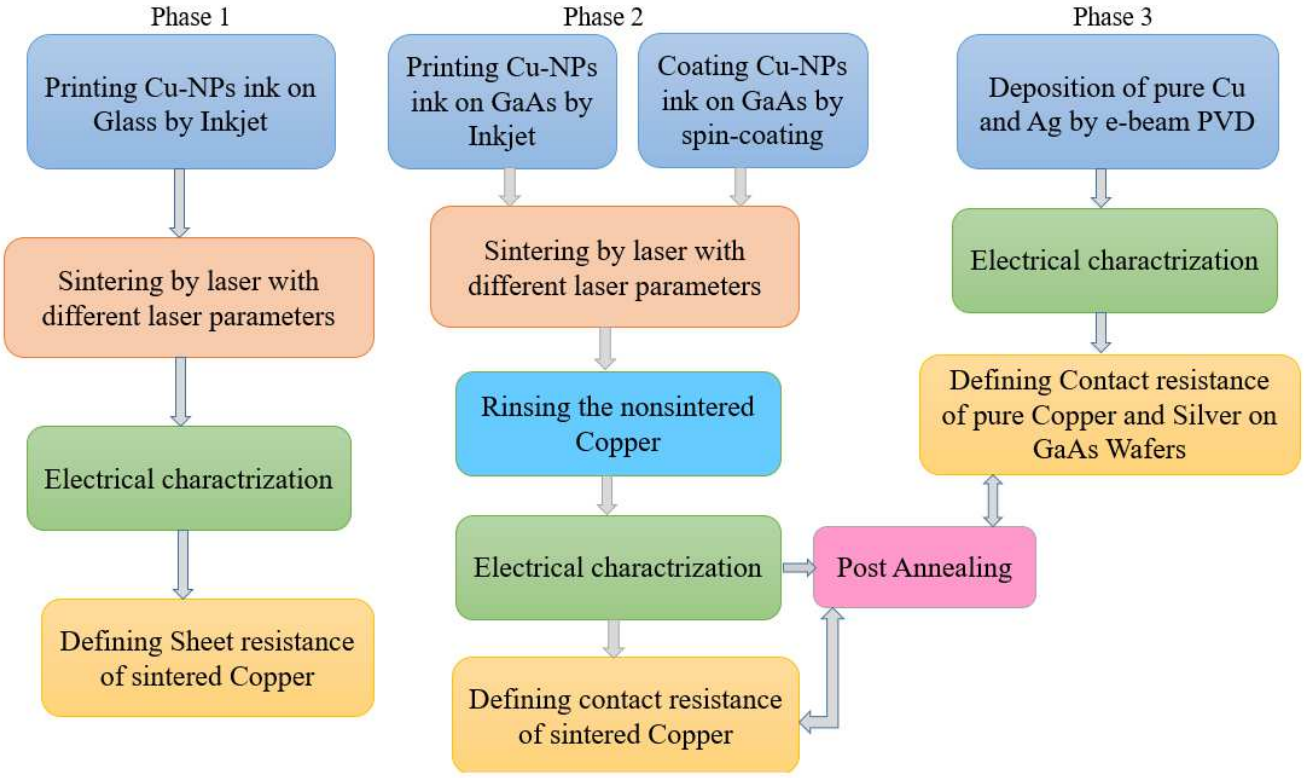

Fig.2.14. flow process of this study

In next section the techniques and materials of printing and laser sintering will be explained. Subsequently the characterization of the contacts is analysed and discussed.

Experimental

Developments for the front contact grid of the III-V/Si Tandem Solar cells in this study are processed with materials and techniques, which can provide low cost metal electrodes of high efficiency. This type of front contact grids was prepared with non-lithographic processes such as ink-jet, spin-coating methods and then sintering with laser.

The focus of this chapter is a description of the materials, methods and the setups used in carrying out the study. The three processes utilized for “contact electrodes preparation” are described in this section, starting with printing the copper nanoparticles on semiconductor, then sintering copper nanoparticles by laser and afterwards rinsing non-sintered copper and finally followed by investigating the characterization of the prepared samples.

3.1 Description of Material

In order to deposit the Metal electrodes on III-V semiconductor by ink-jet or spin-coating printing requires the Nanoparticle based Ink such as copper Nano-particle ink and appropriate III-V semiconductor such as GaAs wafer.

3.1.1 Copper Nanoparticles (Cu NP) Ink

Conductive inks based on metal NPs (metallic nanoinks), which are suitable for fabrication of 2D and 3D conductive structures. Main methods to produce metal NPs is wet chemical methods, which enable large-scale production of uniform metal NPs for conductive inks. Conductive inkjet ink is a multi-component system that contains a functional conducting material in a liquid vehicle (aqueous or organic) and various additives (such as rheology and surface tension modifiers, humectants, binders, and deformers), which enable optimal performance of the whole system, including the printing device and the substrate [22]. As a general rule, the size of the particles in inkjet ink formulation should be about 0.01 of the diameter of the print head’s orifice (typically 20-50 micrometres) to avoid its clogging and blockage [22]. These particles should be stable against aggregation and precipitation at high metal loading, typically 20–60 wt % in commercial inks. To ensure the stability of metal NPs, the ink formulation should contain a stabilizing agent, which is usually a polymeric material or a surfactant.

Currently, most conductive nanoinks are based on silver NPs. Silver is a noble metal, which is resistant to oxidation and possesses the highest electrical conductivity among metals. However, large-scale production of printed electronic devices requires low-cost nanoinks, in which silver as a conductive functional material should be replaced by lower cost metals of high electrical conductivity such as copper and aluminium, having conductivities of about 95 and 55% of that of silver [22]. The specific challenge while utilizing NPs of such metals is their oxidation at ambient conditions. For example, aluminium undergoes rapid (∼100 ps) oxidation in air with the formation of very dense nonconductive Al2O3 layer, with a thickness of 2–6 nm [22]. This obviously makes Al NPs inapplicable for the formulation of conductive nanoinks. Oxidation of Cu NPs is less rapid, compared to Al, especially in the presence of an excess of a reducing agent in the reaction mixture [23]. To overcome the oxidation problem, the synthesis of Cu NPs is usually performed in organic solvents such as polyols, toluene, heptanes, octyl ether, octylamine, and often under inert atmosphere (Ar, N2) [22]. Regardless of the method of synthesis, to minimize the exposure of Cu NPs to oxygen, they should be coated by a dense protective layer of a capping agent [22].

As was noted previous, inkjet ink for printed electronics contains a conductive nanomaterial, aqueous or organic liquid vehicle, and various additives that enable optimal printing performance and good quality of printed patterns [22]. Since metallic nanoinks should provide high electrical conductivity of the printed patterns, it is essential that the content of the metal NPs is high.

The higher the metal load in the ink, the higher the conductivity obtained from printing a given volume of droplets. Although the final conductivity of the printed patterns depends on several factors, including the number of printed layers and post printing process [22]. Usually the methods of formulating metallic nanoinks with high metal loading are based on a four-step procedure. The first step is the synthesis of metal NPs in the presence of stabilizing agent. Then, the synthesized NPs are separated by centrifugation or by precipitation with various organic solvents such as alcohols (methanol, ethanol, and isopropanol) or acetone. In the third step, the precipitated NPs are washed with a proper solvent to remove the excess of non-adsorbed materials such as dispersion stabilizers. The last stage is redispersing the obtained NPs in a proper liquid vehicle containing the required additives, usually by mechanical stirring, ultrasonication, and ball milling. Thus, the key for ink preparation is to satisfy both dispersion stability and electrical performance.

3.1.2 GaAs Wafer

During the last decade GaAs-based micro- and optoelectronics has developed to a global commercial player that does not replace but supplement silicon-based devices. This development has been due to some unique physical properties of compound semiconductors allowing for superior functionality of devices [24].

In contrast to silicon, GaAs and the other III-Vs, except for GaP, are direct semiconductors. The bandgap of GaAs is 1.424 eV at 300 K, which is significantly larger than that of silicon (EG = 1.12 eV at 300 K) and allows high-temperature and radiation-tolerant electronics, optical and mechanical sensors, and high-voltage rectifiers [24]. Due to a larger curvature at the minimum of the conduction band GaAs has a lower effective electron mass resulting in a higher electron mobility and drift velocity of carriers compared to silicon (see Fig.3.1). This allows devices working at higher frequencies [24].

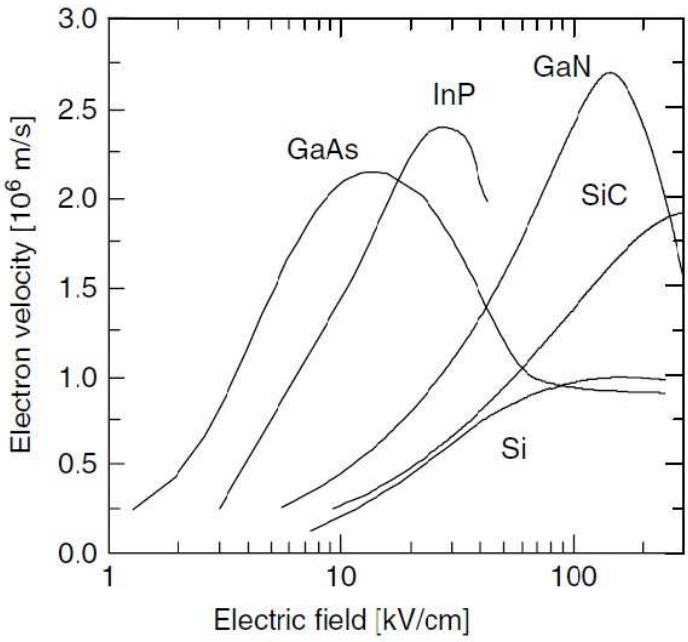

Fig. 3.1. Drift velocity of compound semiconductors verses silicon.

GaAs and other III-V compounds can rather easily be doped to get p- and n-type conductivity in the range of 10^{-3} to 10^{-1} Ωcm at room temperature, which is necessary for optoelectronic devices. Elements of the second group of the periodic table of elements act as acceptors (Zn, Cd(Codmium)), group VI elements (Te, S) as donors [23]. The thermal conductivity of GaAs (λGaAs = 0.46 W/cm K at 300 K) is lower than that of silicon (λSi = 1.41W/cm K at 300 K).

Therefore, heat dissipation and extraction from operating devices is less effective and limits the growth rate in crystal growth from the melt [23]. The critical shear stress of GaAs near the melting temperature is significantly lower than that of silicon, therefore thermoplastic relaxation of thermally induced stress by generation and multiplication of dislocations during crystal growth and subsequent thermal treatment is more important [23].

For the growth of GaAs single crystals from the melt two methods are of commercial interest, such as Liquid Encapsulated Czochralski (LEC) and Vertical Gradient Freeze (VGF) techniques:

1- Liquid Encapsulated Czochralski (LEC): By this technique, the material to be grown is first melted by induction or resistance heating under a controlled atmosphere in a non-reacting crucible, which is made from pyrolytic boron nitride (pBN) and contains the GaAs melt covered by liquid boron oxide encapsulates to avoid arsenic losses during melt growth [25].The melt is kept for a certain time at a temperature above the melting point and the temperature is then reduced to a value slightly above the freezing point. The freezing point is considered by cooling the melt until crystals start to appear on the surface. By pulling and rotating the seed simultaneously a crystallization center forms. The diameter of the pulled crystal is controlled by manipulating the temperature of the melt and the pulling rate. Suitable engineering of both axial and radial temperature gradients is needed to grow single crystals of desired dimensions reliably [26].

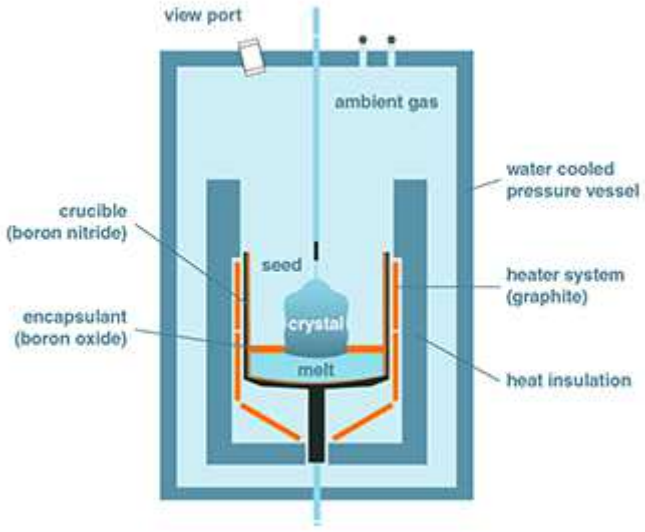

Fig.3.2.Schematic view of the LEC setup for growing GaAs crystals[25].

2- Vertical Gradient Freeze (VGF): it is a modification of the conventional Bridgman method. By this technique, a pyrolytic boron nitride (pBN) is used and charged with GaAs and boron oxide is placed in a furnace. The crystallization process is provided by a number of separately controlled zones which allow generating two nearly temperature-constant zones above and below the melting temperature and a controlled (small) temperature gradient in between [25]. Optimization of heat transfer in the furnace, and the melt and gas flows is the key point in growing quality crystals. Lower values of temperature gradients reduce dislocation density in the crystal and reduce probability of crystal cracking in the end of the process caused by residual stresses [27].

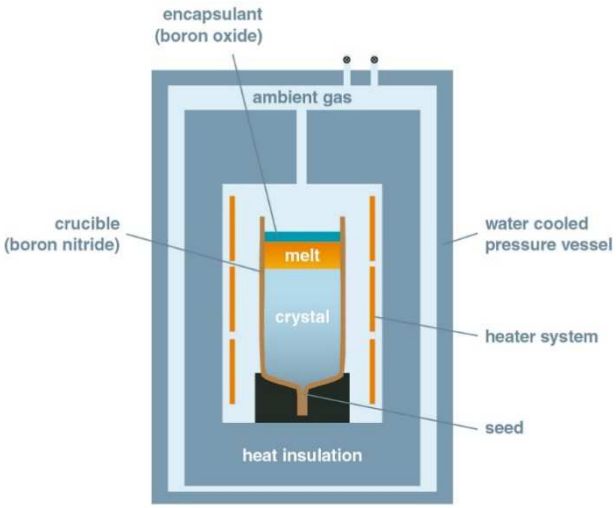

Fig.3.3.Schematic view of the VGF setup for growing GaAs crystals[25].

GaAs crystals are doped with different elements to achieve the required electric conductivity for semi-conducting or semi-insulating wafers. Control of segregation of doping materials is important to increase a high yield of GaAs wafers with electric conductivity values within the specification limits. Modelling of melt flow coupled with segregation helps to obtain distribution of dopant.

3.1.3 Si Wafer

The methods for making Si wafers is very similar to the preparation of GaAs wafers.

3.2 Description of Techniques

3.2.1 Printing Methods

During the last decade, the field of printed electronics to fabricate conductive electronic devices on solid and flexible substrates, received a great interest. Traditional methods of manufacturing electronic devices are photolithography, vacuum deposition, and electroless plating processes. These methods are multistage, require high-cost equipment, and usually the formation of large amounts of waste. A better alternative to these procedures are ink jet printing, screen printing and etc...

3.2.1.1 Ink jet

Ink-jet printing is a direct write, non-contact deposition technology with high line resolution. This technology has the advantage of a high material efficiency and a reduced process complexity. The main benefit compared to screen-printing is the higher line resolution (line width < 20 μm) of at least a factor of two compared to the minimum line width achievable with screen-printing technology [28].

IJP is characterized by the formation of droplets by a sudden pressure pulse in the nozzle chamber. In order to leave the nozzle in a reliable manner and to allow fast droplet generation (high printing frequencies), inkjet inks generally have low viscosities (in the order of 2−50mPa s) and rather low solid contents [29].

At least two types of IJP are distinguished, depending on the manner of droplet formation and ejection, which can be achieved either by a heat pulse, inducing solvent boiling and thus a pressure pulse (thermal IJP) (Fig. 3.4.a), or by the shape change of a piezo element integrated in the nozzle chamber walls (piezoelectric IJP) (Fig. 3.4.b). In both cases, the pressure pulse is eventually the result of an electric voltage pulse, which can be modulated in terms of intensity, time duration, and voltage ramp.

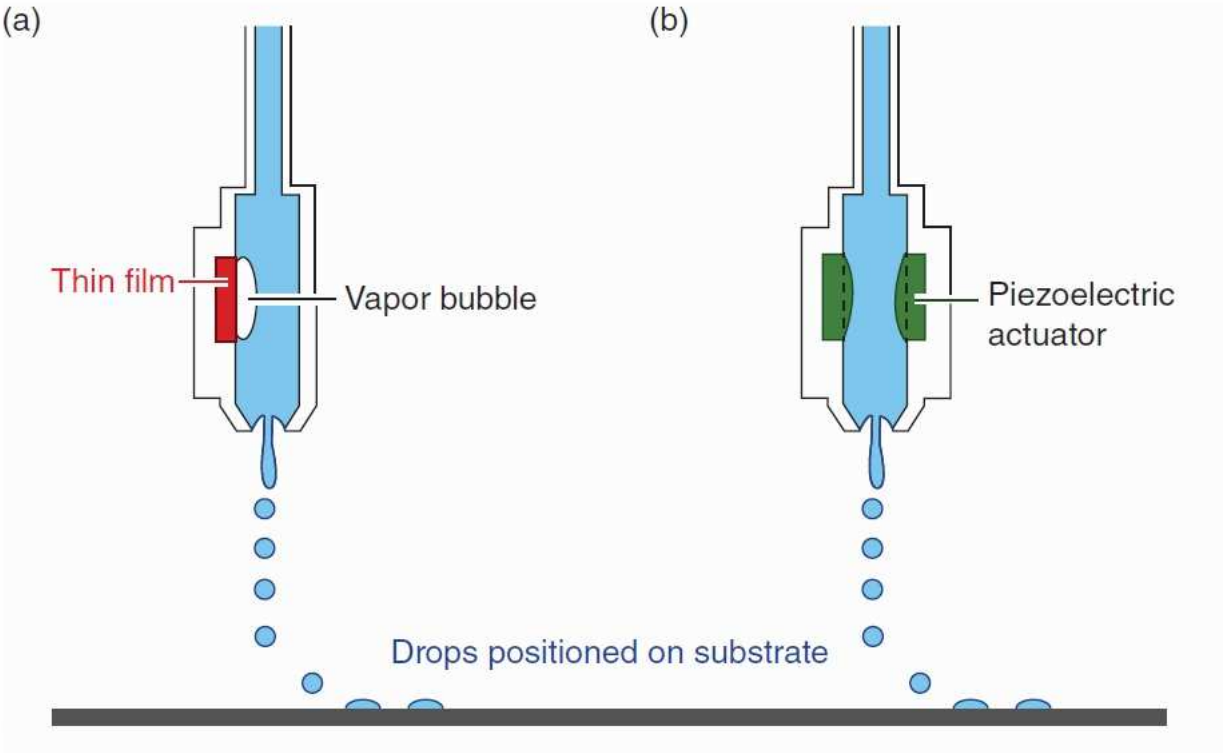

Fig.3.4. Operational principles of (a) thermal and (b) piezoelectric inkjet printing

A piezoelectric inkjet (PIJ) print head, as the name implies, uses a piezoelectric material to convert applied electrical energy into mechanical deformation of an ink chamber. The displacement of the chamber wall generates the pressure required for a drop to form and eject from the nozzle.

For a successful patterning, the ink formulation should be well designed not only for drop wettability and uniform deposition but also for electrical performance of the printed structure after drying. As for drop wettability, the dynamics of a colloidal suspension jet is known to be different from that of a Newtonian liquid in terms of no straight flying trajectories and non-axisymmetric ligaments [30]. The poor jetting behaviour brings out difficulties and irregularities in the printing process. In spreading and levelling, Marangoni flow, which is caused by concentration gradient and particle adsorption to the liquid-air interface, and non-Newtonian flow behaviour (e.g. differential evaporation rates) influence the levelling process and may sometimes cause the so-called coffee ring effect [30].

A. Printing Parameter

Many factors affect the performance of drop-on-demand inkjet printing. They include processing parameters[16–18] such as driving voltage (pulse height), dwell time (pulse width), and repetition rate, as well as fluid properties [30].

A.1. Length Scale of Printing Head

For Newtonian fluids, drop formation is determined by the dimensionless number and Z (length scale of the printing head) which is equal $(d\rho\sigma)^{1/2}/\eta$, where d is the nozzle diameter, σ surface tension, η viscosity and ρ density of ink. If Z is too low, no droplet can be formed, and if Z is too high, the formation of satellite droplets results in poor printing quality [30].

A.2. Driving Voltage

When a driving voltage is applied, the tube is radially polarised, and this causes a contraction of the transducer. The sudden displacement of the enclosed volume causes a drop of ink to be ejected from the nozzle. Some of the ink is moved backward in the tube, but this is not significant because of the high acoustic impedance of the long and narrow channel of the tube. When an electric voltage is applied to the piezoelectric material, it presses or expands the chamber which results in an ejection of a drop. The outer surface of the diaphragm is coated with a conducting material for electrical connection. Application of a driving voltage causes the diaphragm to bend, which results in creating a pressure inside the chamber, thereby bringing out an ink drop.

A.3. Firing Frequency

To improve the printing speed, there are three different approaches, including increasing the number of nozzles, and/or the droplet size, and/or the printing frequency (i.e., the number of droplets generated per nozzle per second [31]. In addition, increasing printing frequency can lead to significant improvement of printing speed. Both the speed and diameter of the ejected drop increased linearly with voltage if all other parameters such as fluid properties and temperature remained the same [32].

A.4. Waveform

An ink droplet hitting the surface at too high speed will splash and create a very ill-defined pattern because of residual oscillations. Waveform tuning can control impact velocity and avoid the occurrence of splashing, in other words the waveform is able to damp these residual oscillations. The parameters of waveform, that are optimized are the rise time, the dwell time, the fall time and the amplitude.

Both unipolar and bipolar waveforms, as shown in Fig.3.5., can be used as the triggering waveform for the inkjet printer.

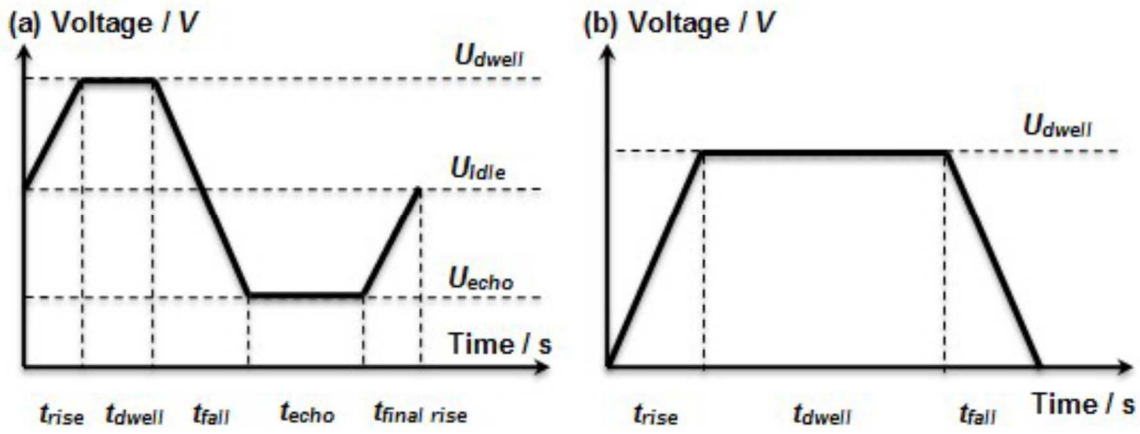

Fig.3.5. (a) Bipolar and (b) unipolar waveforms used for droplet generation in inkjet printer[35].

A.5. Stage Temperature

Temperature of the surfaces has a significant impact on the ink spreading. The higher temperature of substrate causes the fast evaporation process of the ink onto the substrates surface as well as causes the viscosity decreasing of the nano-ink. It is generally known, that the higher temperature causes the coffee ring effect creation, especially in the case of inkjet printing technology.

Furthermore, there is the main effect of the fast solvent evaporation on the drop's shape. This causes the increases of the dot's height and damages the dot's width which decreases.

With regard to different reports, it can be said that a substrate temperature higher than 60 °C causes fast evaporation of the solvents contained in the nano-inks in all cases of the investigated substrates.

3.2.1.2 Spin Coating

Spin coating is one of the most common techniques for applying thin films to substrates. It is used in a wide variety of industries and technology sectors. The advantage of spin coating is its ability to quickly and easily produce very uniform films, ranging from a few nanometres to a few microns in thickness [33].

Spin coating generally involves the application of a thin film evenly across the surface of a substrate by coating (casting) a solution of the desired material in a solvent (an "ink") while it is rotating. Spin coating is performed according to the following steps:

1- First the substrate is coated by the ink containing the molecules dissolved in a solvent.

2- Then the substrate is rotated at high speed and the majority of the ink is flung off the side.

3- by airflow during the rotating the solvent evaporates to leave the desired material on the substrate in an even covering.

The rotation of the substrate at high speed (usually >10 rotations per second = 600 rpm) means that the centripetal force combined with the surface tension of the solution pulls the liquid coating into an even covering.

A. Printing Parameter

A.1. Spin Speed

In particular, for industrial processes spin coating would generally only be recommended at speeds of >1000 rpm to ensure the best uniformity.

In general, the thickness of a spin coated film is proportional to the inverse of square root of the spin speed, as in the below equation where *t* is the thickness and *w* is the angular velocity [33]:

$$t \, \alpha \, \frac{1}{\sqrt{w}} \qquad (3\text{-}1)$$

The range of spin speeds available is important as it defines the range of thicknesses that can be achieved from a given solution.

The exact thickness of a film will depend upon the material concentration and solvent evaporation rate (which in turn depends upon the solvent viscosity, vapour pressure, temperature and local humidity) [33].

A.2. Distribute Type:

Probably the most important aspect to consider is the spin coating method used to distribute the solution - either a static distribute or a dynamic distribute.

In a static distribute the solution is placed upon the substrate while it is stationary and usually the entire substrate is covered in the solution before rotation begins. The spin coater is then started and brought up to required speed as fast as possible.

In a dynamic distribute the substrate is first started spinning and allowed to reach the desired spin speed before the solution is distributed into the centre of the substrate. The centrifugal force then rapidly pulls the solution from the middle of the substrate across the entire area before it dries.

The disadvantage of a dynamic distribute is that it becomes increasingly difficult to get complete substrate uniform coverage, when using either low spin speeds below 1000 rpm or very viscous solutions. This is because there is insufficient centrifugal force to pull the liquid across the surface, and the lower rotation speed also means that there is increased chance that the ink will be distributed before the substrate has completed a full rotation

A.3. Spin Duration

For most standard spin coating techniques, the objective is to keep the substrate spinning until the film is almost dry. As such the spin duration will mainly depend upon the boiling point, vapour pressure of the solvent that is used and also on the ambient conditions (temperature and humidity), which the spin coating is performed in. In general, higher spin speeds and longer spin times create thinner films.

A.4. Spin Steps

For high boiling point (and/or low vapour pressure) solvents, drying may take considerably long time (up to ten minutes in some cases) and therefore these solvents are most commonly used either as additives or with additional drying steps.

3.2.2 E-beam Physical Vapour Deposition

Electron Beam Evaporation is a powerful physical vapour deposition process that allows to evaporate materials, which have high melting point, so that are difficult or even impossible to deposit them by using standard resistance heating evaporation. During an e-beam evaporation process, current is first passed through a tungsten filament which leads to joule heating and electron emission, then high voltage is applied between the filament to accelerate these liberated electrons towards the crucible containing the material, which must be deposited. A strong magnetic field focuses the electrons into a unified beam, upon arrival, the energy of this beam of electrons is transferred to the deposition material, causing it to evaporate (or sublimate) and deposit onto the substrate.

In the Fig.3.6. illustrated a schematic of e-beam deposition. There are two types of substrate holder in this techniques, stationary and rotating. By rotating substrate holder rotates the substrate at particular speed so that, the thin film is uniformly deposited on the substrate.

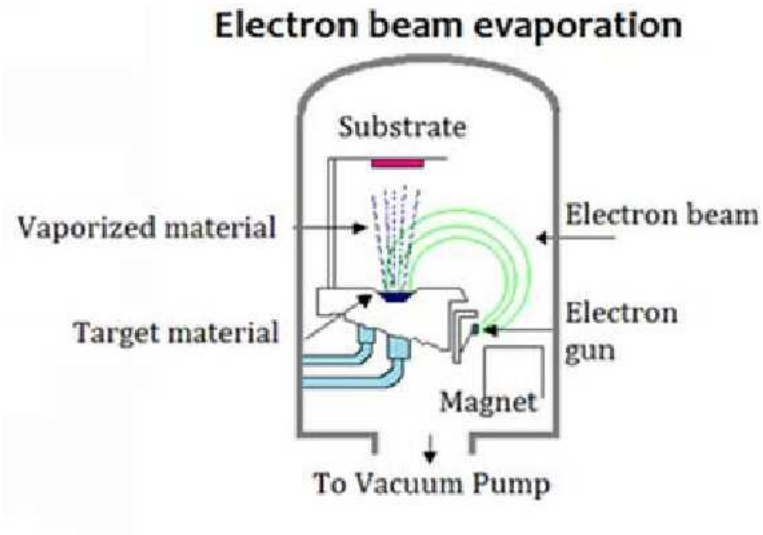

Fig.3.6. schematic of electron beams physical vapour deposition system [35].

The quality of deposition is due to several parameters such as, deposition rate (A/s), substrate holder (stationary or rotating), rotating speed, … etc.

3.2.3 Sintering Methods

After printing and drying ink, the presence of remaining insulating agents of ink prevents the formation of conductive structure, therefore post printing process, in which the insulating material are effectively removed is required. Such removal can be obtained by eventually sintering. There are different sintering methods, the most common sintering methods of metal nanoparticles (NPs) to avoid oxidation of metal are thermal sintering under reduced atmosphere and laser sintering.

3.2.3.1 Laser Sintering

In case of non-reactive metals such as Au and Ag, sintering is possible by simply heating up the printed ink in an oven. Copper, unlike silver, is oxidized rapidly at elevated temperatures; hence, conventional oven sintering cannot be used to render printed copper ink conductive. One solution to this is laser sintering [36], where the rapid temperature rise produced by the laser can sinter the copper before oxidation occurs.

A. Laser Sintering Parameter

Laser sintering of metal Nano inks can be performed by continuous or pulse wave. Laser sintering process can be characterized with different laser parameters.

A.1. Pulse Repetition Rate (PRR)

When the laser is running in pulsed mode the number of pulses per second or frequency of pulses is known as the **Pulse Repetition rate (PRR)**. The term **PRR** and pulse frequency are commonly used.

Sometimes the control system of the laser allows the emission of a single pulse, in other cases the emission is repeated over time, with a well-defined frequency. The pulse repetition rate ranges from 1kHz to 2MHz (FT, free trigger mode) and between 2MHz and 50MHz (SFD, seeder frequency divider mode) for the pico second-pulsed (pc-pulsed) laser.

A.2. Average Laser Power

Laser power is determined as power level that is brought by laser beam to the material (printed Cu NPs). This factor should be set to ensure that the particles will be heated close to melting temperature during scanning. Total laser energy brought by beam has important effect to sintering result. Overall energy, which is delivered to the particles, has an effect to laser power value used.

A.3. Pulse Energy

There is a linear dependency between the pulse frequency and the beam energy, which is proportional to the number of photons emitted by the laser cavity during the interval time. The following relations allow to compute the pulse energy, either knowing the peak power and the pulse duration or the average power and the pulse repetition rate.

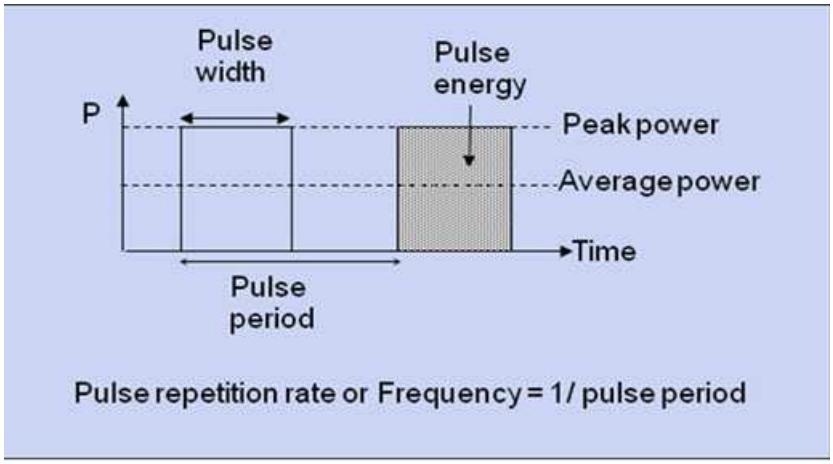

Fig.3.7. Piece-wise constant power waveform of the laser radiation. The grey area corresponds to the pulse energy. Both the peak and average power levels are shown [37].

Moreover, from the definition of average power following relation can be derived:

$$E_{PULSE} = \frac{P_{AVG}}{F_{REP}}$$

A.4. Lateral Distance:

Since the laser beam in the sintering process passes in parallel lines, the lateral distance is defined as the distance between two lines, normally in micro meter scale.

A.5. Focal Length

For most of the laser machining of materials, the beam emitted by the source passes through one or more lenses with the aim of focusing all the radiation in a small spot. The focal length of a lens is the distance after the lens where a collimated beam is focused, achieving the minimum beam diameter. Therefore, the focal length assumes positive values for a focusing lens and negative values for a defocusing one. The focal length is proportional to many parameters of the process:

- working distance between the lens and the sample to be irradiated with perfect spot.
- the minimum size of the spot achievable.
- the Rayleigh length, affecting the simplicity to optimally focus the beam on the sample.

In the case of ps-source, two different lenses were used: first set of experiments were carried out with 330mm focal length lens and the second set was carried out using a focusing lens with ℓ= 100mm. Before reaching the lens, the beam diameter was increased from 3mm (immediately after the source) to 12mm, by means of a beam expander.

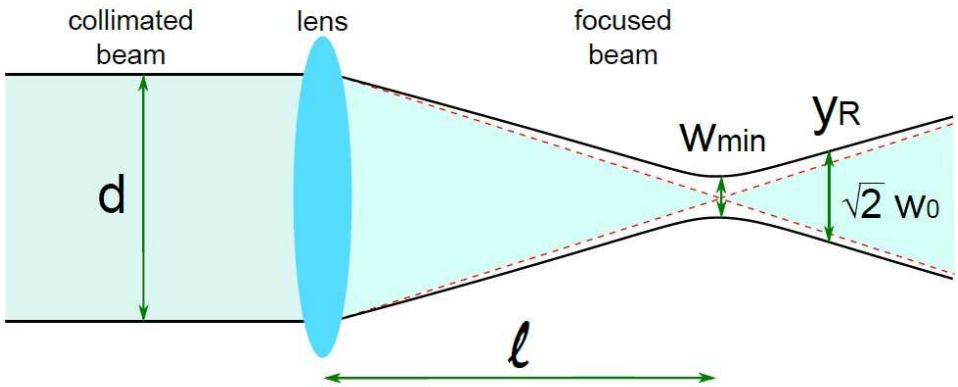

Fig.3.8. Lens focusing a collimated laser beam of diameter d.

Refer to Fig.3.8. The focal length is defined as ℓ.

A.6. Beam Diameter

With reference to Fig.3.8., the W_{min} or W_0 is defined as the position where the beam has the minimum diameter (beam waist radius). In case of Gaussian beam propagation, the beam radius increases moving far from the beam waist on the y direction. Rayleigh length y_R is defined as the distance from the beam waist where the radius is $\sqrt{2}$ times higher than the beam waist radius (W_0), the Rayleigh length is found for a Gaussian propagation.

A.7. Scan Velocity (Feed Rate)

Scanning speed means the speed of beam that is brought to material bed. The laser energy density is depending on scanning speed. By increasing the scanning speed, the laser energy density would be decreased if all other parameters such as laser power, PRR and etc., remained constant. To set the scanning speed generally is used a galvanometer scanner, which could be changed in a certain range from 1mm/s to 30m/s.

A.8. Pulse to Pulse Distance (PPD)

Given a certain pulse repetition rate F_{rep} with a certain scanning speed V, the distance between two subsequent spots can be defined as:

$$PPD = \frac{V}{F_{rep}} \qquad (3\text{-}2)$$

In this case, the pulse duration is assumed to be infinitesimal. If the PPD is higher than the spot size, then the spots are separated from each other, on the other hand, if it is lower than the spot size, the spots are overlapping, as shown in Fig.3.9.

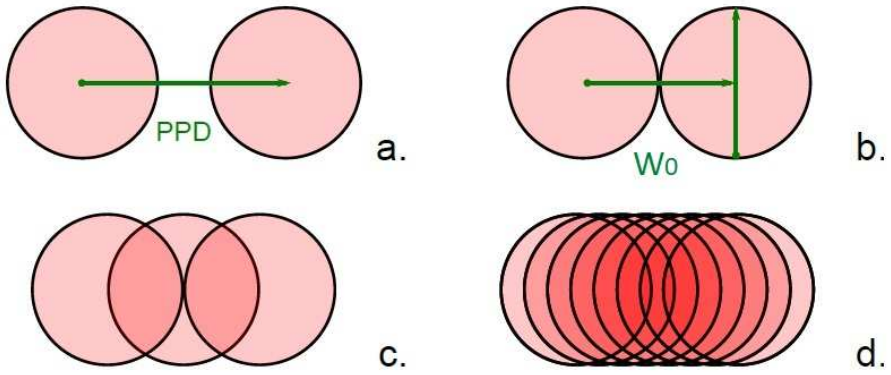

Fig.3.9. Laser spots with decreasing PPD. a) separated spots, b) spots next to each other with PPD = W0 , c) subsequent spots overlap, d) multi-spot overlap.

A.9.Jump Speed

The jump speed is described as the repositioning movement of the spot while no radiation is emitted by the source. A lower jump speed corresponds to a higher interval time between the irradiation of different parts of the pattern, allowing higher relaxation to the sample.

3.2.4 Characterization Methods

3.2.4.1 Optical Microscopy

Optical microscopy is a technique employed to closely view a sample through the magnification of a lens with visible light. An optical microscope uses one or a series of lenses to magnify images of small samples with visible light. The lenses are placed between the sample and the viewer's eye to magnify the image so that it can be examined in greater detail [38]. As a result, the image can be projected onto a computer screen in real time to examine a sample with these digital microscopes. The power of magnification of a compound optical microscope depends on the ocular, in our study we use the ocular lens, which has a final magnification from 5x, 10x, 20x, 50x to 100x.

3.2.4.2 Profilometer

Profilometry is a technique used to extract topographical data from a surface. The purpose of profilometry is to get surface morphology, such as step heights and surface roughness. This can be done using a physical probe or by using light. All profilometers include at least two parts, a detector and a sample stage. The detector is what determines where the points on the sample are and the sample stage is what holds the sample. In some systems, the sample stage moves to allow for measurement, in others the detector moves and in some both move.

There are two types of profilometers: stylus and optical. Stylus profilometers use a probe to detect the surface, physically moving a probe along the surface in order to acquire the surface height. This is done mechanically with a feedback loop that monitors the force from the sample pushing up against the probe as it scans along the surface. A feedback system is used to keep the arm with a specific amount of torque on it, known as the 'setpoint', the changes in the Z position of the arm holder can then be used to reconstruct the surface [39]. A Schematic of a stylus profilometer is shown in Fig.3.10.

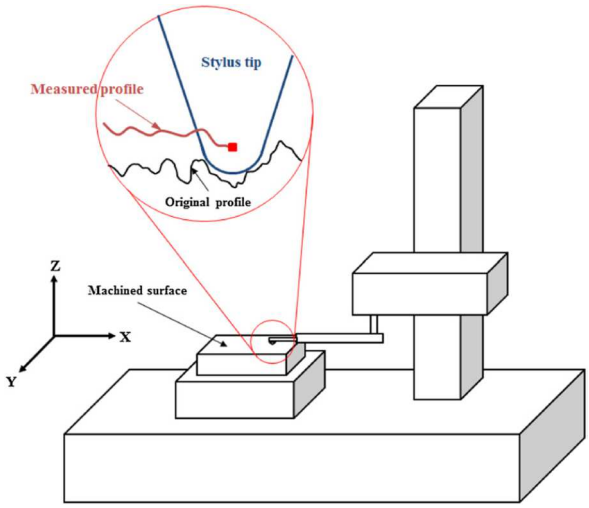

Fig.3.10. Schematic of a stylus profilometer [39].

Stylus profilometry requires force feedback and physically touching the surface, so while it is extremely sensitive and provides high Z resolution, it is sensitive to soft surfaces and the probe can become contaminated by the surface [39]. This technique can also be destructive to some surfaces. Because a stylus profilometer involves physical movements in X, Y and Z while maintaining contact with the surface, it is slower than non-contact techniques, the stylus tip size and shape can influence the measurements and limit the lateral resolution [39].

3.2.4.3 AFM (Atomic Force Microscopy)

Atomic force microscopy (AFM) is an advanced technique of studying properties of materials at an atomic scale. AFM provides a 3D profile (image) of the surface to prepare quantitative data on a variety of surfaces. Now, many material properties can be determined with AFM techniques, including friction, electrical forces, capacitance, magnetic forces, conductivity, viscoelasticity, surface potential, and resistance [40].

A typical AFM setup consists of a probe in the shape of a cantilever with a small tip at its free end, a laser, a four-quadrant photodiode, and a scanner unit. The laser beam is focused onto the back of the free end of the cantilever and from there reflected to the four-quadrant photodiode; this allows detecting the bending of the cantilever with high precision.

The interaction between the sample and the tip gives rise to either attractive or repulsive forces. These forces give information about the topography of the sample.

While scanning the tip across a sample surface, the force between tip and sample leads to changes either in the static bending of the cantilever (when the tip is in contact) or in the resonance frequency of the cantilever oscillation (when it is vibrated and the tip is at a small distance from the surface) [41]. Fig.3.11. schematically shows this basic AFM experimental setup.

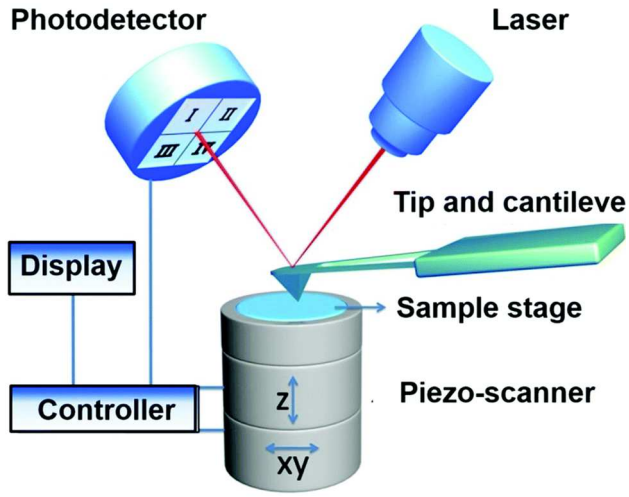

Fig.3.11. Working principle of an AFM consisting of a laser, a position-sensitive photodiode and the sample on a scanning xyz-stage [42].

There are 3 primary imaging modes in AFM:

1) Contact AFM (Static Mode):

In the contact mode, the AFM is at its simplest working mode. Here the cantilever is adjusted until the sample and the probing tip are in contact.

The tip-sample interacting forces are in the repulsive regime (repulsive van der waals). The amount of force between the probe and sample dependant on the spring constant of the cantilever and the distance between the probe and the sample surface. This force can be described by using Hooke's Law:

$$F = -k \cdot x \qquad (3\text{-}3)$$

Where, F = Force, k = spring constant and x = cantilever deflection

In this mode the feedback loop keeps the deflection of the cantilever constantly at the set-point (The set-point is a value set by the operator of the microscope) in the other words, the force between the probe and the sample remains constant and an image of the surface is obtained. (To keep this force constant, the cantilever holding the crystal would move up and down in the Z-axis. thus, when there is an elevation or depression in the surface, the cantilever would automatically move up or down.)

2) Intermittent Contact (Tapping) (Dynamic Mode)

The imaging is similar to contact. However, in this mode the cantilever is oscillated at its resonant frequency and the vibration amplitude of the cantilever is measured to estimate the deflection of the cantilever. The probe lightly "taps" on the sample surface during scanning, contacting the surface at the bottom of its swing. The vibration amplitude of the cantilever is measured to estimate the deflection of the cantilever.

By maintaining a constant oscillation amplitude, a constant tip-sample interaction is maintained and an image of the surface is obtained.

3) Non-Contact AFM (Dynamic Mode)

In this mode the tip is brought close to the sample in a constant distance but not in contact. The tip is oscillated at or near its resonance frequency, according to the following equation:

$$W=\sqrt{\frac{k}{m}} \qquad (3\text{-}4)$$

where k is the spring constants of the cantilever, m is the mass of the spring-like cantilever.

These oscillations are mechanically excited by the system on which the cantilever is mounted. The cantilever must be stiffer than in the contact mode, this allows the cantilever to have a small bending and a high force sensitivity. The interacting forces are in the attractive regime (attractive van der waals).

The curve of the force versus distance of any kind of three imaging modes is indicated in Fig.3.12.

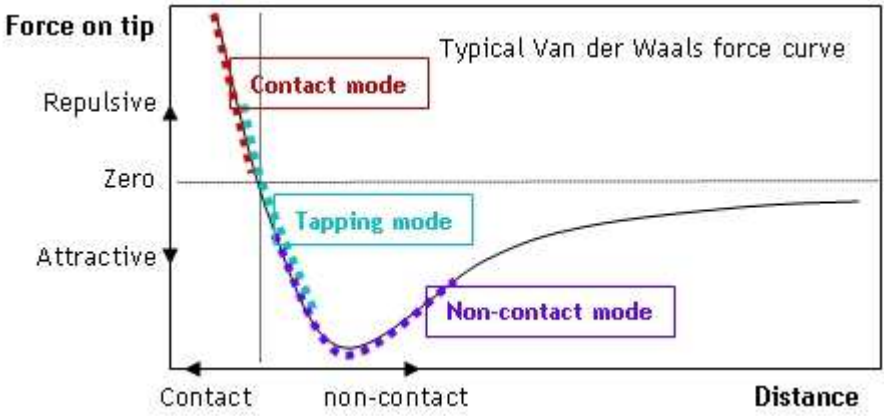

Fig.3.12. Force-distance curve for atomic Force Microscopes [43].

3.2.4.4 SEM (Scanning Electron Microscopy)

Fundamental Principles of SEM (Sample-Electron Interaction)

SEM, which is a type of electron microscope, uses electrons for imaging, in a similar way that light microscopes use visible light. SEM utilize a focused beam of high-energy electrons to generate a variety of signals at the surface of sample. Generally the electron beam is scanned in a raster scan pattern, the signals that derive from electron-sample interactions define information about the sample including external morphology and composition.

There are two types of electron-sample interaction: Elastic electron scattering, where incident electrons transfer no energy to the sample and inelastic electron scattering, where electrons do

transfer energy to the sample. The incident electrons are decelerated in the solid sample, and a variety of signals are produced. These signals include secondary electrons (that produce SEM images), backscattered electrons (BSE occur by heavy elements thus backscatter electrons are more strongly and appear brighter image, that are used to detect contrast between areas with different chemical compositions), electron backscatter diffraction (EBSD that are used to determine crystal structures and orientations of minerals), photons (characteristic X-rays that are used for elemental analysis and continuum X-rays), visible light (cathode-luminescence(CL) and heat .

In Fig.3.13. illustrates the different signals by electron sample interaction.

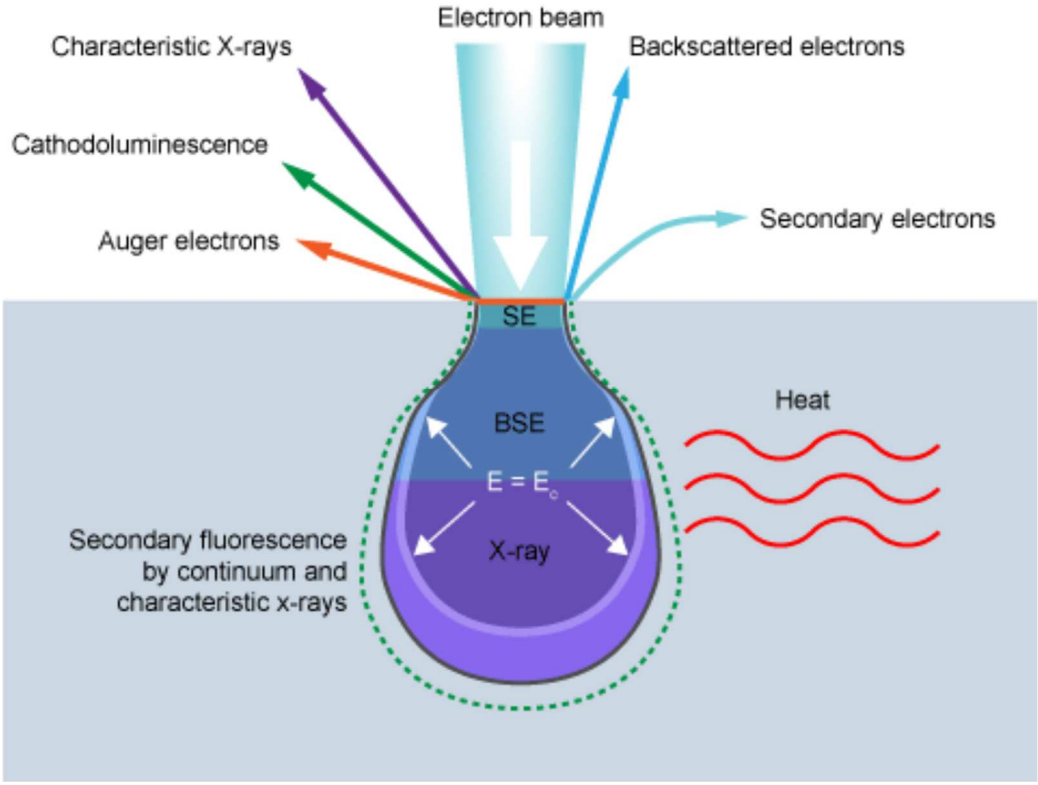

Fig.3.13. Schematic of electron beam interaction [44]

These signals are collected by one or more detectors to form images which are then displayed on the computer screen. When the electron beam hits the surface of the sample, it penetrates the sample to a depth of a few microns, depending on the accelerating voltage and the density of the sample.

Secondary electrons and backscattered electrons are commonly used for imaging samples: Secondary electrons are most valuable for showing morphology and topography on samples. Fig.3.14. represents a schematic of SEM technology:

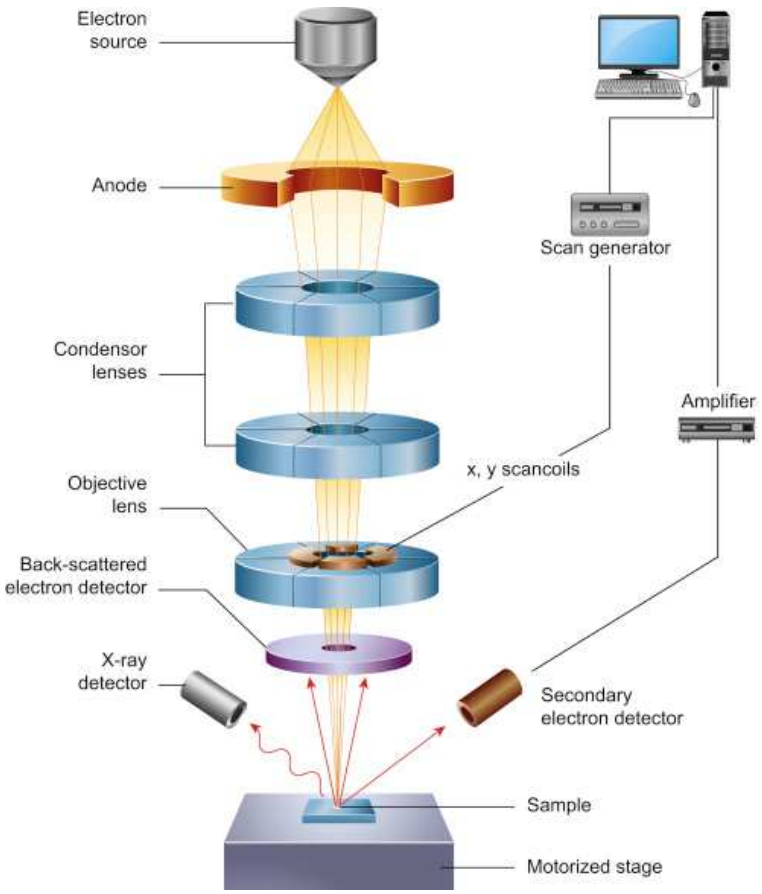

Fig.3.14. Schematic of a Scanning Electron Microscope [45]

The main components of SEM include:

- Source of electrons
- Column down which electrons travel with electromagnetic lenses (condenser and objective)
- Electron detector (due to microscope type BSE and X-ray detector can be applied)
- Sample chamber
- Computer and display to view the images

Electrons are generated at the top of the column, accelerated down and passed through a combination of lenses and apertures to produce a focused beam of electrons which hits the surface of the sample. The sample is mounted on a stage in the chamber area, both the column and the

chamber are evacuated by a combination of pumps. The level of the vacuum will depend on the design of the microscope.

The position of the electron beam on the sample is controlled by scan coils situated above the objective lens [46]. These coils allow the beam to be scanned and rastered over the surface of the sample, furthermore, enable information about a defined area on the sample to be collected. Afterwards the signals as a result of the electron-sample interaction are detected by appropriate detectors.

The maximum resolution obtained in an SEM depends on multiple factors, like the electron spot size and interaction volume of the electron beam with the sample [46]. While it cannot provide atomic resolution, some SEMs can achieve resolution below 1 nm. Typically, modern full-sized SEMs provide resolution between 1-20 nm whereas desktop systems can provide a resolution of 20 nm or more [46].

3.2.4.5. Electrical Measurement

The metal-semiconductor (MS) contact is the most useful device in the study of semiconductor surfaces and essential component in semiconductor device. To evaluate, how the electrical devices operate usually are used the I-V curves, which are measured by a four-point probe**.**

a. Four-Point Probe

The most common technique used for measuring sheet resistance is the four-probe method. This technique involves using four equally-spaced, co-linear probes (known as a four-point probe) to make electrical contact with the material. Most four-point probes available commercially use sharp needles as probes. The four-probe method works by contacting four equally-spaced, co-linear probes to the material. This is known as a four-point probe, and a schematic is shown in Fig.3.15.

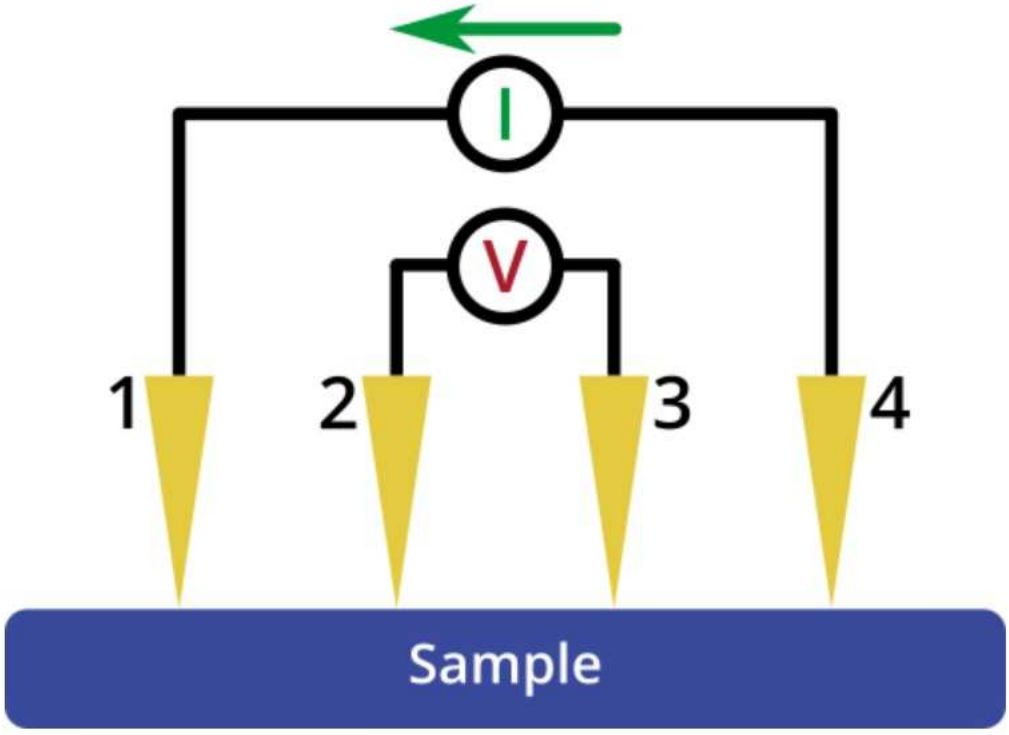

Fig.3.15 .Schematic diagram of a four-point probe circuit [47].

A DC current is applied between the outer two probes (1 and 4) and a voltage drop is measured between the inner two probes (2 and 3). The sheet resistance can then be derived by following equation:

$$R_s = \frac{\pi}{ln2}\frac{\Delta V}{I} = 4.53236\,\frac{\Delta V}{I} \qquad (3\text{-}5)$$

where, R_s is the sheet resistance, ΔV is the change in voltage, which is measured between the inner probes, and I is the current applied between the outer probes. The sheet resistance is expressed with the units Ω/□, or "ohms per square".

In addition to the factor of π/ln2, a geometric correction factor is often required. The correction factor is based upon the size and shape of the sample, as well as the positioning of the probes, and accounts for the limitation of current pathways through it [47]. However, it should be noted that the most accurate measurements are taken from the centre of the sample. If the thickness of the measured material is known, then the sheet resistance can be used to calculate its resistivity:

$$\rho = R_s.t \tag{3-6}$$

where, ρ is the resistivity, and t is the thickness of the material.

b. I-V Curves

I-V curves (or current-voltage curves) are a common method of characterising electrical devices. They reveal the relationship between the voltage applied across a device and the current flowing through it. I-V curves for the metal-semiconductor structures mainly depend on the barrier heights of the contacts and the carrier concentration. Whenever the barrier height is low the relationship between voltage and current is linear (ohmic behaviour) but a nonlinear relationship (schottky behaviour) portend to a high barrier height.

To calculate the contact resistance between metal and semiconductor requires some pads (like lines or squares) or an interdigitated pattern. The pads must be the same size, and the distances between the pads must be different. (see the Fig.3.16.)

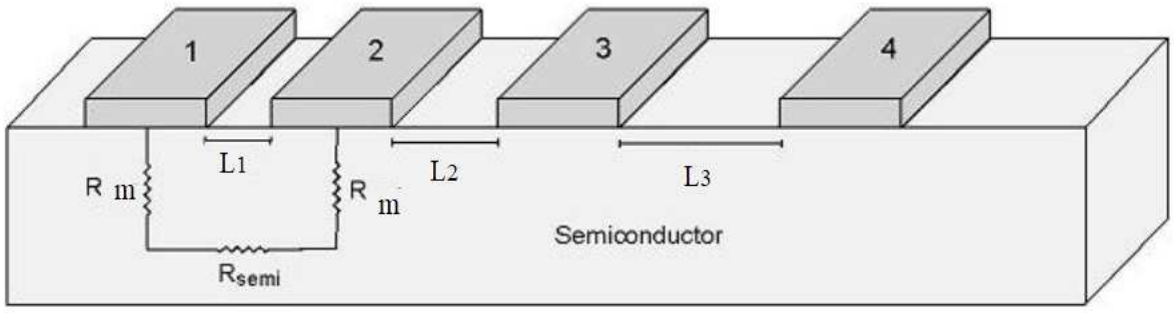

Fig.3.16. Schematic of the metal pattern includes some pads with various distances.

But in this study are used six interdigitated patterns. Each pattern has the same fingers, but the distance between fingers for pattern 1 to pattern 6 is varied from L_1 to L_6. Effective length is defined by W. Fig.3.17. represents the interdigitated pattern with smallest distance between fingers (L_1)

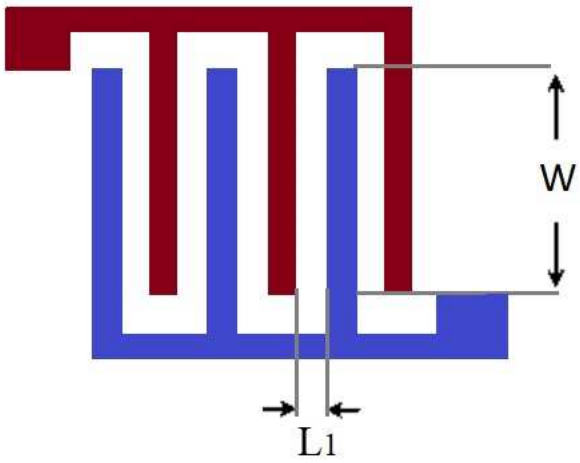

Fig.3.17. schematic of interdigitated pattern

The measurements require simple IV curves, these are most easily done at a probe station, which apply a voltage between several pairs of adjacent pads, and measure the current flow. From this, the resistance between those two pads ($R=\frac{V}{I}$) is calculated.

c. Calculate the Contact Resistance

As illustrated in the picture above (Fig.3.15), the total resistance between any fingers is displayed as the series combination of resistors: two times the metal resistance, two times the contact resistance and the semiconductor resistance between.

$$R_T = 2R_m + 2R_C + R_{semi} \quad (3\text{-}7)$$

Where R_m is the metal resistance, R_C is contact resistance, which is associated with the metal/semiconductor interface, and R_{semi} is the usual semiconductor resistance.

The resistivity of the metal in the contact is so low that $R_C >> R_m$, and so R_m can be ignored.

The semiconductor resistance is:

$$R_{sem} = R_s \frac{L}{W} \quad (3\text{-}8)$$

$$R_T = \frac{Rs}{W} L + 2R_c \quad (3\text{-}9)$$

Where R_s also includes the number of fingers, but R_s will never be needed explicitly.

These results suggest a method for measuring the contact resistance. If resistors of several different finger distances are constructed, keeping all other details the same, the total resistance of each can measured and plotted [48].

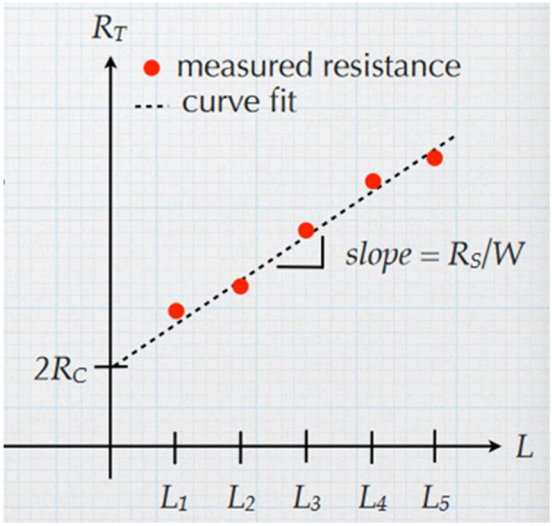

Fig.3.18. The relationship between measured resistance versus various finger distances[48].

In the limit of a resistor with zero finger distance, the residual resistance would be just twice the contact resistance. It can be found from the graph by extrapolating back to L= 0 [48].

As a secondary benefit, the sheet resistance of the semiconductor can be found from the slope of the line.

3.2.5. Adhesion Tests

Adhesion of printed layers is one of the preconditions for mechanical performance and reliability of flexible printed electronics. For adhesion testing the most common methods are pull-off test and cross cut tape test. They are used both in industrial as well as scientific practice.

The pull-off test is a practical method to see the overall adhesion of the deposited layer on the used substrate and to get quantitative information about the adhesion. In pull-off test a tape is applied onto the dried ink and then pulled off. The tester measured the force needed to detach the deposited layer from the sample. In this work, three to four parallel measurements were done and the average result was considered.

3.3 Applied Material

3.3.1. Cu-NP Ink Specification

A commercial nano-copper ink, CI-005 (Intrinsiq Materials,UK),with an average particle size smaller than 100 nm, solid content 26%(Weight %), viscosity 13 cP (at 20°C) and density of 1.27g/ml was used for this study. This copper nanoparticle based ink consists of coated pure copper nanoparticles dispersed in solvent. The specialized coating stabilizes the copper and prevents the ink from agglomerating, ensuring a long shelf life.

3.3.2. GaAs Wafer

In this study two types of GaAs wafer were utilized, which were fabricated in two different companies. These are called “Azur” and “Freiberger”, The technical specifications of wafers are listed in the table below:

Wafer / Parameter	Azur	Freiberger
The crystal growth method	LEC	LEC
Conduction type	N-Type	N-Type
Dopant	Te	Te
Carrier concentration	1.0E19	4.0E16 - 4.0E18
Thickness	450 µm	571± 20 µm

Fig.3.19. shows the morphological image of the two types of GaAs wafers before copper deposition. It is visible that, on the high doped GaAs wafer (Azur) there is some repetitive pattern however, the low doped GaAs wafer (Freiberger) has a smoother surface.

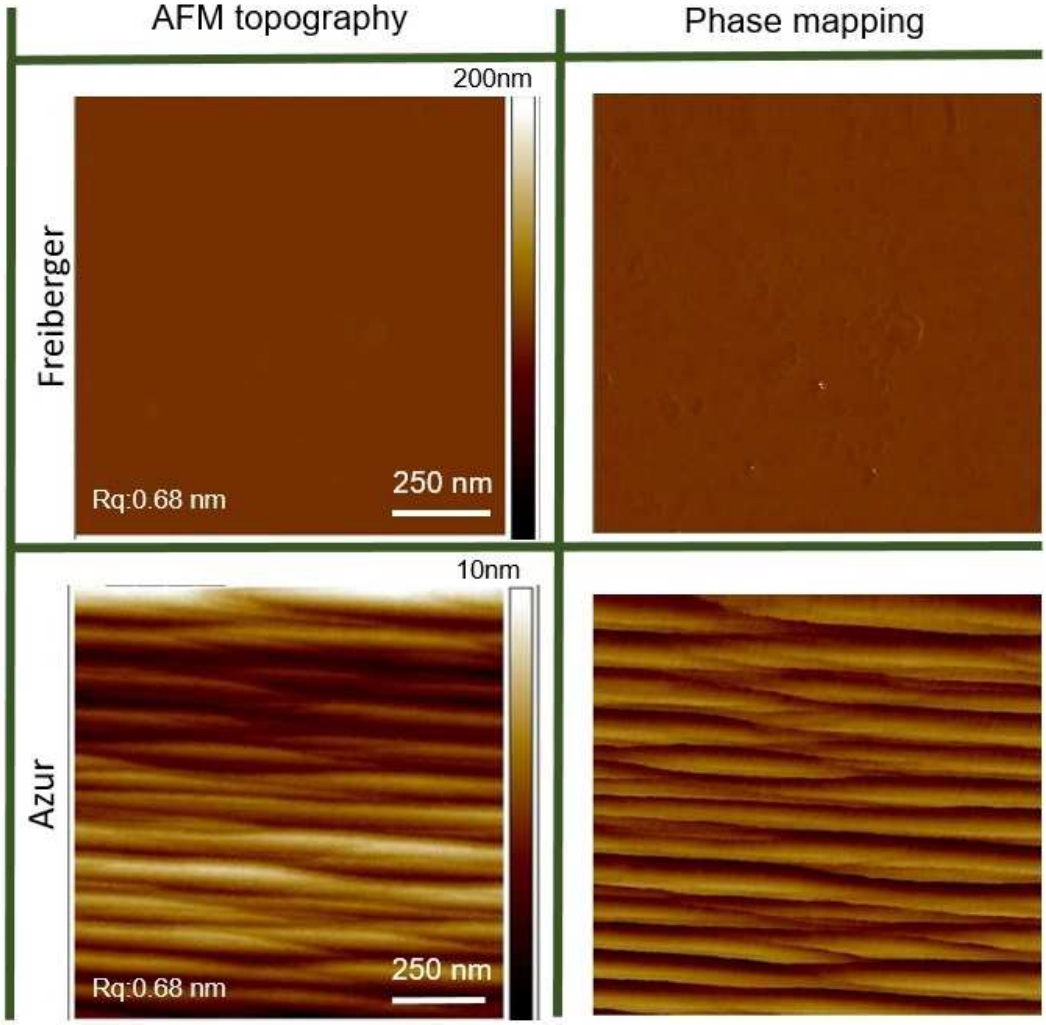

Fig.3.19. Morphological images of high doped (Azur) and low doped (Freiberger) GaAs

3.4 Applied Techniques

3.4.1 Ink Jet Printing

The printing setup was an inkjet printer, PixDro-LP50 with a drop on demand print head; Dimatix Spectra SE-128 comprised of 100 nozzles (see Fig.3.20). With proper parameter settings (driving voltage and waveform, jetting temperature, firing frequency, etc.), excellent jetting performance for our copper inks could be demonstrated. The ink droplets are well directed and constantly jetted out, which results in approx. 30 picoliter droplets.

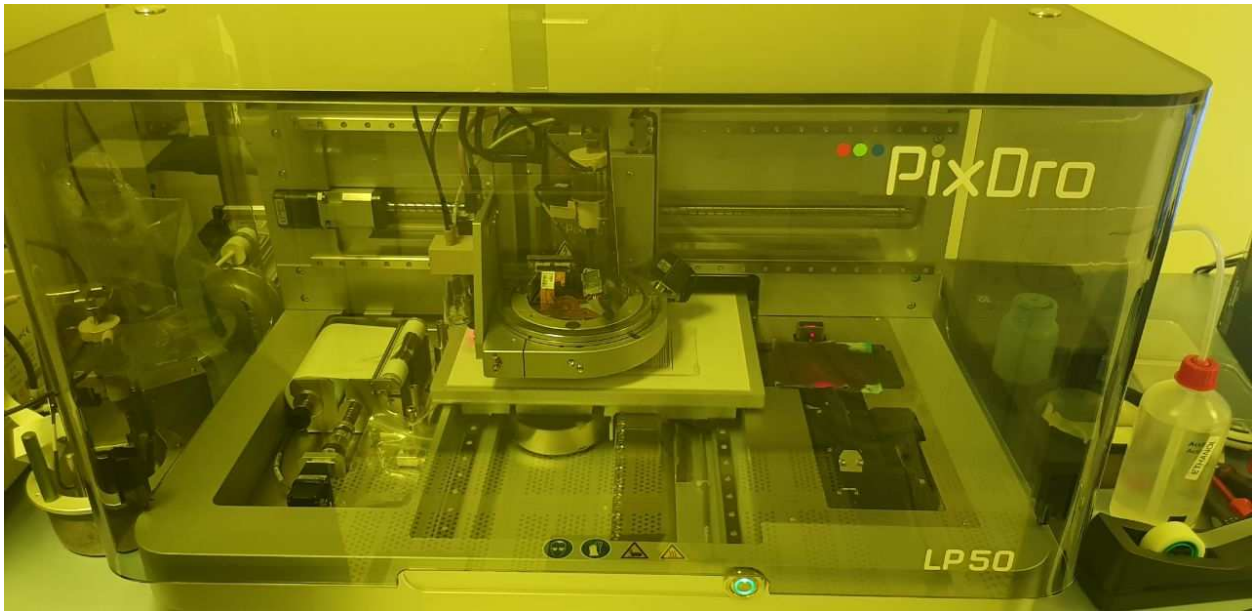

Fig.3.20. Inkjet printer, PixDro-LP50 with a print head; Dimatix Spectra

Experimental parameter:

The printing parameters on glass and GaAs substrate are listed on Table 1.

substrate	parameters	values
Glass	substrate height(Z)	1mm
GaAs		0.7 mm
Glass and GaAs	Head voltage	85 V
	Firing Frequency	200 Hz
	Resolution	800dpi
Glass	Wave(T_{rise} , T_{dwell} , T_{fall})	4, 6.6, 4 µs
GaAs		3, 6, 3 µs
Glass	Stage temperature	30°C or 60°C
GaAs		30°C

3.4.2 Spin Coating

Spin coating SPIN150i was used to produce thin film copper nanoparticles on different types of GaAs and Si wafers (see Fig.3.21.). As was discussed in last section about the different parameters in spin- coating, the parameters for GaAs and Silicon substrate are listed in the table below.

Fig.3.21. Spin- coating printer SPIN150i

Experimental parameter:

substrate	step1			step2		
Si	spin speed	ramp time	duration time	spin speed	ramp time	duration time
	500 rpm	7s	5s	2000 rpm	7s	30s
Si and GaAs	step1					
	spin speed	ramp time	duration time			
	3000 rpm	7s	30s			

3.4.3 Drying Printed Ink

The printed nanoparticles ink on all substrates were dried in oven at 50°C for 2h30 min under vacuum.

3.4.4 Laser Sintering

Experimental Setup:

For the study of the laser sintering process, a 1064*nm* pulsed-laser source has been used, with ultrashort-pulse regime (10*ps*).

The laser source is a diode pumped infrared (λ= 1064nm) picosecond-pulsed laser, based on Nd:YVO4 crystal, with high pulse repetition frequency up to 50MHz and maximum average power of 100W. The diagram in Fig.3.22. shows the composition of the ps-laser setup and the interaction between its components.

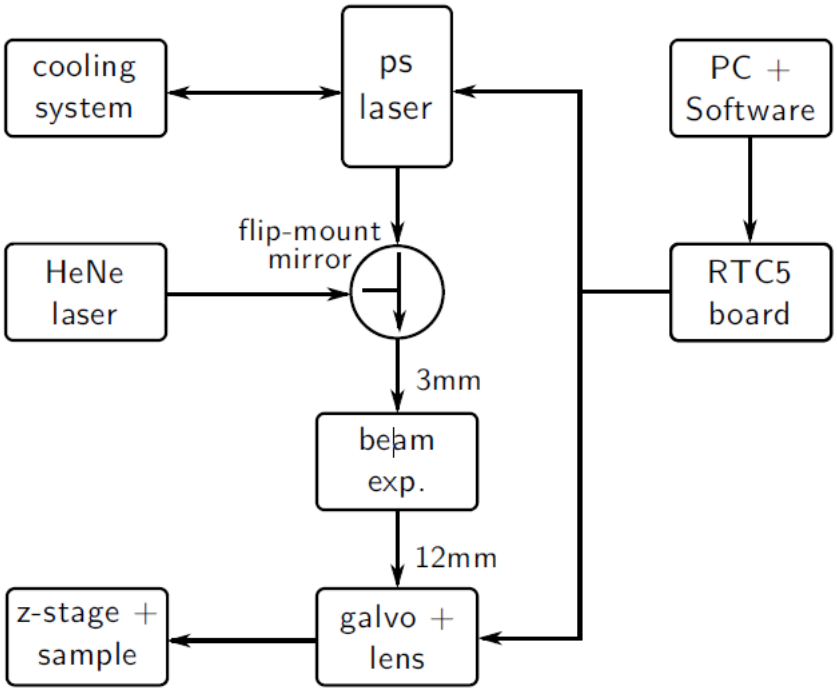

Fig.3.22. Schematic diagram of the ps-pulsed laser setup.

The beam produced by the source with an initial diameter of 3mm is directed through a beam expander, increasing the size to 12mm. The beam is then reflected by means of some mirrors towards the aperture of the galvo head. A high-speed galvanometer scanner (maximum speed of 30m/s) can deflect the beam, which is then focused through a lens and reaches the sample. The combination of a manually adjustable stage and of a micro screw stage allows to move the sample closer to the lens, away from the optimal focal plane of the beam and to achieve bigger off-focused spots. Two f-theta lenses with different focal lengths are used (330mm and 100mm focal length). F-theta lenses exploit a system of properly designed refractive coatings to provide always the same spot size on a flat sample. Both the galvanometer scanner and the laser source are synchronized

by the RTC5 (“ScanLab Real-Time Control 5”) board, controlled by “ScanLab LaserDesk” software running on PC. The pattern to irradiate is designed in this software where the value of all the parameters of the process can be adjusted.

A red HeNe low power continuous-wave laser is integrated into the beam path by means of a mirror on flipping-mount and used as a pointing system for the alignment of the samples on the stage, before their irradiation with the infrared laser.

Considered the high power supplying the laser, a water-liquid cooling system is used to stabilize the temperature of the source to 26°C. Moreover, the ambient temperature is kept to 23°C, to limit the temperature drift of mirrors properties, which could cause misalignment in the beam path and consequently a reduction in power and global accuracy of the process.

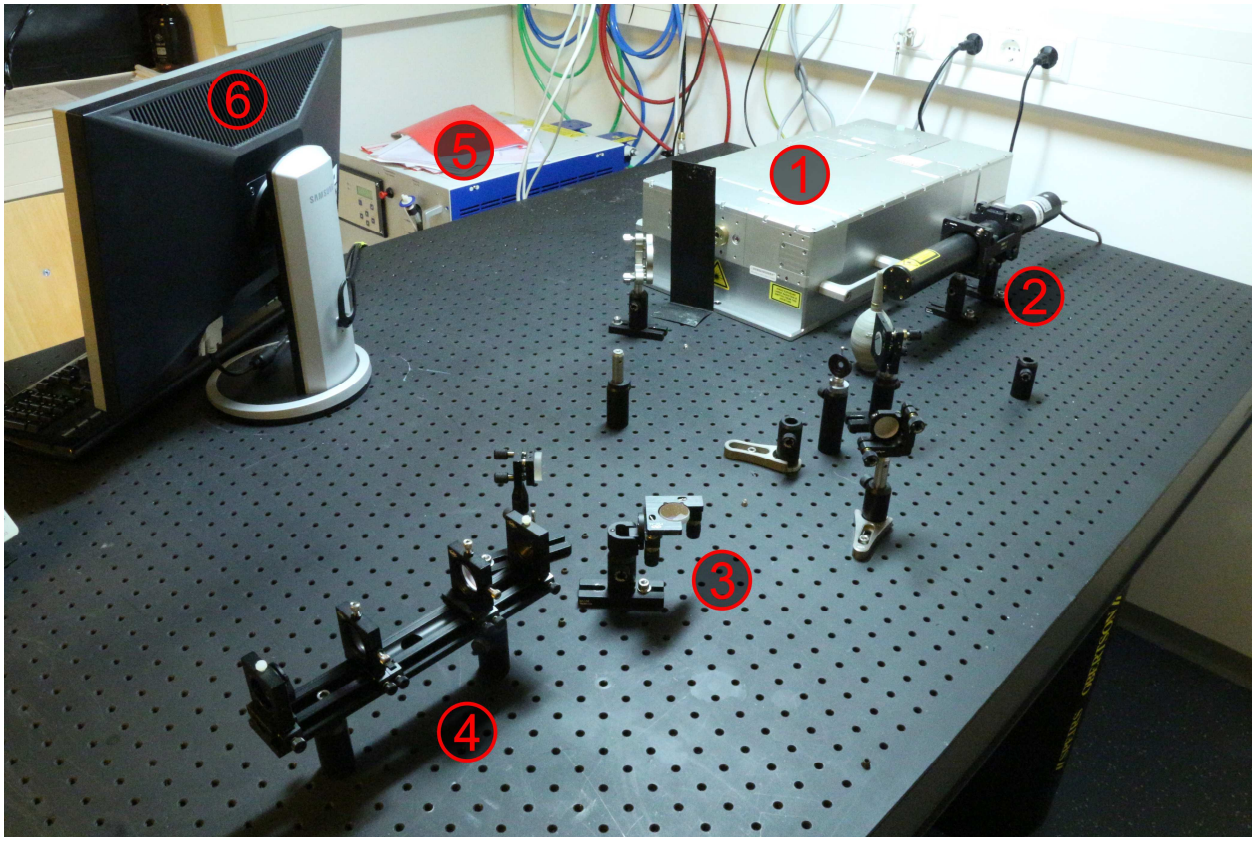

Fif.3.23. Ps-pulsed setup showing laser sources and beam path. ① IR ps-pulsed source; ② CW HeNe alignment laser; ③Flip-mount mirror; ④ Beam expander; ⑤Water-liquid cooler; ⑥ PC running control software and RTC5 board.

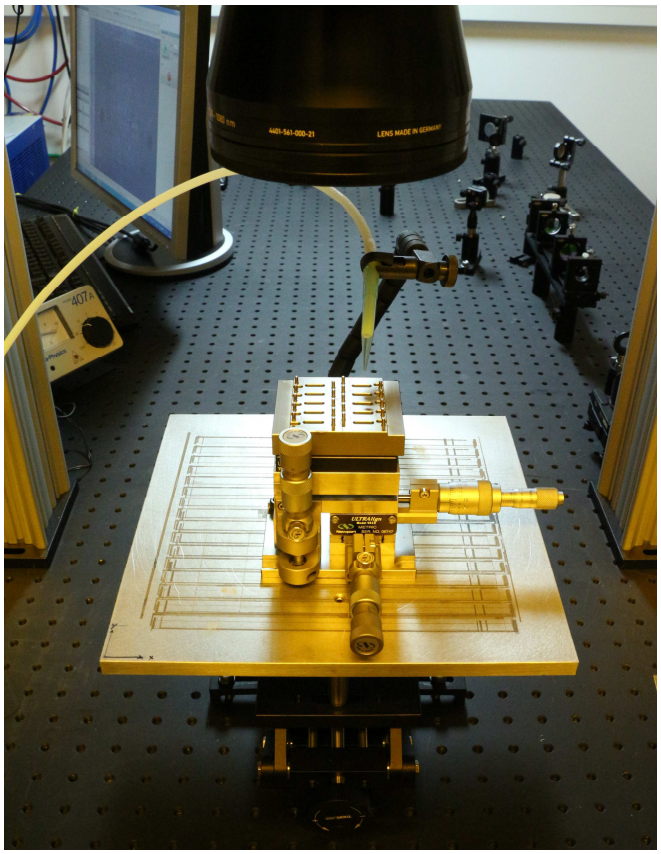

Fig.3.24. Stage and microstage for the sample to be irradiated. The focusing lens is also visible on top side.

Experimental parameters of laser sintering are classified according to different substrates. It should be noted; the Si substrate is used to earn more experience of laser sintering or spin-coating.

A.1. Glass Substrate

substrate	parameters	values
Glass	repetition rate	2MHz, 500 KHz, 250KHz
	laser power(%)	25,30, 35, 36, 37, 38, 39, 40, 42, 43, 44,45,46,54,56
	galvo Scanner speed(m/s)	0,01, 0,02, 0,03, 0,04, 0,05
	jump speed(m/s)	0.05
	lateral distance(µm)	30, 50, 100, 120, 140, 160, 180, 200
	optic lens focus(mm)	330
	focus(over optic table)(mm)	105,125
	number of overscan	1,2,3,4

A.2. GaAs Substrate

substrate	parameters	values
GaAs	repetition rate(MHz)	2 to 50 MHz
	laser power(%)	from 30% to 40%
	galvo Scanner speed(m/s)	0.01 to 1
	jump speed(m/s)	0.05
	lateral distance(µm)	5, 10, 30 and 40
	optic lens focus(mm)	100, 330
	focus(over optic table)(mm)	125
	number of overscan	with best focus, +0.5 mm and −0.5 mm

A.3. Si Substrate

substrate	parameters	values
Si	repetition ate	50 MHz
	laser power(%)	from 34% to 50%
	galvo Scanner speed(m/s)	0.01 to 0.1
	jump speed(m/s)	0.05
	lateral distance(µm)	30, 100, 120, 140, 160, 180, 200
	optic lens focus(mm)	100
	focus(over optic table)(mm)	with best focus
	number of overscan	1,2

3.5 Post Processing

Patterning copper nanoparticles (CuNPs) film can be achieved by laser sintering, thereafter the removal of non-sintered nanoparticles can be achieved by rinsing and what should remain on the surface is the designed layout.

3.5.1 Rinsing and Drying

Non-sintered nanoparticles are removed with Ethanol 99% by placing the wafer for 15 minutes in ultrasonic bath vertically.

3.5.2 Annealing GaAs Substrate

For increasing the adhesion and decreasing the contact resistance in some cases post annealing was done, with different temperatures from 100 to 300 °C under vacuum or argon atmosphere (in glovebox) from 15 minutes to 15 hours.

4. Results

4.1 Glass Substrate

As previously mentioned, NPs ink was printed on glass substrate to investigate the lowest available sheet resistance. Hence by ink-jet printer some squares (10mm×10mm) were printed on the microscope glass slides. Before printing the glass slides were cleaned with ultrasonic bath of ethanol and acetone for 10 minutes for each solvent, afterwards dried with air gun.

Thickness and Homogeneity Variation of Printed Copper(Inkjet)

After finding the best parameters of inkjet with commercial ink CI-005 on glass substrate, these parameters remained constant and varied just the stage temperature and the number of printed layers.

Variation of Stage Temperature

Fig.4.1. shows samples printed on a heated stage at 30 °C had an inhomogeneous thickness ranging from 2.5 to 3µm. It is demonstrated that, the copper tends to concentrate in the center and the edges of the printed pattern (square) were not sharp.

For the samples printed on a stage heated at 60°C, the thickness in the center was more homogeneous and around 1.5 µm. On the edges of the printed square, there is much more material and copper aggregated on sides.

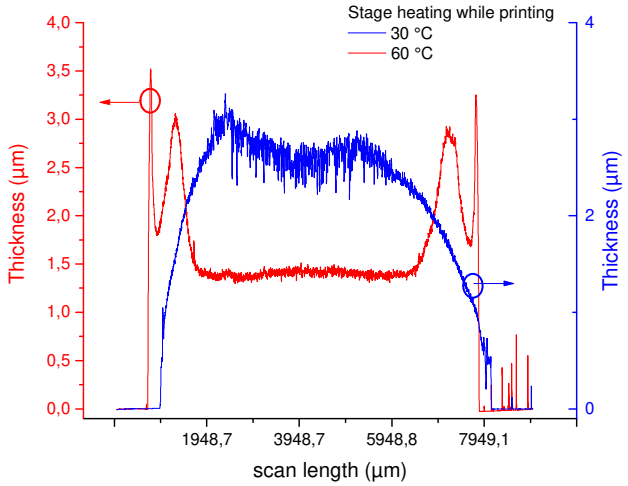

Fig.4.1. Thickness of one layer printed copper on glass with 30°C and 60°C heated stage (before sintering).

Variation of Printed Layers

Printing for second time on heated stage 30°C and 60°C were performed with the same parameters as previous printing, on 60°C heated stage two layers were printed as well. The thickness of printed copper is indicated in Fig.4.2.

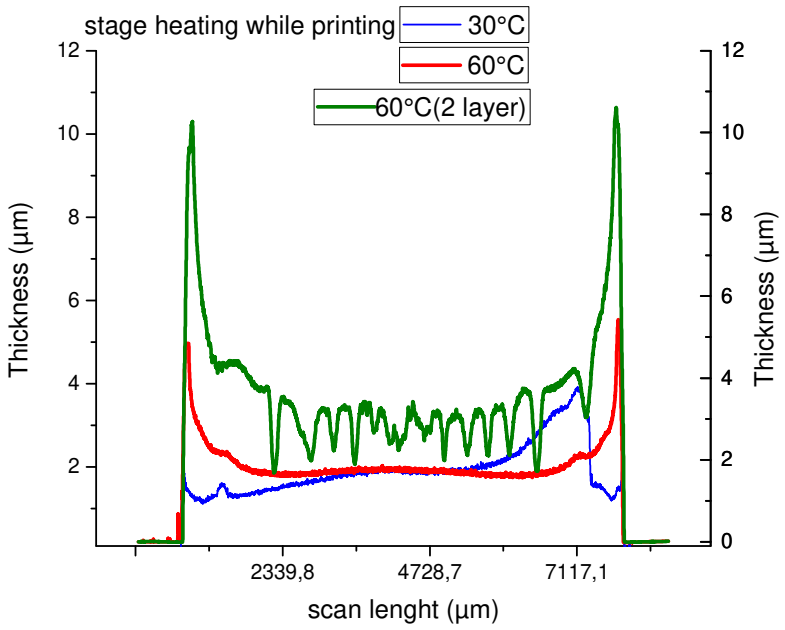

Fig.4.2. Thickness of printed copper on glass with 30°C and 60°C heated stage and two layers (before sintering).

Samples printed on a heated stage at 30 °C had an inhomogeneous thickness ranging from 1.24 to 3.84 µm. Unlike the prior printing.

For the samples printed on a stage heated at 60°C, the thickness in the center is around 2µm. The thickness is few hundreds of nm higher than in previous experiment nevertheless they are comparable.

For the samples printed two times (two layers) on a stage heated at 60°C, wrinkles were observed resulting in an inhomogeneous thickness in the center ranging from 2 to 4 µm. On the edges of the printed square, there is much more material with thickness of about 10.5 µm.

Since the thickness of printed samples at 60 °C is more reproducible than the ones printed at 30°C, therefore for the next experiments just at 60°C would be used.

Identification and Optimization of Laser Sintering Process Windows and Corresponded Sheet Resistance (non-sintered/ sintered/damaged)

This study presents an experimental investigation of the sintering with picosecond pulsed laser with different optic lenses to determine the right processing windows for Cu NPs. The processing windows depend on several parameters such as Cu layer thickness, thermal conductivity of substrates, ambient and laser exposure durations.

The pulsed laser sintering results have been classified into three broad categories:

1- Non sintered printed layer, which was not affected by the incident laser power.
2- Sintered printed layer, which showed significant necking between the particles (increase of the domains of the nanoparticles or in other words small fusion.
3- Ablation/damage, are the results of fast evaporation of organic materials during the sintering process, in some cases damaging the substrate.

Since the glass has a low thermal conductivity, therefore during the sintering process glass stores heat to raise the bed temperature. Hence this process couldn't be performed with high repetition rate like 50MHz, and it has been done between 100 kHz and 2MHz.

As the first result, it became clear, which parameters of the laser would cause the layer to be damaged during the sintering:

- High repetition rate, such as 50 MHz, especially for inhomogeneous samples (printed samples on 30°C heated stage).
- High Galvo scanner speed (scanning speed), such as 0,25m/s, due to low thermal conductivity of glass the heat couldn't be dissipated by high scanning speed through glass and leads to ablation or damaging the printed layer.
- High laser power in sintering process with 2MHz repetition rate, such as more than 38% for homogeneous(60°C) samples and more than 36% for inhomogeneous(30°C) samples, because of different thickness of printed layer the threshold of damaging would be different.

Variation of Lateral Distance* (The Distance Between the Scan Lines of Laser)

The printed Cu layers on 30°C and 60°C heated stage were sintered with different lateral distance between 100 to 200 µm. Note, that other parameters of laser sintering were constant.

Lateral distance is the distance between the scan lines of the laser

The effect of lateral distance on sintering quality on 30°C and 60°C heated stage is indicated in Fig.4.3. and Fig.4.4. respectively. So that, by larger distance, the sintering lines become more pronounced. Regardless of the temperature of the stage, the sintered layer by 100 µm lateral distance seems more homogeneous than that of 200 µm. Since, by smaller lateral distance, the printed area would be sintered

by more laser beam lines, thus more Cu NPs were exposed directly to the laser beam and this resulted in better sintered layers.

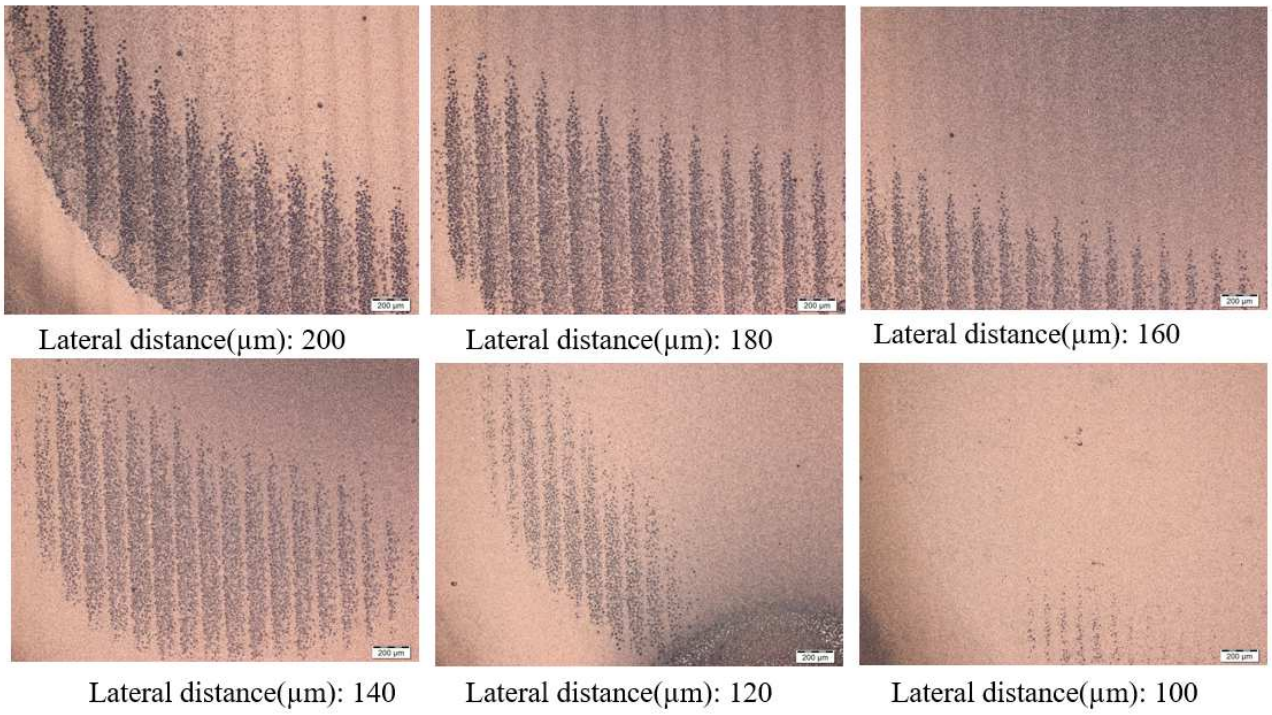

Fig.4.3. Effect of lateral distance on samples printed at 30 °C.

As presented in Fig.4.3. some small blisters are observed , which result from excessive heating and evaporation of the organics primarily from the outermost ink layer, forming a compact metal barrier. This process, which concludes rapidly, locks up the organic gas which forms in the interior and cannot break through the top layer. Eventually a high gas pressure is formed within the heated ‘gas pocket’ (small blisters).

As the printed layer on 30°C heated stage has non-homogeneous thickness and thicker layer in the center of the printed layer as well, blisters are seen more in this type of samples. By decreasing the lateral distance, the sintering quality was improved and no delamination of layers was seen and consequently, less sheet resistance is expected.

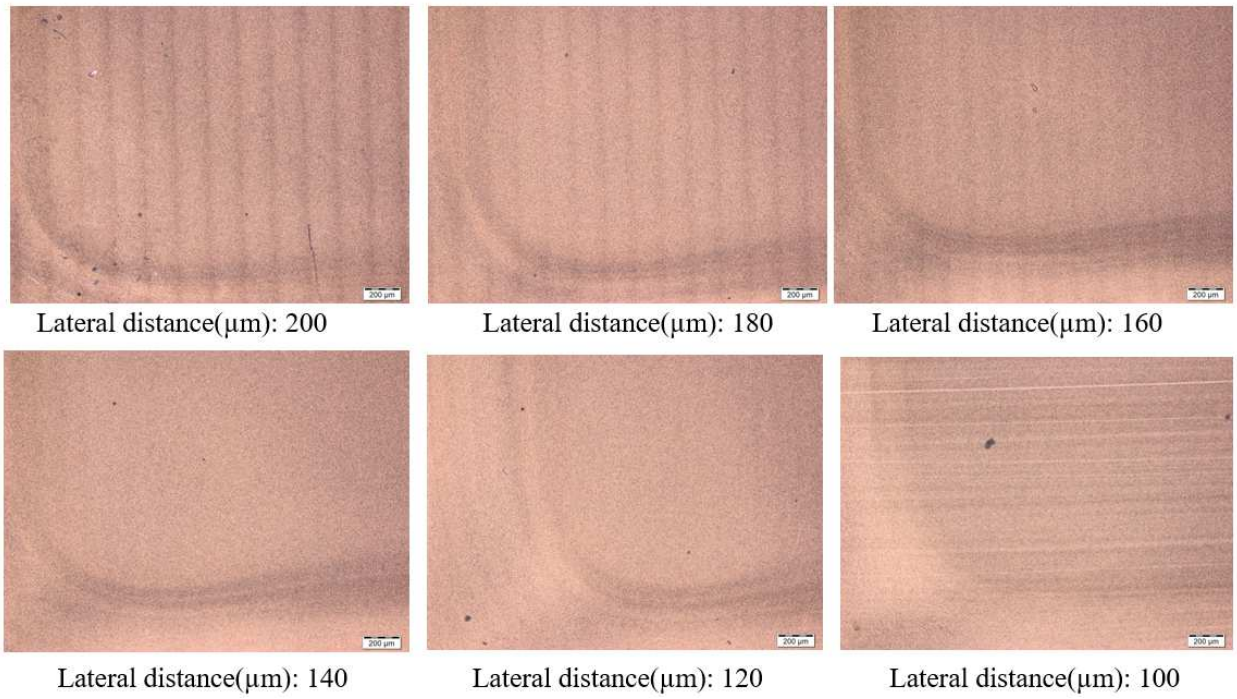

Fig.4.4. Effect of lateral distance on samples printed at 60 °C

The printed layer on 60°C heated stage is more homogenous, therefore there is no delamination of layers, and by decreasing the lateral distance, the sintering quality is improved.

In general, the sheet resistance is proportional to thickness of printed layer. According to the performed experiments, it has been demonstrated that, thicker printed layer has lower sheet resistance.

According to the performed experiments, it has been mainly identified that, regardless of the temperature of the stage during printing:

- Sheet resistance varies slightly with the lateral distance between the scanning lines.
- Sheet resistance decreases with increasing the power of the laser for the same later distance.
- Sheet resistance is proportional to thickness of printed layer (Sheet resistance decreased by increasing the thickness and conversely).

Sheet resistance of two types of printed layers versus the lateral distance and laser power is depicted respectively in Fig.4.5. a) and b). It is noteworthy to mention, the thickness of samples on 30°C and 60°C are about 2.5 to 3µm and 1.5 µm and the laser parameters are listed in table as below:

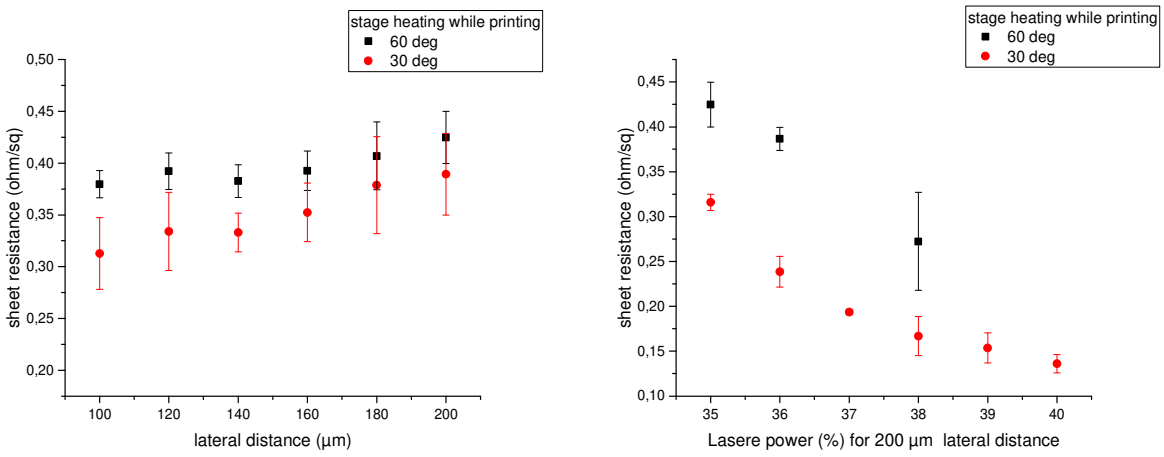

a) b)

Fig.4.5. Variation of sheet resistance versus a) lateral distance and b) by laser parameters of table.

Repetition Rate (MHz)	*Current(A)*	**Laser power*		*Galvo Scanner Speed(m/s)*	*Jump speed (m/s)*	*Focus (over the optic table)(mm)*	*Optic lens(mm)*	*Over scan*
		(%)	(W)					
2	40	35	1,8	0,01	0,05	125	330	1

With 2MHz repetition rate, for low power (smaller than 34%), the samples were not sintered and for high power (more than 39%), the samples were completely damaged.

Since the thickness of the Inkjet printed samples at 60 °C is more reproducible than the ones printed at 30°C, for the next experiments the former condition (i.e. 60 °C) will be used.

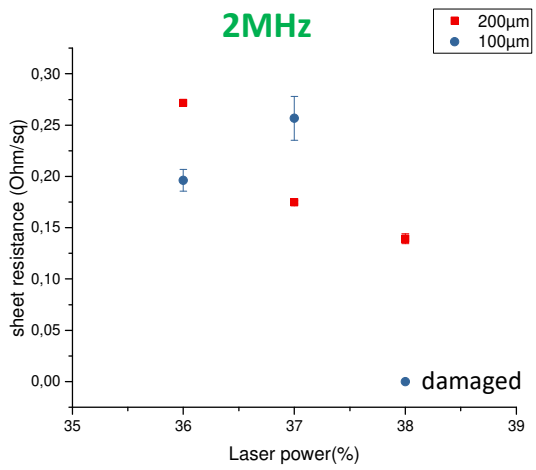

Repetition Rate	2MHz
Current(A)	40
laser power	from 36% to 38%
Galvo Scanner Speed(m/s)	0.01
jump speed	0.05
Focus (over optic table) (mm)	125
optic lens (mm)	330
Over scan	1

Fig.4.6. Variation of sheet resistance versus laser power for samples printed on 60°C stage

As mentioned above, for these samples printed in two layers on heating stage with 60°C, the thickness of the film ranged from 2 to 4 µm. Fig.4.6. shows that, with 200 µm lateral distance, for

* *at 40(A)current, the laser power 35% is corresponding to 1.8W.*

low power (smaller than36%), the samples were not sintered and for high power (more than 38%), the samples were completely damaged. The sheet resistance ranged from 0,14 Ω/☐ to 0,27 Ω/☐ for values of the laser power between 36% and 38%.

With 100 µm lateral distance, for low power (smaller than36%), the samples were not sintered and for high power(more than 37%), the samples were completely damaged, and the sheet resistance ranged from 0,20 Ω/☐ to 0,26 Ω/☐ .

Complementary experiments were performed to demonstrate the effect of different parameters of the laser. By decreasing the lateral distance of laser beam lines, the damage threshold with changing laser power becomes low. This means with larger lateral distance a higher laser power can be used. (when other parameters remained fixed)

As is shown in Fig.4.7. at 100µm lateral distance the damage threshold of samples begins at 37% but for 200µm at 38%.

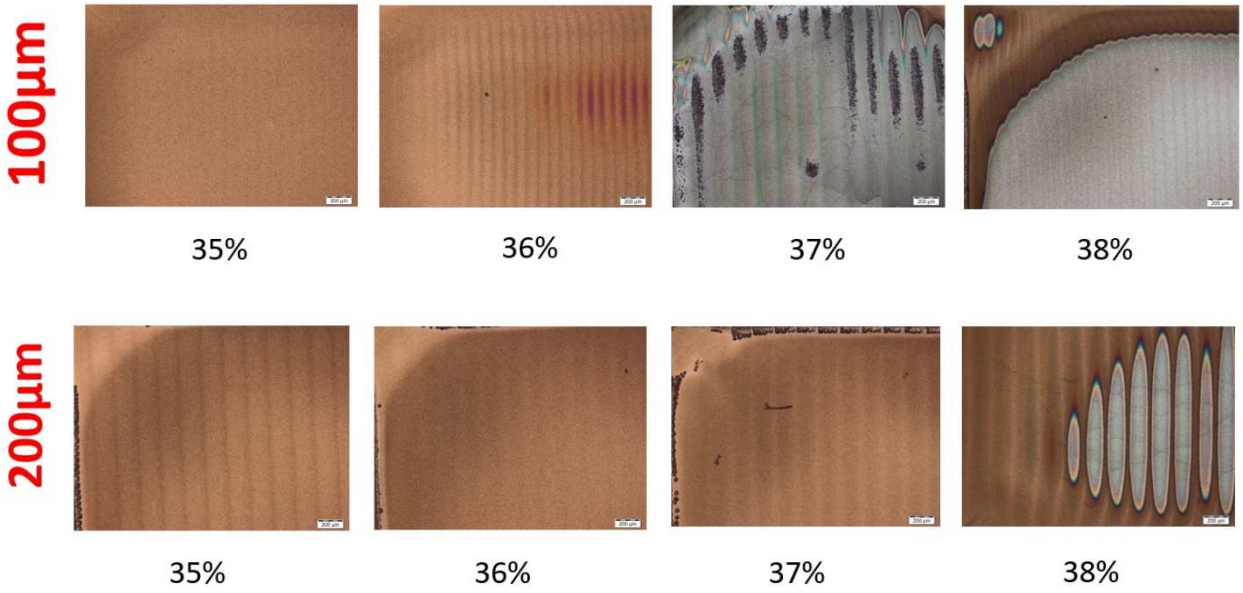

Fig.4.7. Effect of different lateral distance on variation of the damage threshold (one layer samples)

This effect was observed in samples with 2 layers printed as well. Although the thickness of these samples is double, the damage threshold with the same laser parameters isn't very different from one layer printed samples.

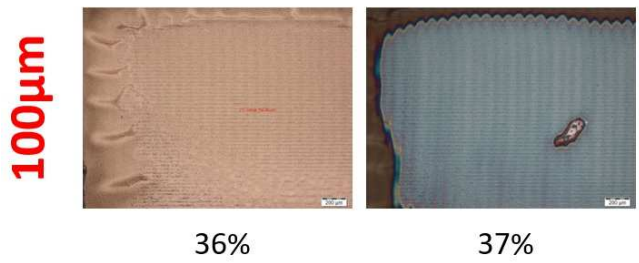

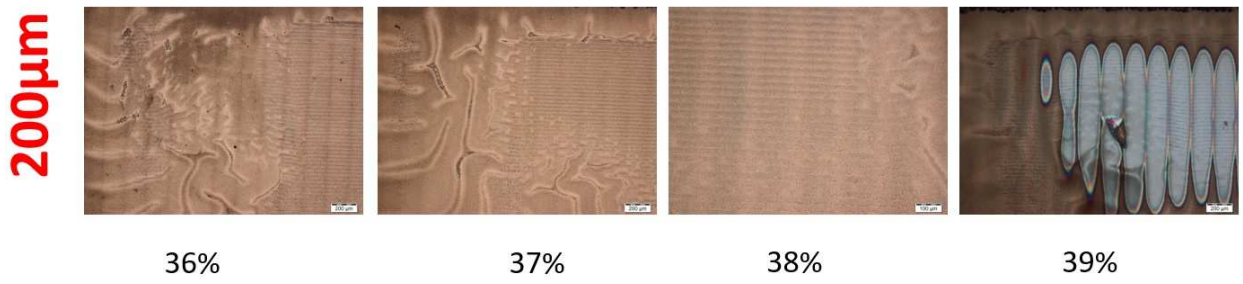

Fig.4.8. Effect of different lateral distance on variation of the damage threshold (two layer samples)

AFM images, which were taken before and after sintering process (see Fig.4.9) show the distinction between sintered and non-sintered particles. For samples, which were sintered with 30% laser power, 2 MHz repetition rate and 100 µm lateral distance, similar morphology is obtained as compared to the non-sintered copper nanoparticles. For 35% and 36% laser power, there is a small increase of the domains of the nanoparticles (small fusion). At37% laser power damages the film, and different morphology is obtained.

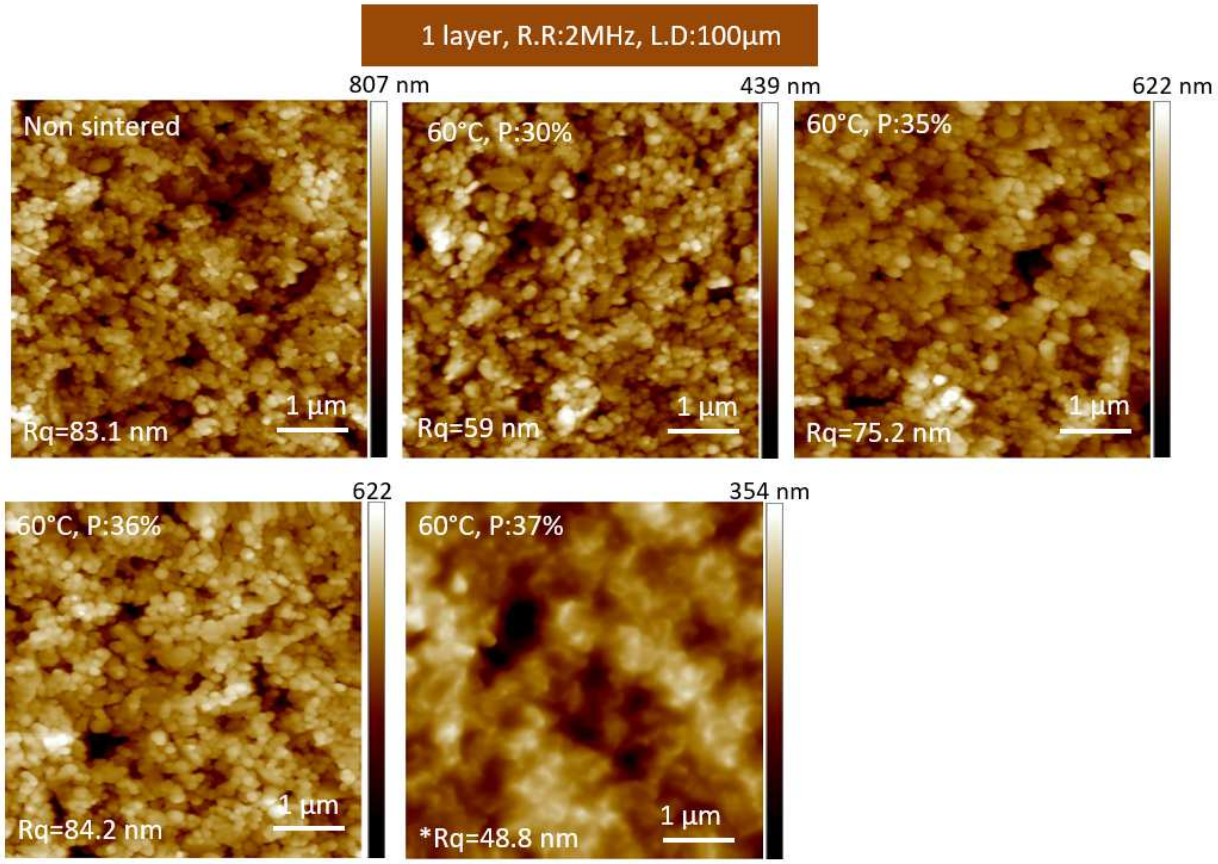

Fig.4.9. Morphological images of printed copper before and after sintering with different laser power

*RMS Roughness(Rq):is the root mean square average of the profile heights over the evaluation length

For laser sintering with 200 µm lateral distance and 2 MHz repetition rate, the domains of the nanoparticles increase very slight. No clear difference is seen between the sintering at 35% and upon increasing it to 38% (see Fig.4.10).

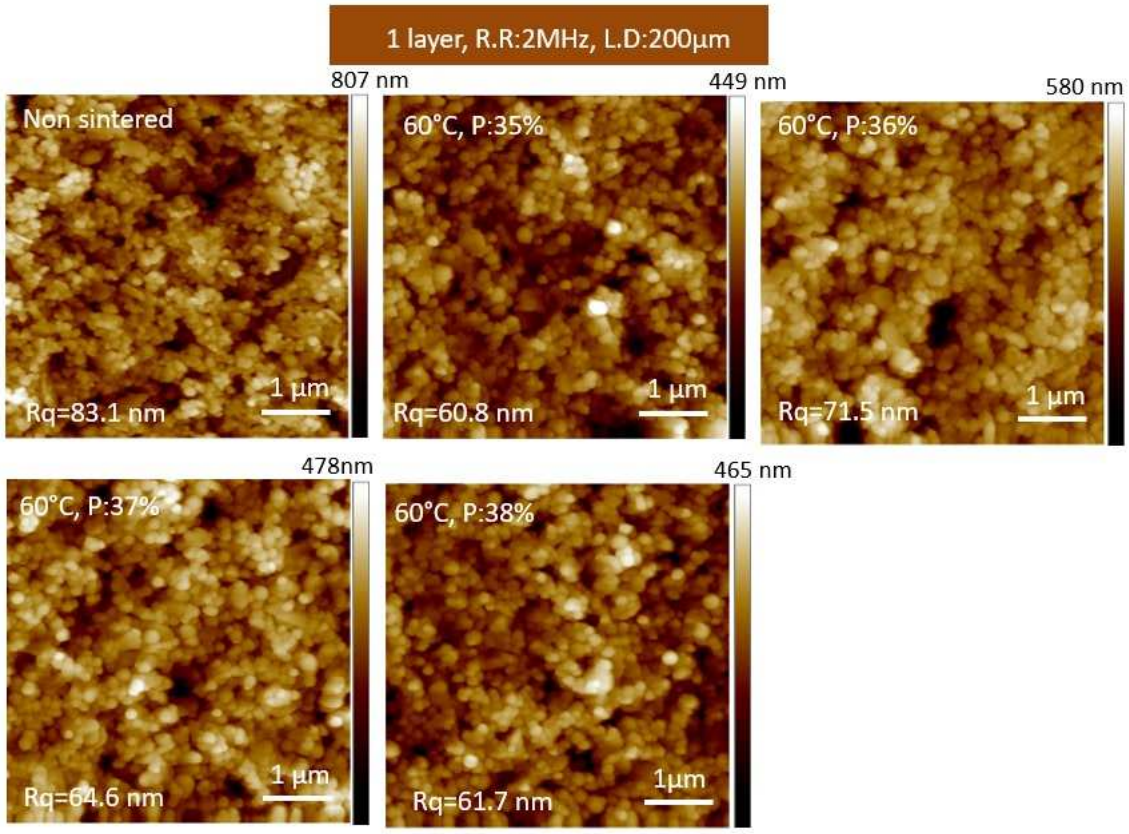

Fig.4.10. Morphological images of printed copper before and after sintering with different laser power

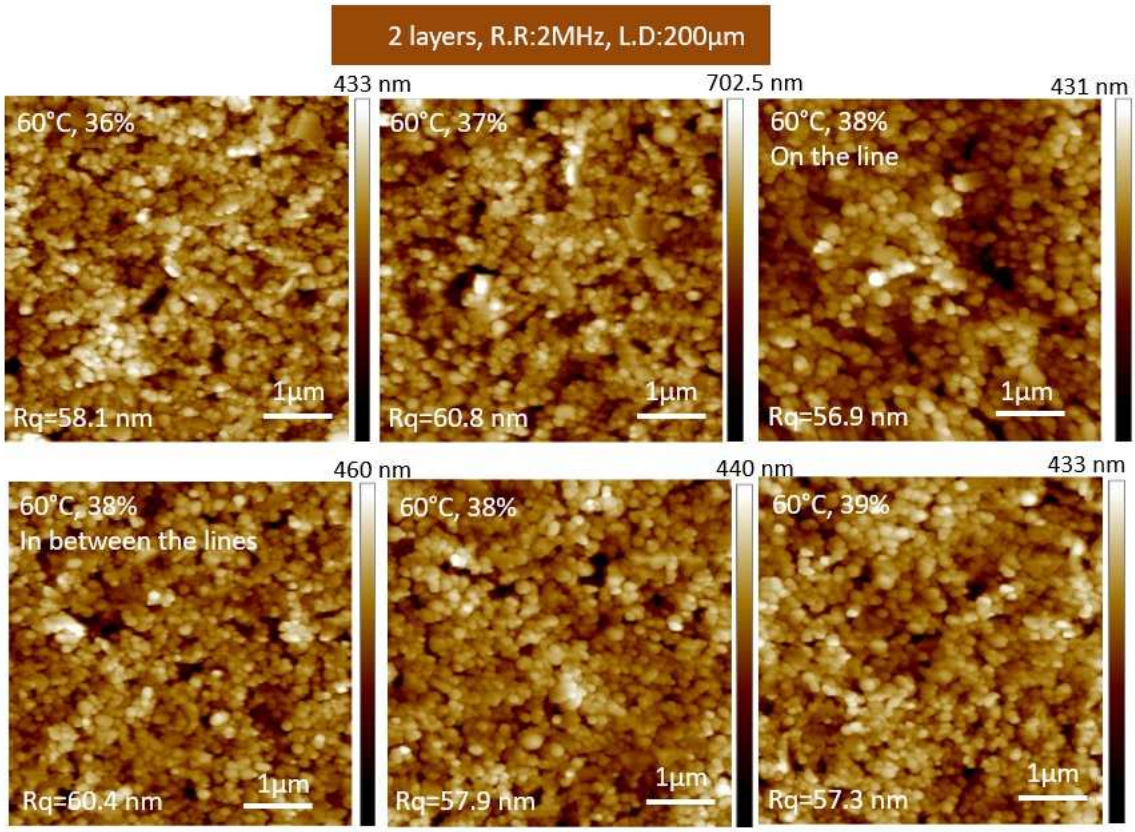

Fig.4.11. Morphological images of printed copper before and after sintering with different laser power

For two layer samples with 2MHz repetition rate and 200µm, at 36% laser power, the morphology is very similar to the non-sintered samples. At higher laser power >37% the domains slightly increase. It is interesting to note that, the sintering is not homogeneous. If the AFM-scan is acquired in between the laser sintering lines, the morphology looks like the non-sintered one (see Fig.4.11.)

As indicated in Fig.4.12. for two layer samples with 2MHz repetition rate and 100µm lateral distance, similar results are obtained. Slight increase of the domains of the nanoparticles if sintered at a laser power of 37%. The zoom in image shows fusion/aggregation of nanoparticles. The graph shows the profile of a cross section (orange line).

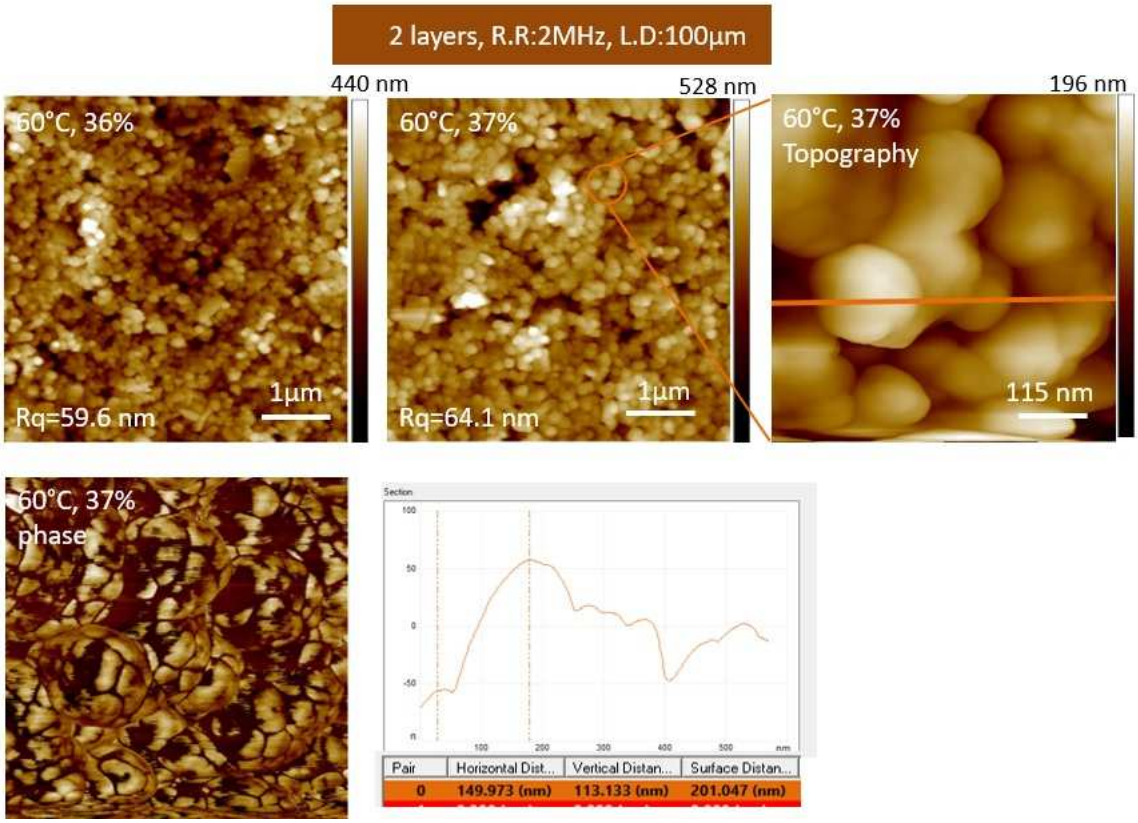

Fig.4.12. Morphological images of printed copper before and after sintering with different laser power and section image to define the thickness of sintered copper nanoparticles

In the next step the sintering process was carried out with lower laser repetition rate such as 250 KHz and 500 KHz. It allows us to utilize higher laser power in percent and we expect also to gain lower sheet resistance (see Fig.4.13.).

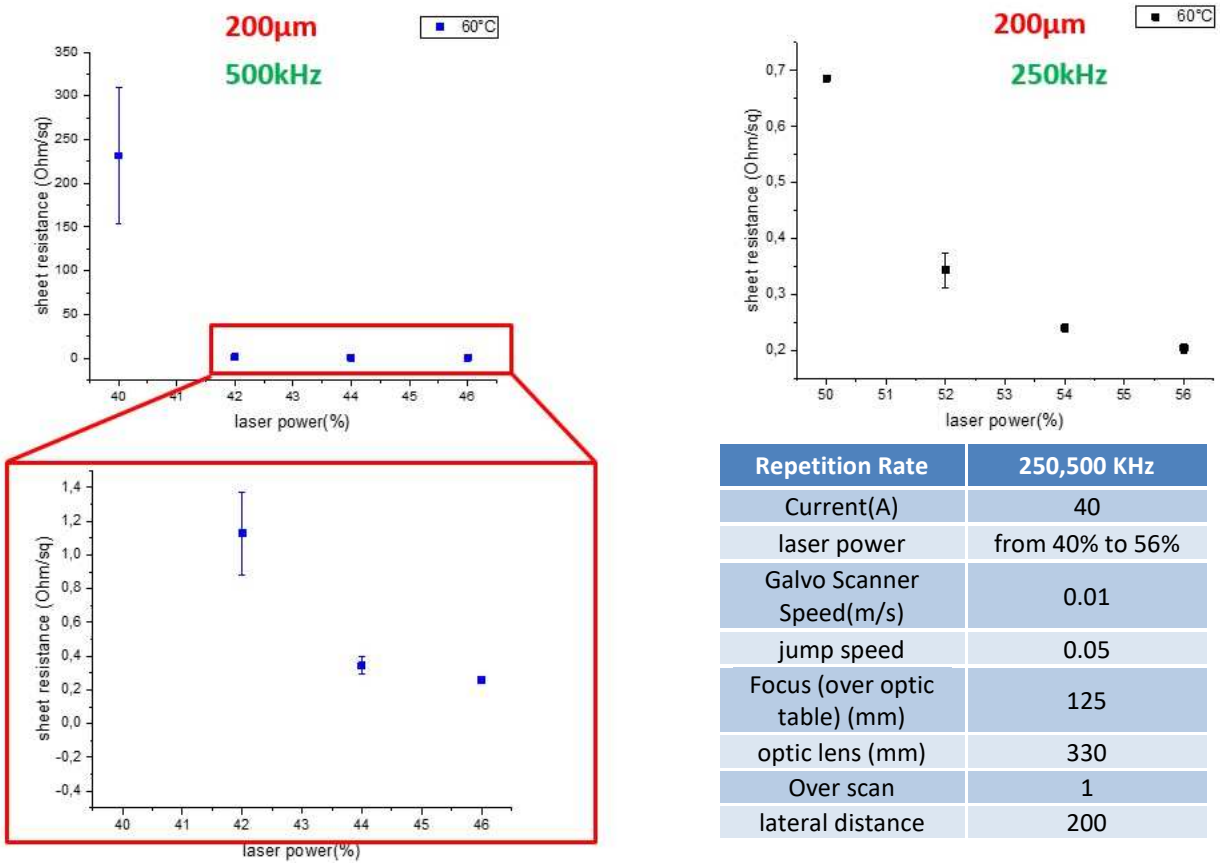

Repetition Rate	250,500 KHz
Current(A)	40
laser power	from 40% to 56%
Galvo Scanner Speed(m/s)	0.01
jump speed	0.05
Focus (over optic table) (mm)	125
optic lens (mm)	330
Over scan	1
lateral distance	200

Fig.4.13. Variation of sheet resistance versus different laser power at 250 and 500 kHz repetition rate and at a lateral distance of laser lines of 200µm.

With 500KHz repetition rate for low power (smaller than42%), the samples were not properly sintered and the average sheet resistance was 231 Ω/☐. Then the sheet resistance decreases with increasing the laser power up to 46 %. Higher than that, the samples are damaged.

With 250KHz repetition rate for low power (smaller than50%), the samples were not properly sintered and the sheet resistance decreases with increasing the laser power up to 56 %. Higher than that, the samples are damaged.

The sheet resistance of one and two layer samples, which were sintered under ambient at different repetition rate and laser power, are summarised in the following tables.

Sheet resistance summary of samples printed at 60°C and sintered with 2MHz repetition rate:

lateral distance	100µm			200µm		
60°C	laser power(%)		sheet resistanceΩ/☐	laser power(%)		sheet resistanceΩ/☐
	20	not sintered		20	not sintered	
	25	not sintered		25	not sintered	
	30	not sintered		30	not sintered	
	35		0,3727	35		0,4471
	36		0,3197	36		0,2868
	37	damaged		37		0,2253
	38	damaged		38	damaged	

Sheet resistance summary of samples printed at 60°C and sintered with 500 and 250 kHz repetition rate:

500kHz repetition rate			
lateral distance	200µm		
60°C	laser power(%)		sheet resistanceΩ/☐
	40		231,62*
	42		1,1285
	44		0,3454
	46		0,2567

250kHz repetition rate			
lateral distance	200µm		
60°C	laser power(%)		sheet resistanceΩ/☐
	50		0,6859
	52		0,3431
	54		0,2401
	56		0,2039

Sheet resistance summary of samples printed 2 layer at 60°C and sintered with 2MHz repetition rate:

lateral distance	100			200		
60°C	laser power(%)		sheet resistanceΩ/☐	laser power(%)		average sheet resistanceΩ/☐
	36		0,1963	36		0,2718
	37		0,2567	37		0,1748
	38	damaged		38		0,1393
	39	damaged		39	damaged	

**this high amount of sheet resistance was occurred due to non-sintered copper*

Variation of Ambient

Next we consider the role of using different atmosphere in sintering process, the best results from the previous experiment were repeated under Nitrogen, Argon and Air Ambient. Sintering under another atmosphere to avoid oxidation was done with flow box. The sample is placed in glass-box and the gases are flowed while the laser beam is incident. Fig.4.14. compares the results obtained under argon, nitrogen and air with conditions, that are listed in table.

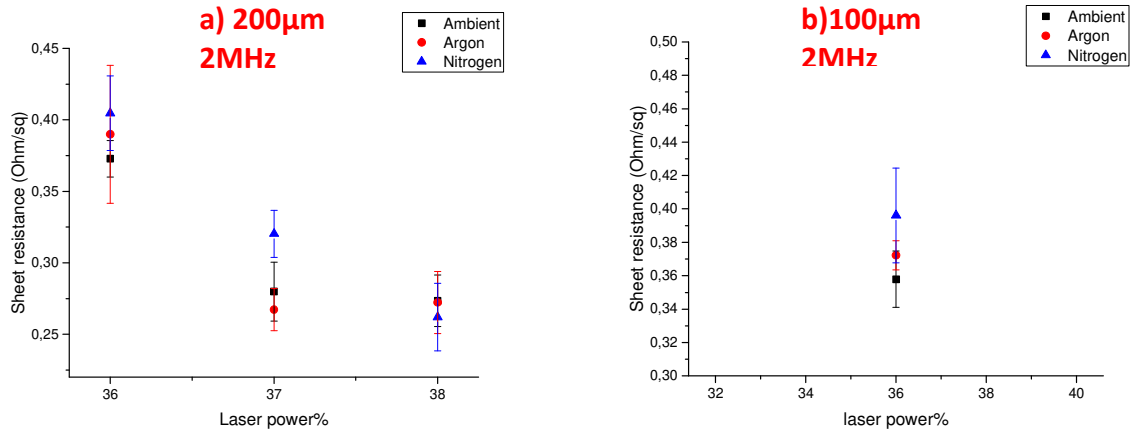

Fig.4.14.Variation of sheet resistance versus different laser power at 2 MHz repetition rate by different lateral distance of the scan lines of the laser under different ambient.

Under different sintering atmospheres, for 36 and 37% laser power, the highest resistance is obtained for sintering under Nitrogen, unlike a 38% laser power where the sintering atmosphere does not seem to influence the sheet resistance. There is no big difference of sheet resistance between different atmosphere.

Repetition Rate	2MHz
Current(A)	40
laser power	from 36% to 38%
Galvo Scanner Speed(m/s)	0.01
jump speed	0.05
Focus (over optic table) (mm)	125
optic lens (mm)	330
Overscan	1
lateral distance	100-200

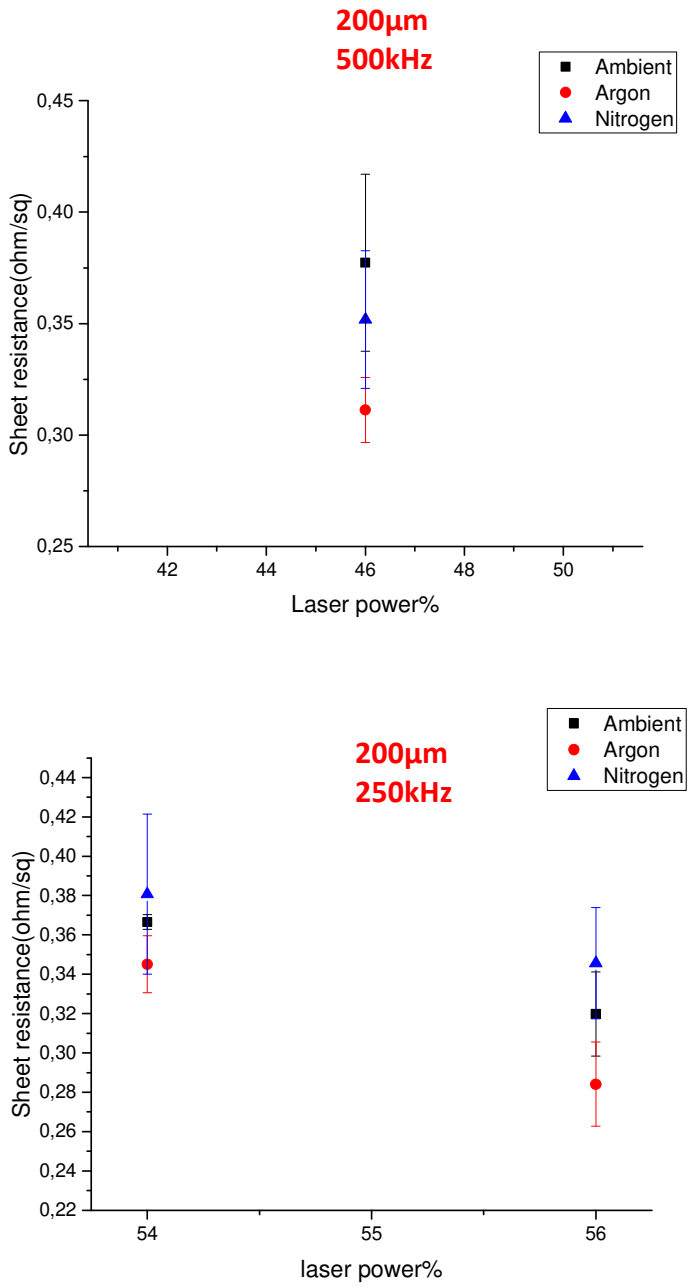

Fig.4.15.Variation of sheet resistance versus different laser power at 250 and 500 KHz repetition rate by different lateral distance under different ambient.

At high percent laser power sintering under Argon has lower sheet resistance and under Nitrogen has higher sheet resistance.

Repetition Rate	250,500 KHz
Current(A)	40
laser power	from 46% to 56%
Galvo Scanner Speed(m/s)	0.01
jump speed	0.05
Focus (over optic table) (mm)	125
optic lens (mm)	330
Overscan	1
lateral distance	100-200

Variation of Scan Speed

Next the effect of variation of scan speed is explored under different ambient. Fig.4.16. shows the results at different speed from 0.02 m/s to 0.05 m/s with different laser power. It should be noted, that in some cases results are not available for all three ambients, because the samples were damaged in the process.

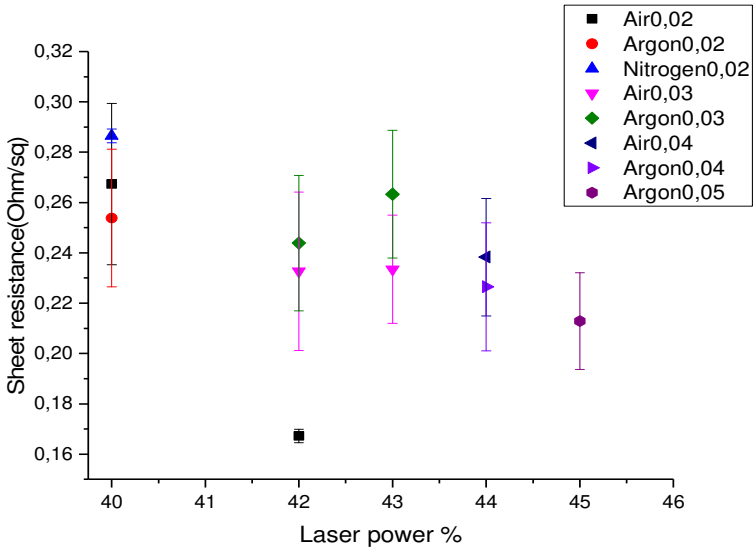

Fig.4.16.Variation of sheet resistance versus different laser power at 2 MHz repetition rate by different scan speed under different ambients.

Repetition Rate	2MHz
Current(A)	40
laser power	from 40% to 45%
Galvo Scanner Speed(m/s)	0.02,0.03,0.04,0.05
jump speed	0.05
Focus (over optic table) (mm)	125
optic lens (mm)	330
Overscan	1
lateral distance	200

By comparing the Sheet resistance of different scan speed, the lowest Sheet resistance occurred at 0,02m/s under air with 42% laser power. Evidently, increasing the scan speed couldn't improve the outcome. As might be expected, with lower scan speed the particles have more time to distribute heating and modify the sintering process.

Variation of Over Scans

To study the effect of over scan on sintering process, on some samples, which were printed on 60°C heated stage, grids were sintered (with line distance of 500µm) with different laser power from 31% to 38%. Then this sintering was repeated for 2, 3, 4 times with the same conditions. Fig.4.17. a) to d) show the sintered samples with one to four over scans respectively.

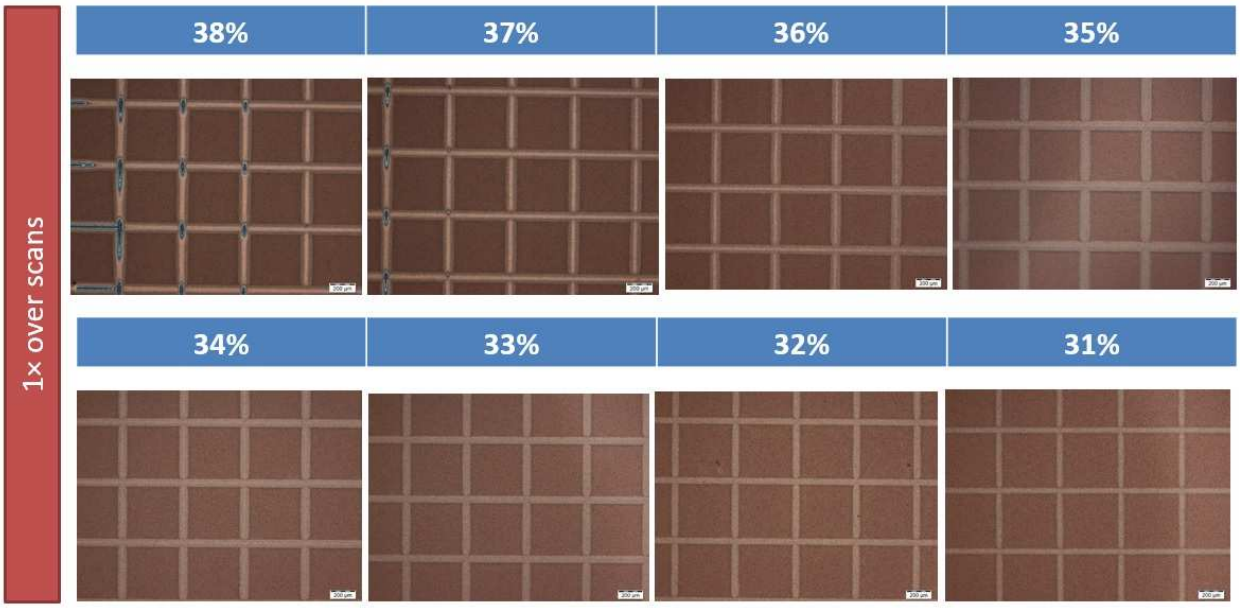

Fig.4.17. a) Patterned grids of printed copper for one time over scan.

After sintering the grids, damaged sintered Copper is observed at the intersection. The best result was obtained at 36% laser power.

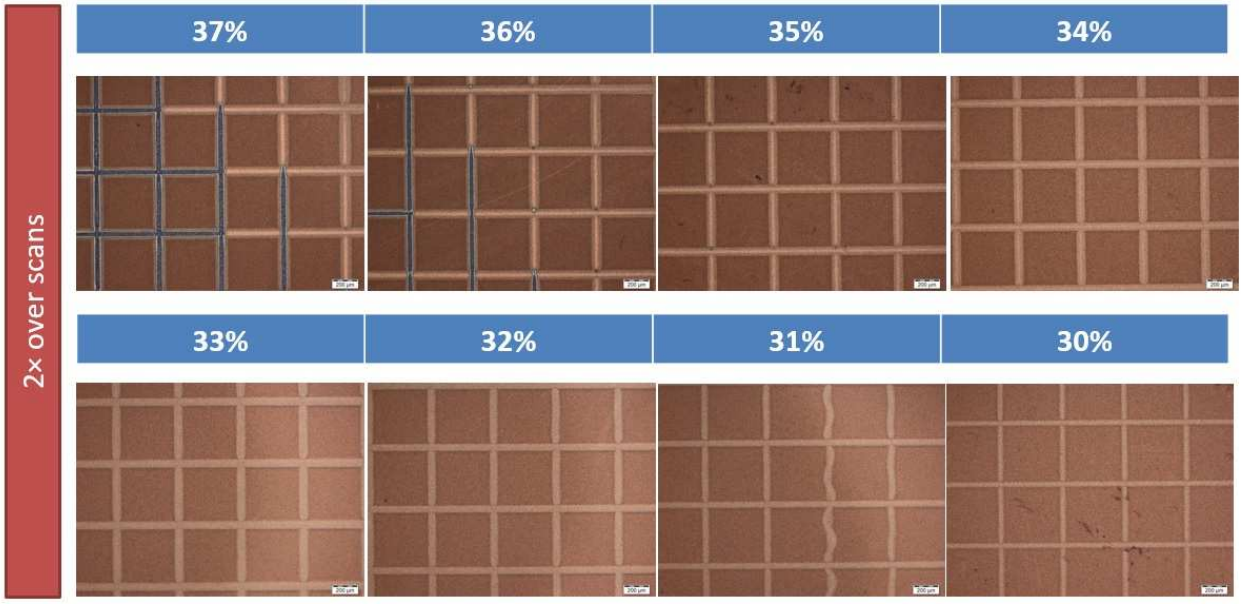

Fig.4.17 b) Patterned grids of printed copper for two times over scan.

By 2 times over scans damaged Copper is seen, when there was more than 35% laser power.

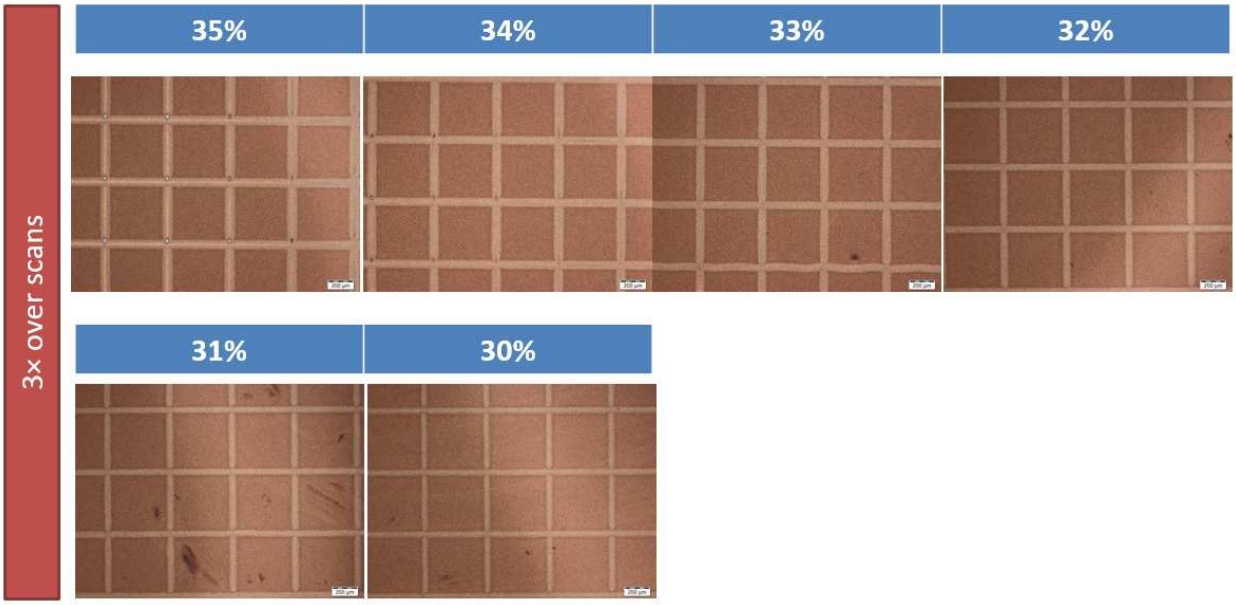

Fig.4.17. c) Patterned grids of printed copper for three times over scan.

By 3 times over scans damaged Copper is seen, when there was more than 34% laser power.

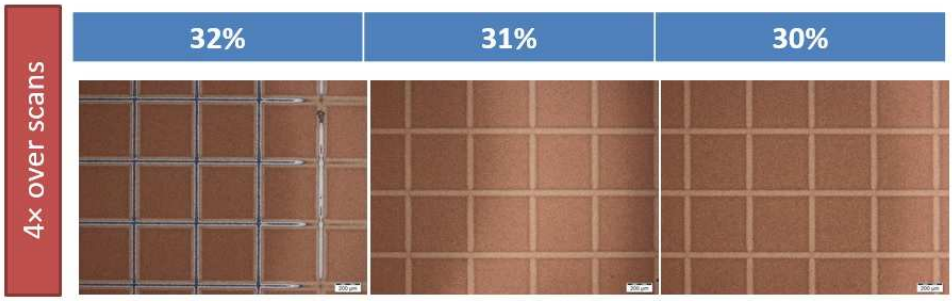

Fig.4.17. a) Patterned grids of printed copper for four times over scan.

By 4 times over scans damaged Copper is seen, when there was more than 32% laser power.

laser parameters of patterning the grids are as below:

Repetition Rate	2MHz
Current(A)	40
laser power	from 31% to 38%
Galvo Scanner Speed(m/s)	0.01
jump speed	0.05
Focus (over optic table) (mm)	105
optic lens (mm)	330
Overscan	1
lateral distance	30

Adhesion Test:

To check the adhesion of sintered copper, non-sintered copper was rinsed with Ethanol 99%, for which the substrate is placed in Ultrasonic bath for 15 min. Afterwards the substrate is dried with air gun. As Fig.4.18. indicates the best results are obtained in one time over scan with 36%, 37% and 38% laser power.

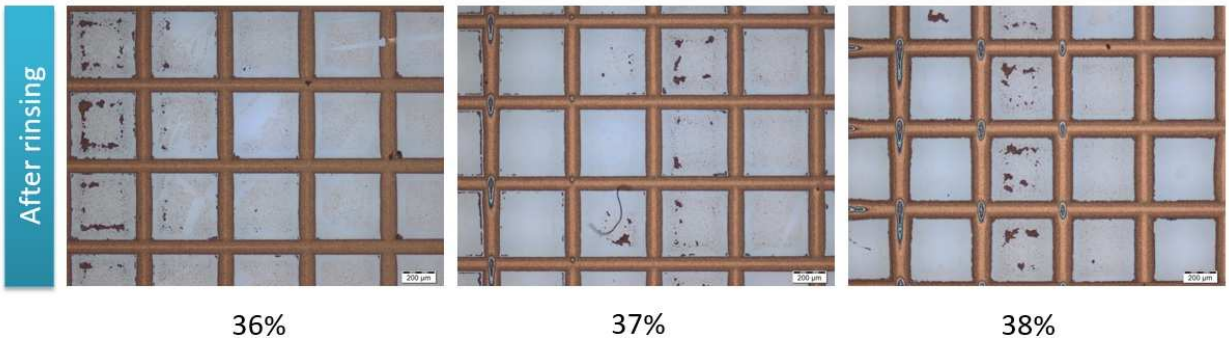

Fig.4.18. Sintered copper NPs after rinsing

To test adhesion, sticky tape is pasted on the copper grids and then the tape is removed. The outcomes are illustrated in Fig.4.19. The best result is attained by 38% of laser power and one over scan.

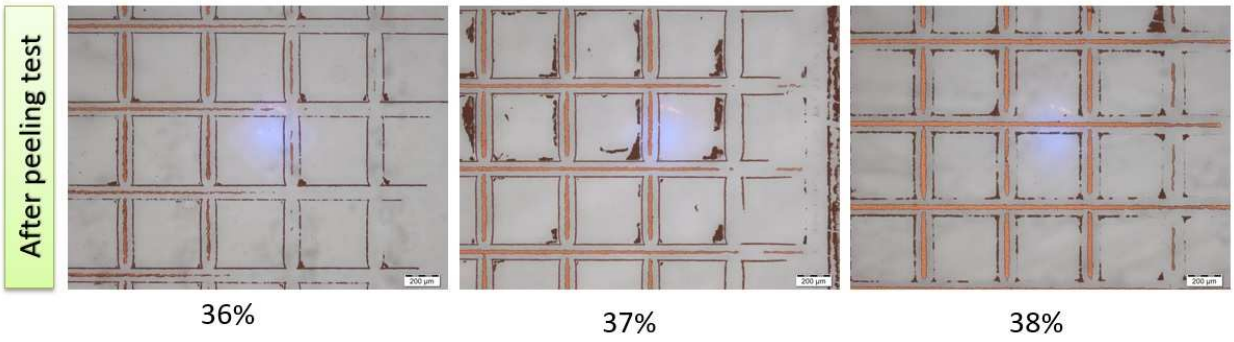

Fig.4.19. Sintered copper NPs after adhesion testing

Copper sintering via increasing the number of over scan couldn't improve the adhesion of sintered copper film and the best result is achieved by using high laser power with one over scan.

Although patterning via laser sintering can provide a high resolution practically, due to the non-homogeneity of the copper thickness on the substrate as a result of inkjet printing, the laser behavior isn't the same on the whole surface. Therefore, after the sintering process on one printed square one can observe some part with high quality sintering and metallic colour of sintered copper and also some damaged part. This might be because of the slight variation of thickness.

4.2 GaAs Substrate

Thickness and Homogeneity of Printed Copper by Ink Jet Printing

After finding the best parameters of inkjet with commercial ink CI-005 on the GaAs substrates, some squares were printed by using the printing parameters, which are mentioned in chapter three. Since the thickness of printed layer of copper by inkjet is non homogenous, another type of printing with more homogeneity like spin-coating was examined.

a. Variation of Thickness (Coffee Ring) by Ink Jet Printing

Samples were printed on a heated stage at 30 °C. As is shown in Fig.4.20. the thickness in the center ranges from 0.3 to 0.5 µm but on the edges of the printed square from 0.45 to 0.7 µm (much more material has been observed there). The thickness is about few micrometers lower than on the previous experiment on glass substrate. For a larger pattern the coffee ring is wider and larger from the edges which leads to less material in the middle and therefore thinner layer in the center.

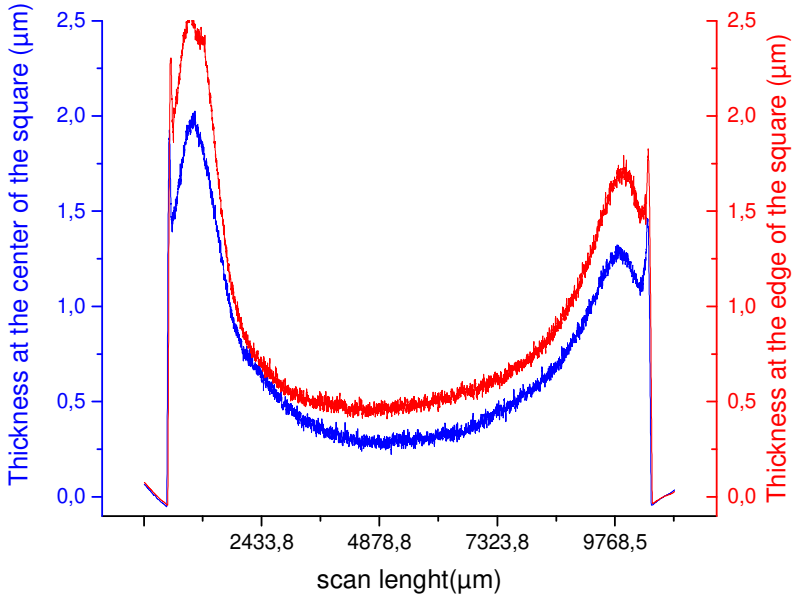

Fig.4.20. First inkjet outcome of printed copper nanoparticles ink on GaAs Freiberger wafer

The second try to print copper nanoparticles ink by inkjet on GaAs is illustrated in Fig.4.21. The thickness in the center of the first spot and the second spot ranges from 0.3 to 0.6 µm (like in the previous experiment).

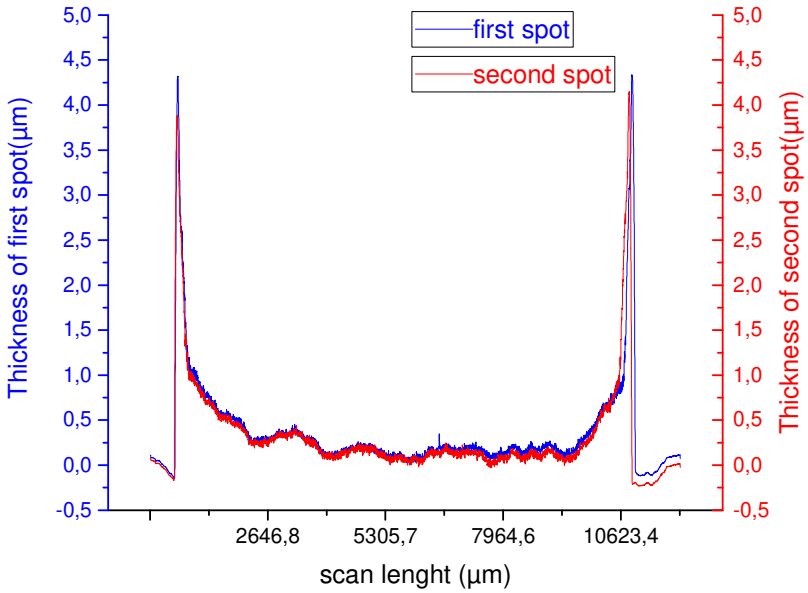

Fig.4.21. Second inkjet outcome of printed copper nanoparticles ink on GaAs Freiberger wafer

b. Variation of Thickness by Spin Coating Printing

To reach a more homogenous printed layer the spin- coating was performed. The thickness could be controlled with variety of speed and duration time. The samples were printed according to printing parameters, which are mentioned in chapter three. The thickness of the printed thin layer depends on spin speed and spin duration.

The first try was done in two-steps coating: 500 rpm for 5 seconds, then 2000 rpm for 30 seconds. Then the sample is dried in the oven for 2 hours and 30 minutes at 50°C. Next the thickness in different places of the wafer was measured in five spots (center, right, left, top, bottom) and the results are depicted in Fig.4.22. and Fig.4.23. The thickness ranges from 300 to 400 nm.

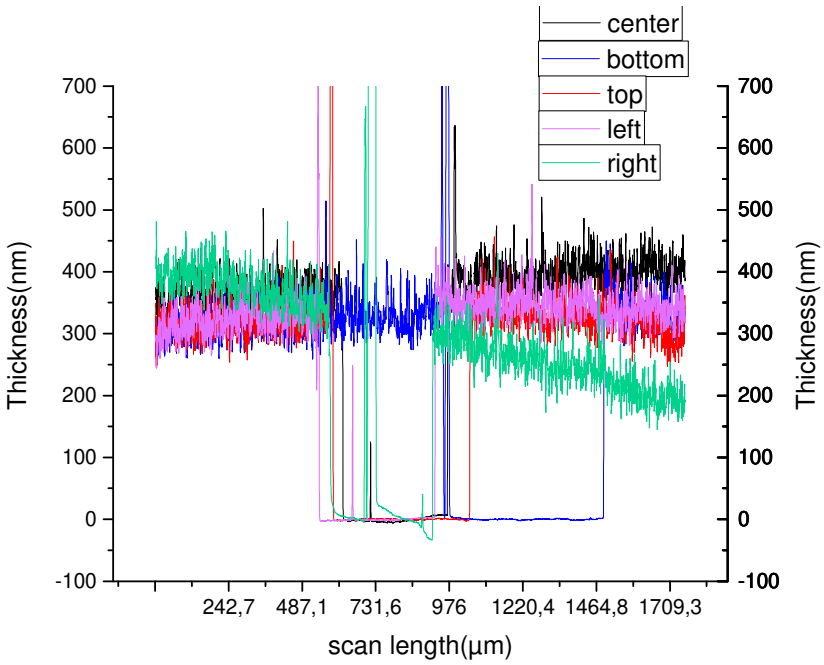

Fig.4.22. Shows the thickness variation in two steps coating: 500 rpm for 5 seconds, then 2000 rpm for 30 seconds

The next experiment was carried out in one-step coating: 3000 rpm for 30 seconds. The thickness of printed copper in the second sample is ranges from 100 to 200 nm.

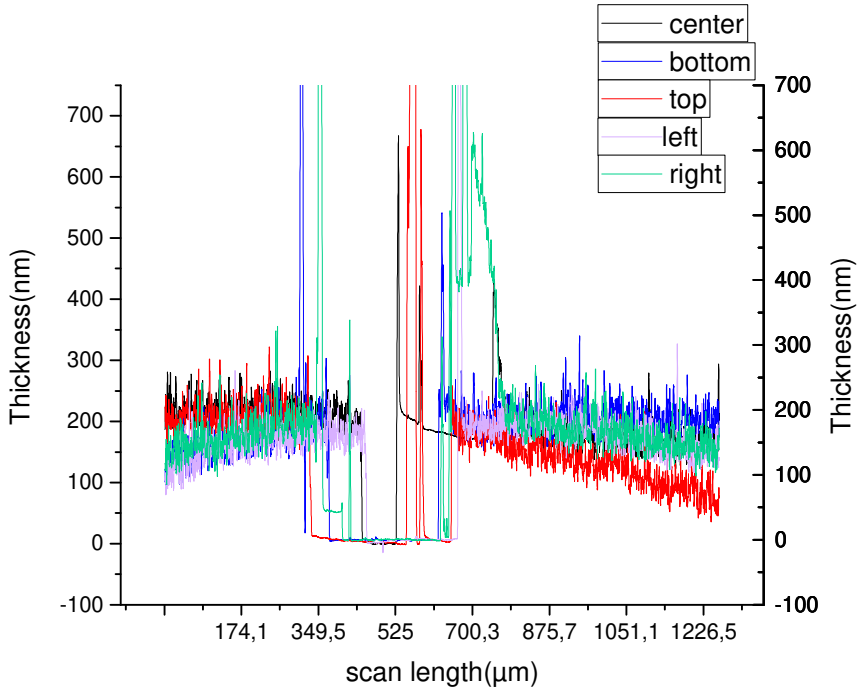

Fig.4.23. Shows the thickness variation in one step coating: 3000 rpm for 30 seconds

To investigate the variation of thickness in spin-coating technique, some samples were produced, the outcomes are depicted in the table. It is shown that, the printed layers are more homogenous and it could be providing more laser sintering efficiency.

experiment	*ASH1(nm)	ASH2(nm)	ASH3(nm)	Average
1	222	189	205	205,33
2	250,9	232,8		241,85
3	220,69	252,7		236,70
4	279,1	243,2	248,5	256,93

c. Identification and Optimization of Laser Sintering Process Windows (non-sintered/ sintered/damaged)

The first sintering process was done with the best parameters of Copper sintering on glass under ambient condition, (repetition rate: 2 MHz, scan speed: 0.01m/s, jump speed: 0.05m/s, lateral distance: 30µm, laser power: from 30% to 38%, over scan: 1 time, focus (over the optic table):105mm, optic lens: 330mm) but these parameters couldn't provide a good sintering result, which could be due to different thermal conductivity (glass:0.8 W/Km, GaAs: 45.5-46 W/Km). GaAs substrate with higher thermal conductivity dissipates the heat, thus samples on GaAs substrate require much higher irradiance for sintering of NPs than is required for samples on glass substrates. Then different repetition rate was examined, and the best result was obtained at 50 MHz.

c-1) Variation of Thickness

Since the thickness of printed layer by inkjet on the whole printed area is nonhomogeneous, the best outcomes are gained with 35% and 36% of laser power. Fig.4.24. shows the treatment of the printed layer with different laser power. At 33% the laser power is too low, above 37% copper starts to peel off(ablation), from 36 to 38% the colour is metallic.

AHS: Average Step Height

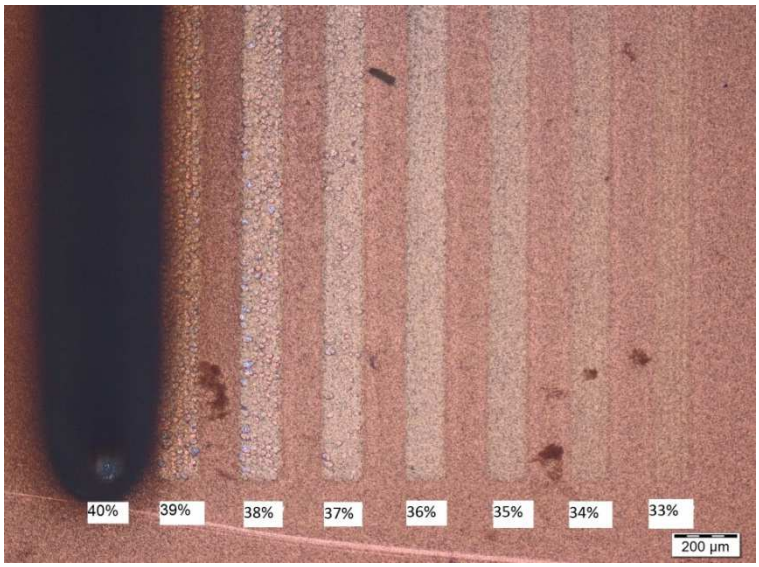

Repetition Rate	2MHz
Current(A)	40
laser power	from 33% to 40%
Galvo Scanner Speed(m/s)	0.01
jump speed	0.05
Focus (over optic table) (mm)	105
optic lens (mm)	330
Overscan	1
lateral distance	30

Fig.4.24. Illustration of the treatment of printed lines with different laser power from 33% to 40%

After finding the best laser parameters, some interdigitated electrodes for TLM (transmission line measurement) were patterned. Although the width of electrode's fingers is very thin (about 50µm), after sintering black spots like delamination of layer could already be observed at some fingertips. This is due to the non-homogeneity of the copper thickness on the GaAs, thus the effect of laser sintering with the same parameters on the printing area is not the same. An example of this phenomenon is indicated in Fig.4.25.

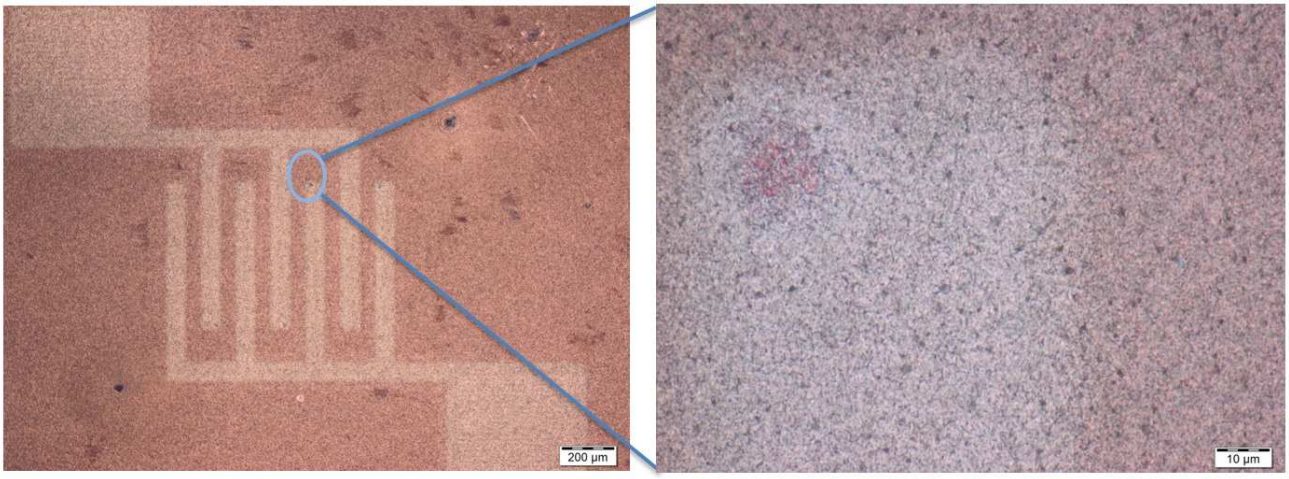

Fig.4.25. Illustration of a black spot at a fingertip of interdigitated electrodes

c-2) Variation of Ambient

With the same condition as above the effect of variation of laser power in argon ambient is explored, and is shown in Fig.4.26. It seems the results are similar to air atmosphere. The best laser power is 36%. At 34% laser power and smaller, the power is insufficient and from 38% onwards begins the ablation. In general sintering under another ambient couldn't improve the sintering and consequently the adhesion.

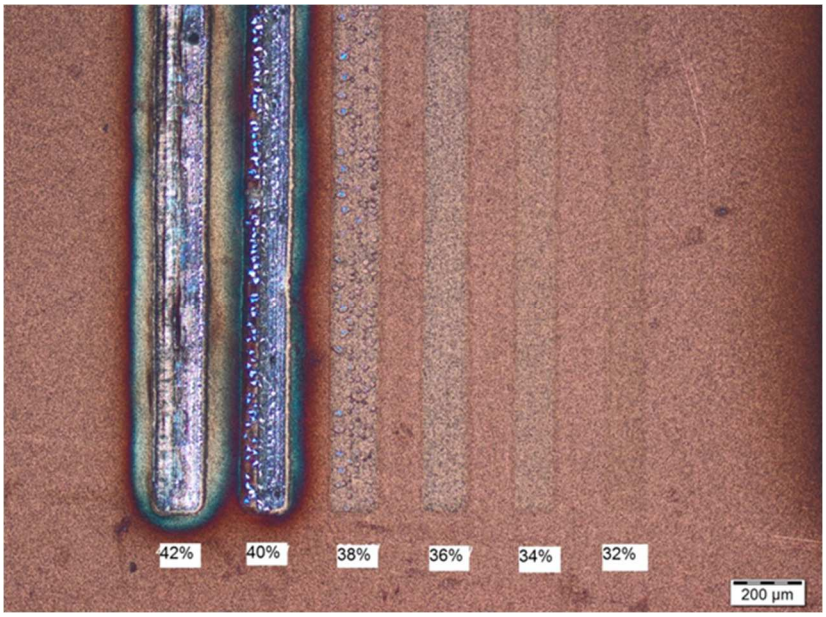

Fig.4.26. Sintering under argon ambient with different laser power.

c-3) Variation of Scan Speed:

According to widespread experiments it was identified that, if the colour of sintered copper changed to metallic colour it means, the organic cap of copper nanoparticles in ink is removed to gain neck formation of metal and finally metal grain growth. The metallic colour usually is achieved by high laser power. Therefore, to avoid the ablation, higher scan speed must be utilized. As an example, 40% laser power is about 2 times more power in comparison to 36%, hence different scan speed was performed from 0.02m/s to 0.1m/s (10 times more speed in comparison to Fig.4.24.). The results are indicated in Fig.4.27.

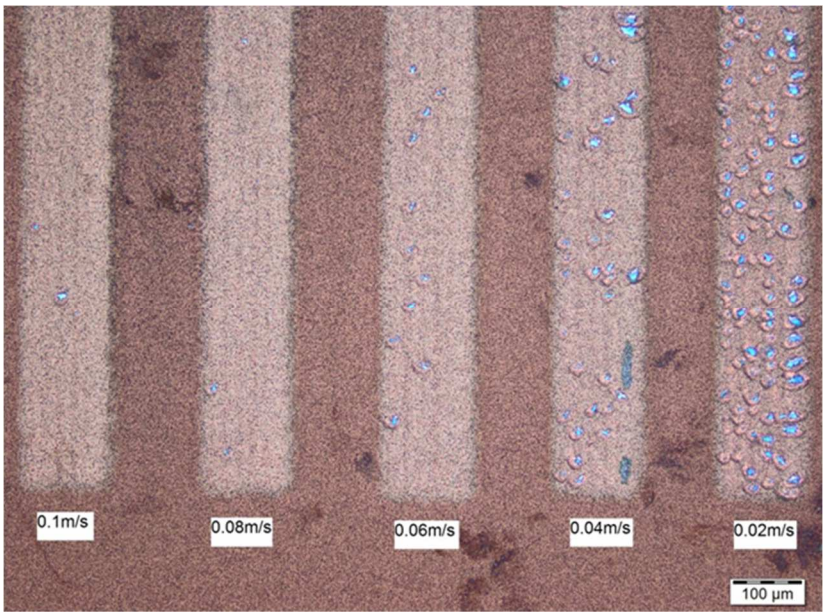

Fig.4.27. Variation of scan speed by using high laser power (40%)

As shown in Fig. 4.27. higher scan speed, or in other words shorter sintering duration (exposure time), resulted in a decrease of the probability of ablation. In comparison to Fig. the colour of sintered copper is more metallic but some ablations could be observed. Sintering of the interdigitated electrodes with using the high laser power and high scan speed is very hard, because of fast heating in a very short time, reducing heat dissipation to the substrate, especially in small areas like fingers, so that delamination or ablation occurred. (see Fig.4.28.)

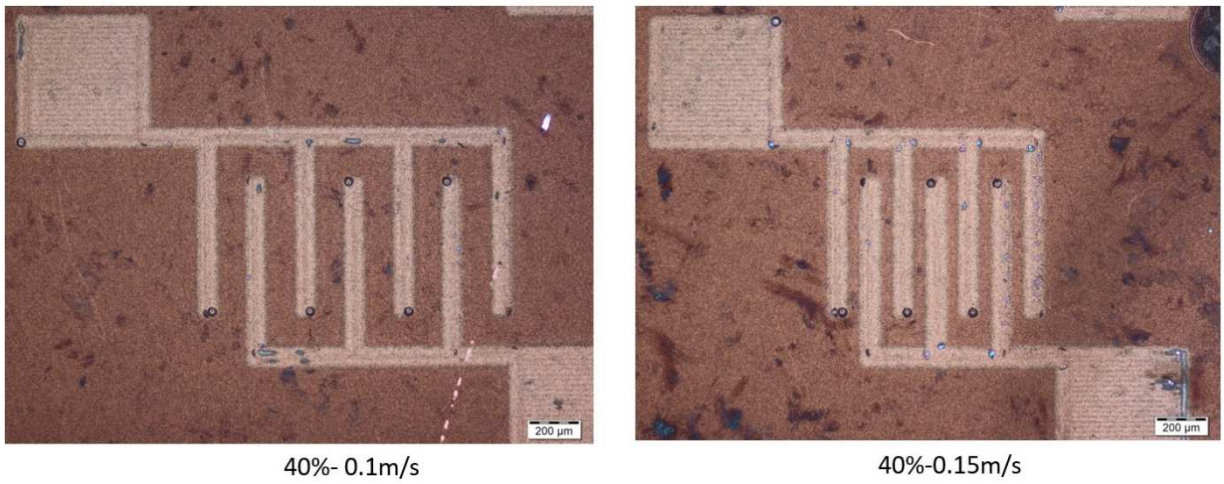

Fig.4.28. Sintering interdigitated electrodes with 40% laser power in 0.1 and 0.15 m/s scan speed

c-4) Variation of Over Scans:

The result of doing more times over scans is very similar to outcomes on the glass substrate. It signifies more over scans couldn't optimize the sintering process and adhesion of sintered copper on substrate. Fig.4.29. shows the 2,4 and 8 times over scans. There is no difference between samples and the colour of sintered copper stays constant.

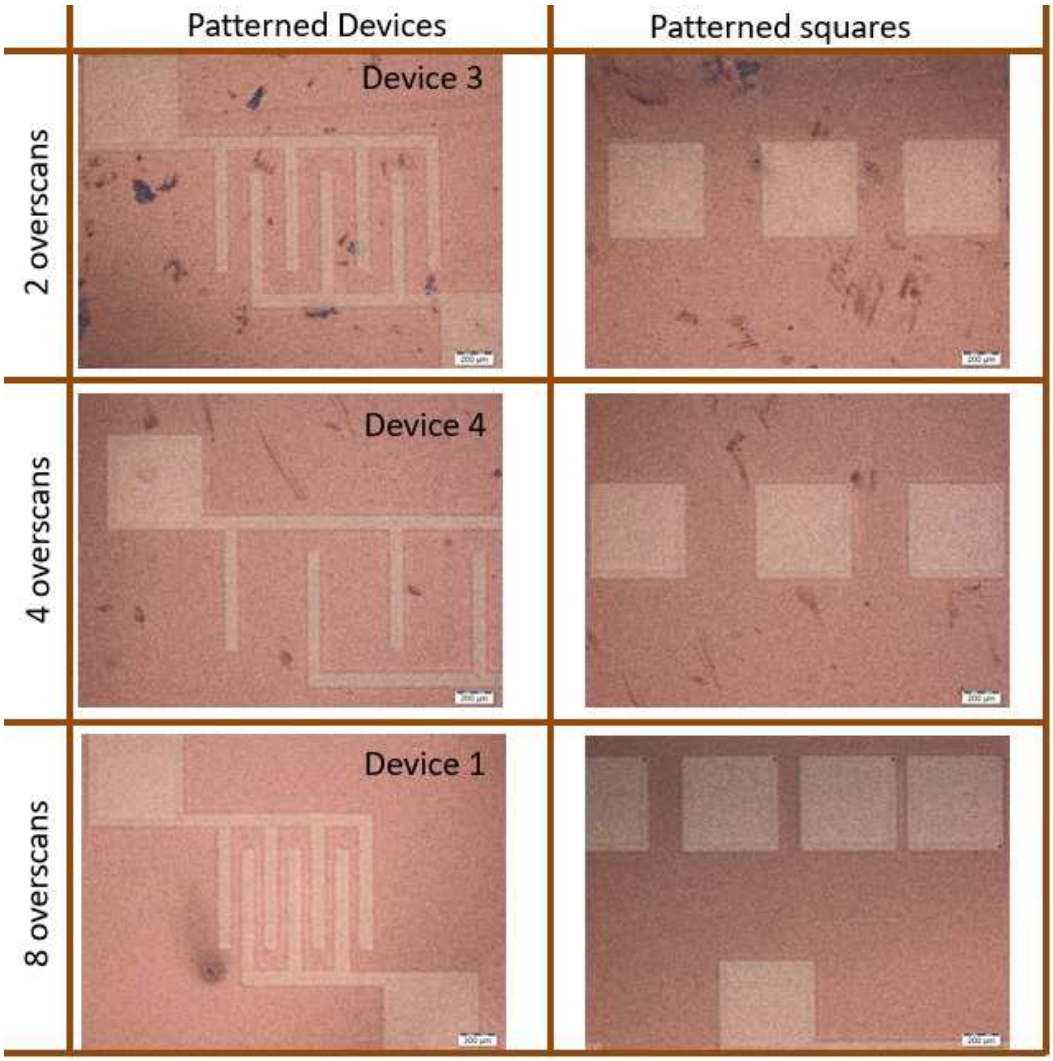

Fig.4.29. Comparison of samples with high laser power and high number of over scans with low laser power. It is clear that, the sintered copper is more similar to pure copper and is a better outcome.

The laser parameters of samples in Fig.4.30. are listed in the table. It must be noted here, that in contrast to glass substrate, by increasing the number of over scans the ablation threshold didn't change on GaAs.

Repetition Rate	50MHz
Current(A)	40
laser power	35%
Galvo Scanner Speed(m/s)	0.01
jump speed(m/s)	0.05
Focus (over optic table) (µm)	105
optic lens (mm)	330
Overscan	2,4,8
lateral distance (µm)	20

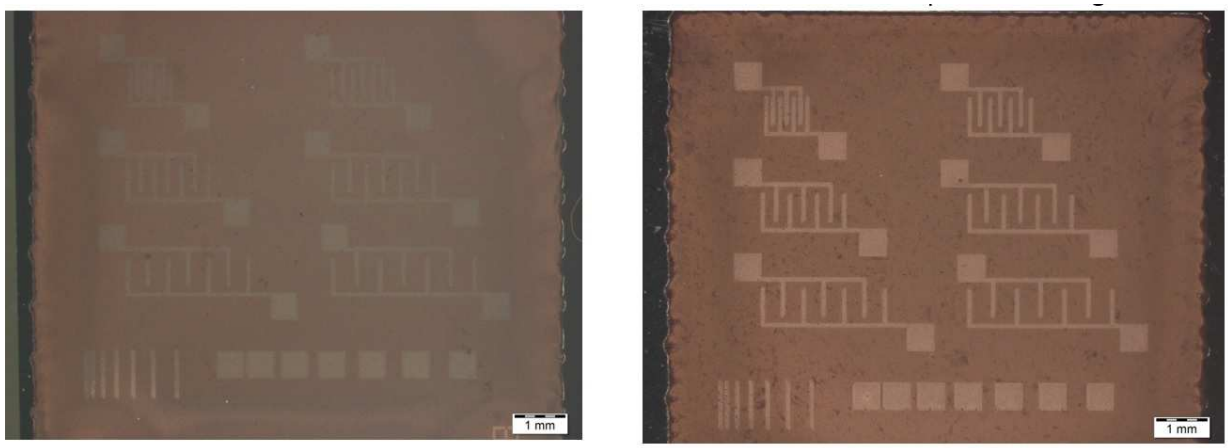

Fig.4.30. Comparing the samples with high laser power and high number of over scans

c-5) Using Hot Plate While Sintering:

In order to prevent a thermal shock during sintering, it is suggested to warm up the wafer before sintering. Hence the GaAs substrate was placed on the hot plate with 60°C for 5 min before sintering and was kept on the hot-plate while sintering. Samples were sintered with two modified laser parameters (35%laser power, 0.01m/s scan speed and 40%laser power, 0.1m/s scan speed) but it couldn't improve the results. As indicated in Fig.4.31., on the sample with high laser power very strong ablation is seen but on the sample with lower laser power there is no ablation. It shows, at the low laser power no clear difference in results between the sintering with and without hot-plate is obtained.

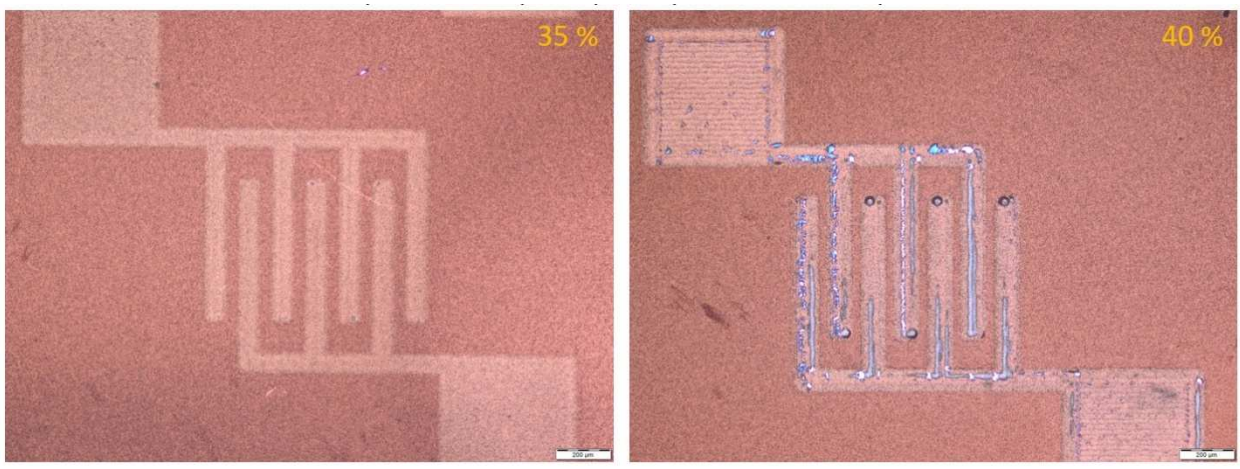

Fig.4.31. Result of warming up the sample before and during the laser sintering by hot plate

Rinsing Non Sintered Cu-NP Ink

In order to measure the contact resistance, the non-sintered copper NPs should be rinsed by an appropriate solvent (Ethanol 99%). Thus samples were placed in an ultrasonic bath for 5-15 min (The wafer was placed horizontally in the bath)

After rinsing all sintered and non-sintered copper NPs in all samples were disappeared except in the sample, which was sintered with 40% laser power. Even the post processing such as post annealing in oven under argon and vacuum couldn't modify the results. Fig.4.32. represents samples after rinsing.

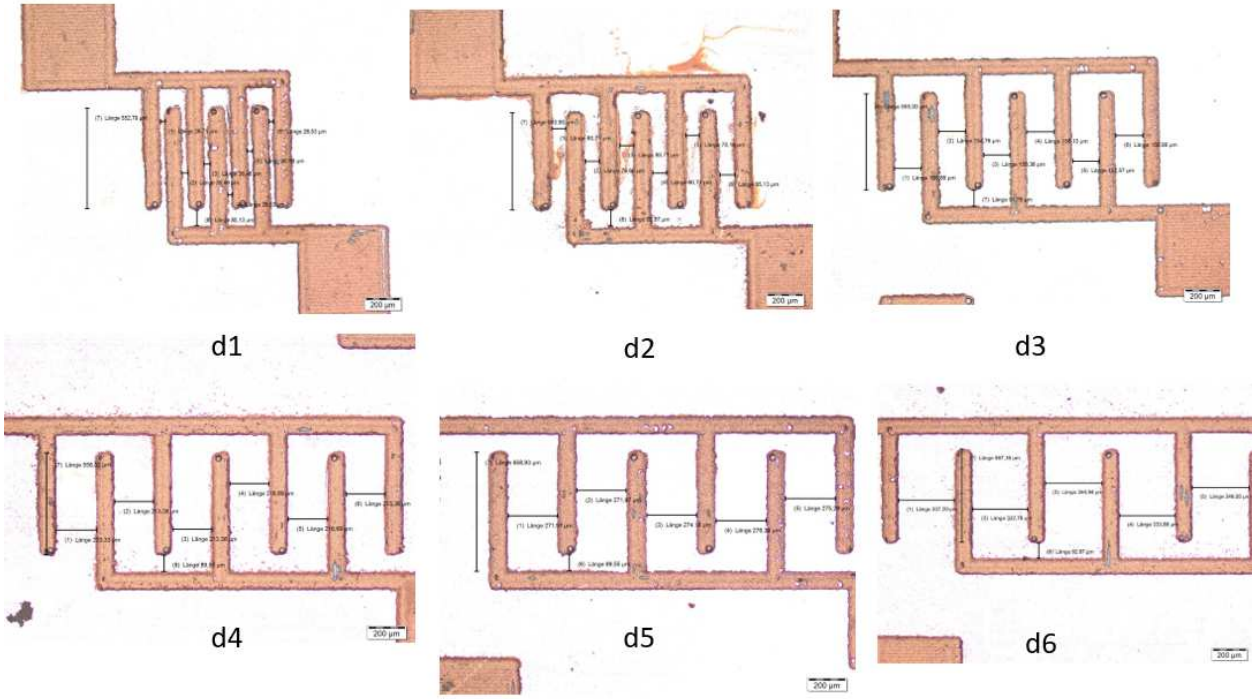

Fig.4.32. After rinsing the samples, which are sintered with 40% laser power

The summary of results after rinsing the samples is listed in the table. It shows that in all the samples, which are sintered with or without post processing, the sintered copper NPs are removed except sintered samples with high laser power (40%).

sample	number	sintering parameter	hot plate	Annealing (60min)	oversacan	result of rinsing
SK006-1 (reference)	1	35% - 0.01	✗	✗	1	✗
SK006-2	2	35% - 0.01	✗	100°C	1	✗
SK006-3	2	35% - 0.01	✗	200°C	1	✗
SK006-4	2	35% - 0.01	✗	300°C	1	✗
SK006-5	1	35% - 0.01	✗	✗	2	✗
SK006-6	1	35% - 0.01	✗	✗	4	✗
SK006-7	1	35% - 0.01	✗	✗	8	✗
SK006-8	1	35% - 0.01	✗	200°C	2	✗
SK006-9	1	35% - 0.01	✗	200°C	4	✗
SK006-10	1	35% - 0.01	✗	200°C	8	✗
SK006-11	1	40% - 0.1	✗	✗	1	✓
SK006-12	1	40% - 0.15	✗	✗	1	✓
SK006-13	1	35% - 0.01	60°C	✗	2	✗
SK006-14	1	40% - 0.2	60°C	✗	1	✗

I-V Characterization

After rinsing samples, the determination of the contact resistance between sintered copper and GaAs wafer is carried out with IV-curves measurement, for good contact the relationship between current and voltage is linear. It should be noted that to determine the contact resistance, just curves with ohmic behaviour would be considered. Sometimes there is a small deviation from ideal linear behaviour, in these cases, the measured resistance would be estimated by fitting the curves by a tangent line at the point I=0, V=0.

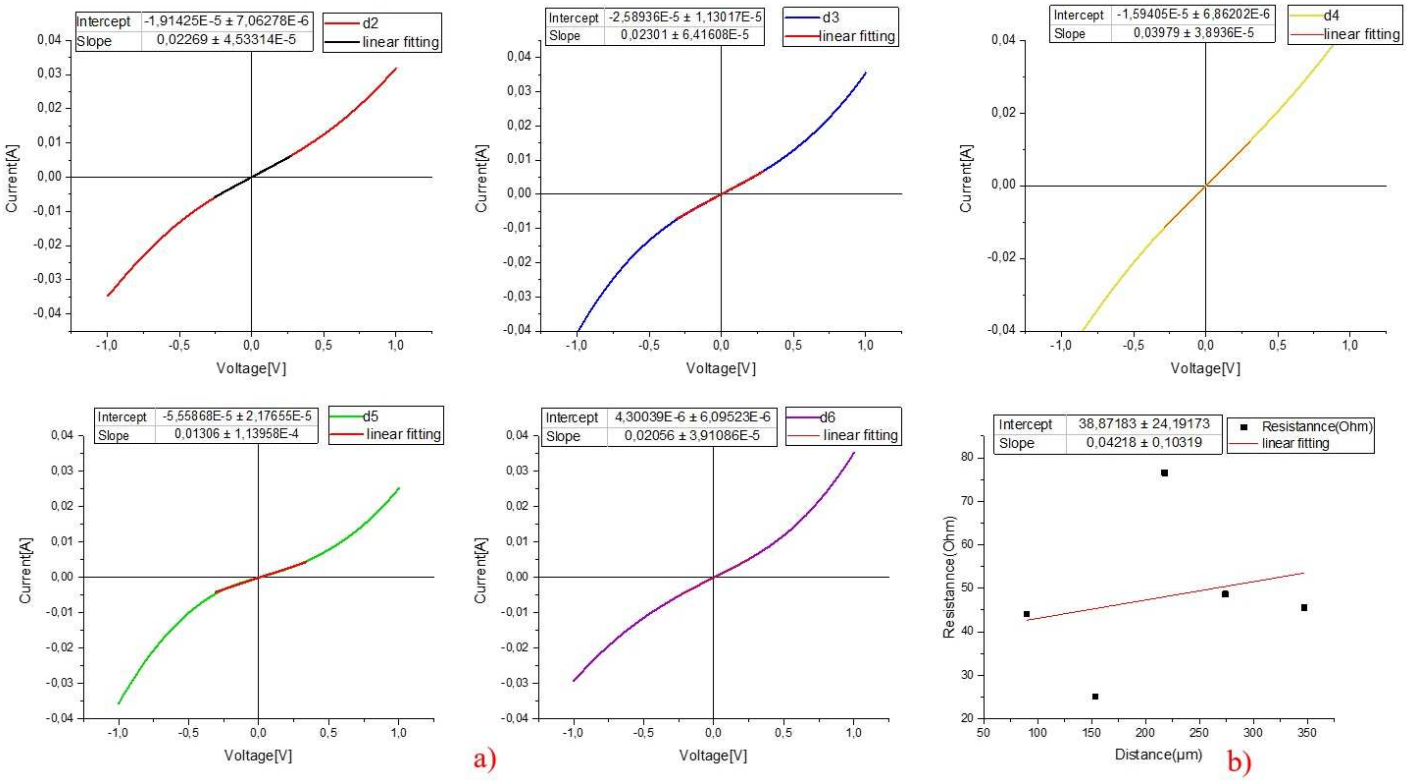

Fig.4.33. a) The IV-curves of different devices with interdigitated electrodes. b) Curve of measured resistance versus distance between fingers in devices 2 to 6.

As mentioned above this sample was sintered with 40% laser power with 0.15m/s scan speed. As Fig.4.33. indicates, there are small deviations from ohmic contact. In order to calculate the contact resistance, the measured resistance[*1] versus the distance of six devices was plotted. The distance between fingers of devices one to six was measured by optical microscope and listed in the following table.

device	d1	d2	d3	d4	d5	d6
distance(µm)	21,01	89,92	153,68	217,98	274	347,15

After defining the contact resistance, the sample was placed again in ultrasonic bath vertically to remove some particles, which remained between fingers due to placing them horizontally in the bath (see Fig.4.34.). After 15 minutes, all the sintered copper NPs were removed. This study obtained that, inkjet printing and optimum laser sintering couldn't provide good adhesion and ideal contact resistance of sintered copper on [*2]GaAs substrate.

[*1] *the slope of these IV-curves corresponded to 1/R*

[*2] *In experiments with Inkjet printing just the wafer of Freiberger was used.*

According to this plot, the R_C =14.17± 4.44 Ω. This resistance is very high for ideal contact resistance of solar cell metal electrodes.

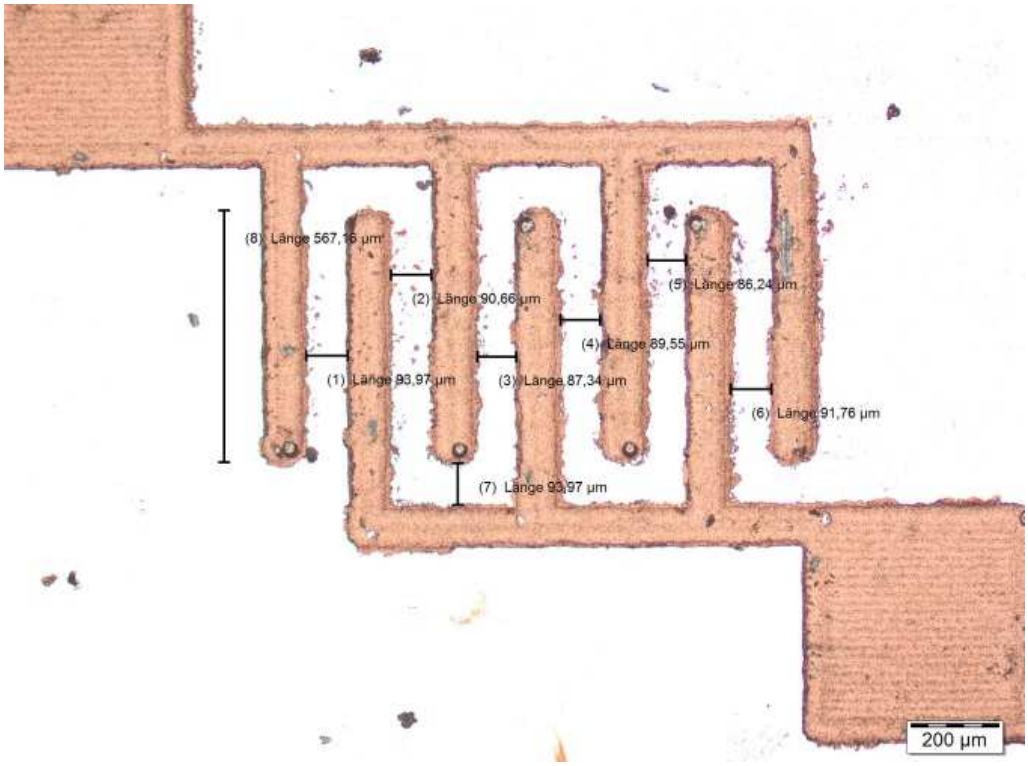

Fig.4.34. One sample of patterned interdigitated electrodes after first rinsing

Samples Printed by Spin-Coating:

Since by spin-coating the thickness of the printed layer on average is about the one third of one in inkjet printing, the laser sintering parameters should be changed, in other words the copper thin film could be sintered by lower laser power. The parameters window is listed in the table.

Repetition Rate	50MHz
Current(A)	40
laser power	33% to 34%
Galvo Scanner Speed(m/s)	0.01
jump speed(m/s)	0.05
Focus (over optic table) (µm)	best focus or zero position
optic lens (mm)	100
Overscan	1,2,3,4,5
lateral distance (µm)	10

As indicated in the table above, the optic lens of the laser is changed from 330 mm to 100 mm and this results in a smaller laser beam diameter and improves the resolution of laser patterning.

The samples were sintered by above parameters with 1,2,3,4 times over scans then rinsed and the outcomes are presented in Fig.4.35. It is clear that, there is an improvement in adhesion of sintered copper on GaAs surface and in pattern resolution. It should be noted; samples were rinsed under the same conditions as the inkjet printed samples (placing for 15 minutes in ultra-sonic bath vertically)

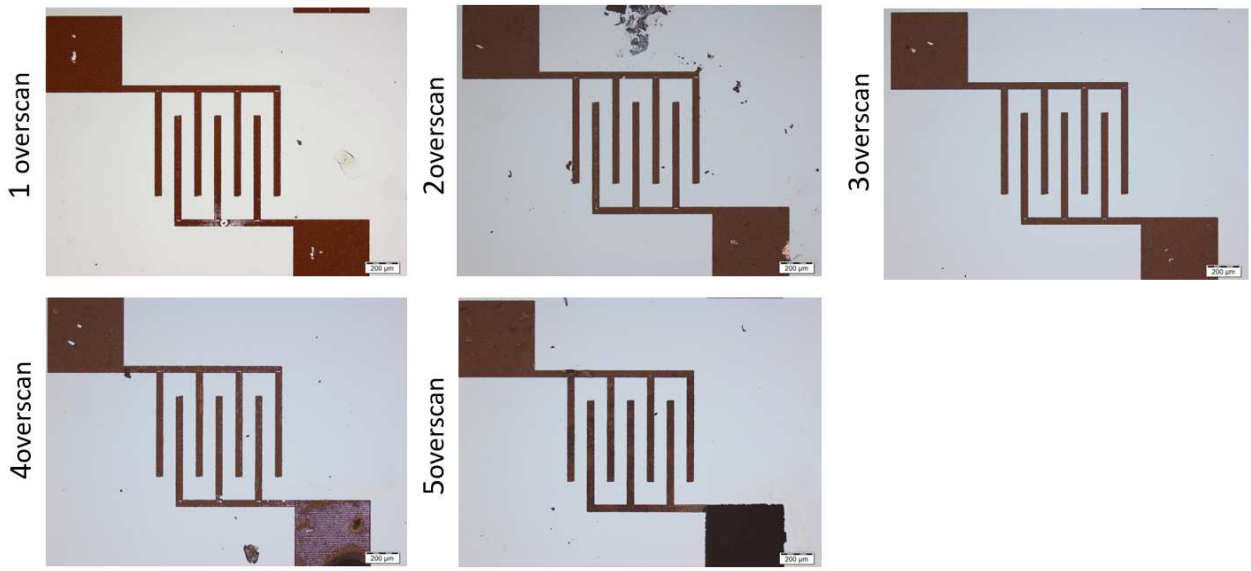

Fig.4.35. Optical images of patterned electrodes by laser with different over scan and after rinsing

As indicated in Fig.4.35. samples with 4 and 5 times over scans looked burned and ablated. The results from 1 to 3 times over scan seem very similar.

The IV characterization of samples are as below. The best result is obtained by 2 times over scans. By best focus and this wavelength of laser, we couldn't use a large range of laser power, just 33% was used for patterning because by 34% some ablations have been observed. Although it could be possible to utilize a higher scan speed (feed rate). In this case the time duration for sintering would be decreased and copper wouldn't have enough time to merge together. Therefore, the value of resistivity could be increased and fast heating increases the probability of ablation and delamination as well.

As mentioned previously each pattern includes six interdigitated electrodes(devices), six lines and seven squares with different distance between fingers but the same length. All devices in each pattern would be sintered with the same conditions (see Fig.4.36.). Therefore, it is expected, that the devices have the same electrical behavior but in some cases we encountered with different electrical characteristics.

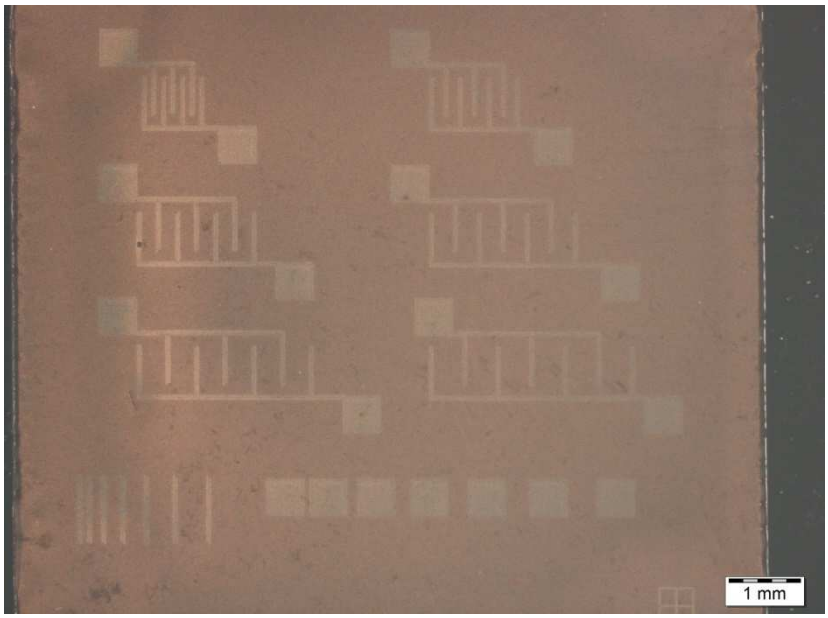

Fig.4.36. Example of sintered pattern includes six interdigitated electrodes(devices), six lines and seven squares with different distance

In the samples with one over scan only one device has almost ohmic behavior, but the current flow is very low (in range of 0.04 to 0.06 mA) and it results high slope(resistance). Fig. illustrates the IV-curves of three devices (d1, d2 and d6). d2, d3, d4 and d5 have the IV-curves of a diode. This difference might be result of weak sintering and sintering is not uniform across the sintering area.

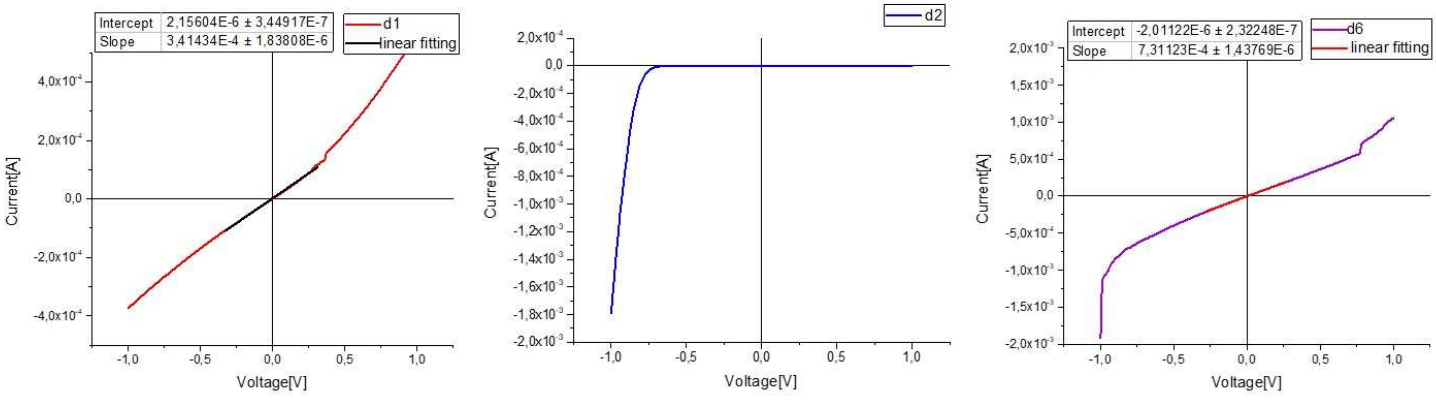

Fig.4.37. IV-curves of three devices of sample with one over scan

As is shown in Fig.4.38. by 2 times over scan d1, d4 and d5 have the I-V curve with almost ohmic behavior.

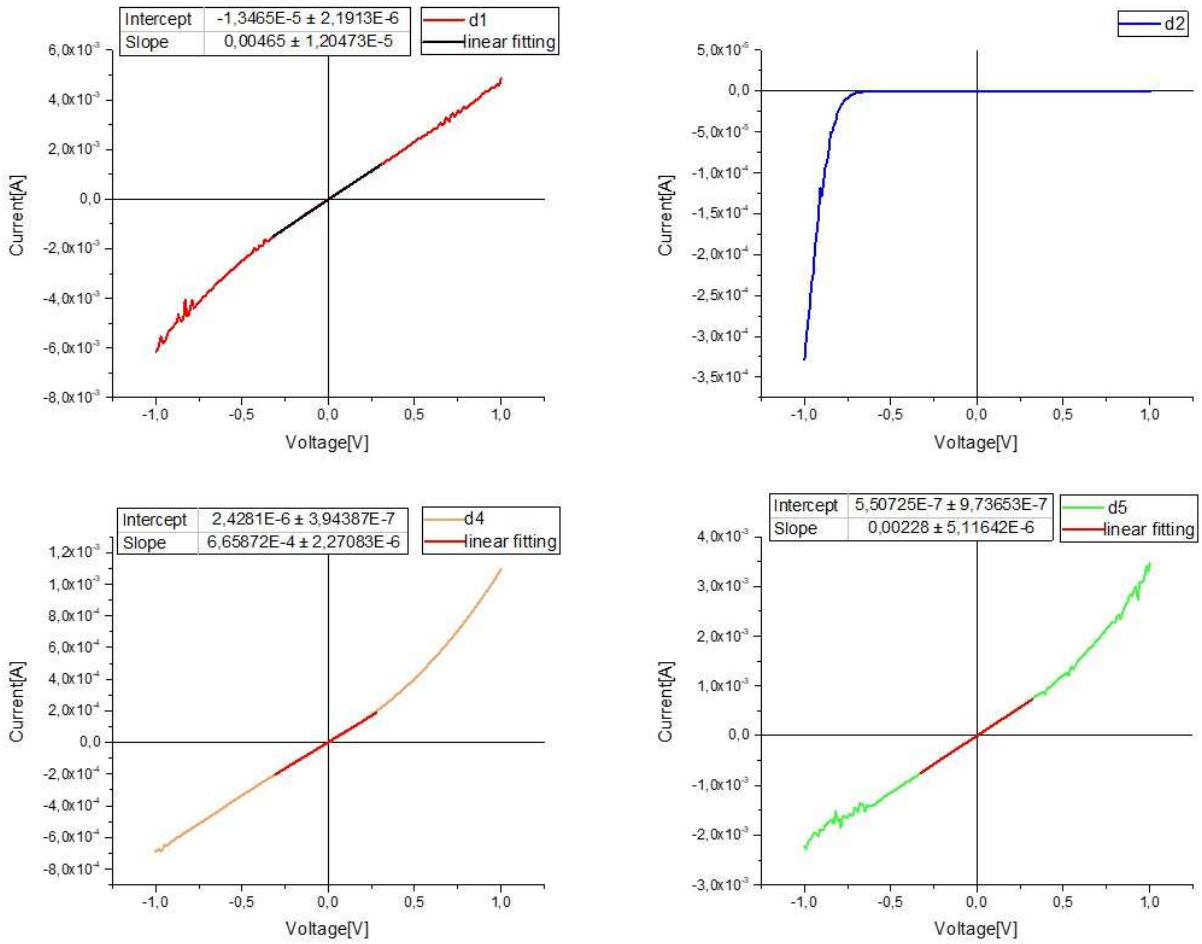

Fig.4.38. IV-curves of four devices of sample with two times over scan

The current flow in samples with two times over scans is higher than in the previous experiment. This can be explained, by enhancing the number of over scans better sintering of the copper NPs occurred and this improved the I-V characteristics on Freiberger GaAs (low doped GaAs).

To further investigation the electrical behavior of sintered copper nanoparticles, which were deposited by spin-coating, the ranges of laser power were changed by varying the position of the optical table upward or downward to provide lower (ranging around 35%) and higher (ranging from 38% to 39%) laser power respectively. In this experiment the two types of GaAs wafer were applied (Fig.4.39.) and sintered under the same condition. It should be noted, by patterning sometimes ablation occurred especially in fingers (with width of almost 40 µm). This hints at different behavior of thin film copper between slim lines and wider area at the same conditions of laser parameters.

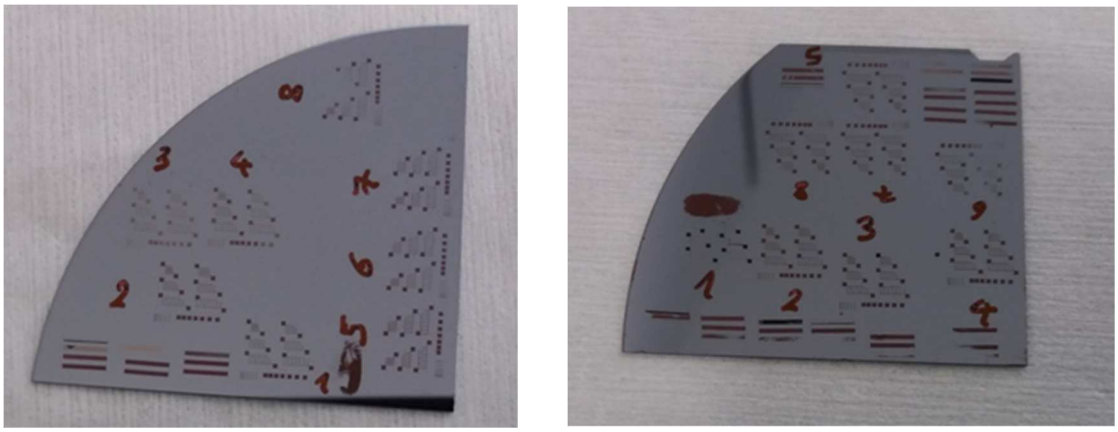

a) b)

Fig.4.39. a) Freiberger sample (low dopped), b) Azur sample (high dopped)

The summary of outcomes is listed in the table below:

Pattern	focus (µm)	laser power(%)	scan speed(m/s)	lateral distance(µm)	over scan	result (resistance of devices)(Ω)	result after annealing (resistance of devices)(Ω)
SK012-a-1	500	35%	0,05	10	1	schottky	schottky
SK012-a-2	500	35%	0,05	10	1	schottky	schottky
SK012-a-3	500	35%	0,01	10	1	schottky	schottky
SK012-a-4	500	35%	0,01	10	1	schottky	schottky
SK012-a-5	-500	39%	0,01	10	1	schottky	d1=399,72 d3=148,7 d5=184,3
SK012-a-6	-500	38%	0,01	10	1	schottky	d1=121,9 d2=168,68
SK012-a-7	-500	38%	0,01	10	2	schottky	d3=143,78 d4=206,9
SK012-a-8	-500	38%	0,01	5	1	schottky	schottky
SK012-b-1	-500	40%	0,01	10	1	no IV- curves	no IV- curves
SK012-b-2	-500	39%	0,01	10	1	d1=233,1 d3=13,49 d5=2004,4 d6=401,89	d1=158.9,7 d3=12.95 d4= 239.9 d5=407,93
SK012-b-3	-500	39%	0,01	10	2	d1=112,12	schottky
SK012-b-4	-500	39%	0,01	5	1	d1= 124,21 d5=123,6	d1=96,1
SK012-b-5	0	33%	0,01	5	1	schottky	schottky
SK012-b-6	0	32%	0,01	5	1	d3= 147,9 d5=18234,4	d3=103,64 d4=215,7
SK012-b-7	0	33%	0,01	10	1	d2= 205,65	schottky
SK012-b-8	0	33%	0,01	10	1	schottky	schottky

According to the table of results, there isn't any ohmic behavior for low doped GaAs wafer whereas for high doped GaAs wafer some ohmic curves have been seen but the slopes of the curves (resistance) are still huge, except device 3 with resistance of 13,49 Ω.

The electrical characterization and morphological images of samples with low and high doped wafers respectively are shown below:

Freiberger GaAs Wafer:

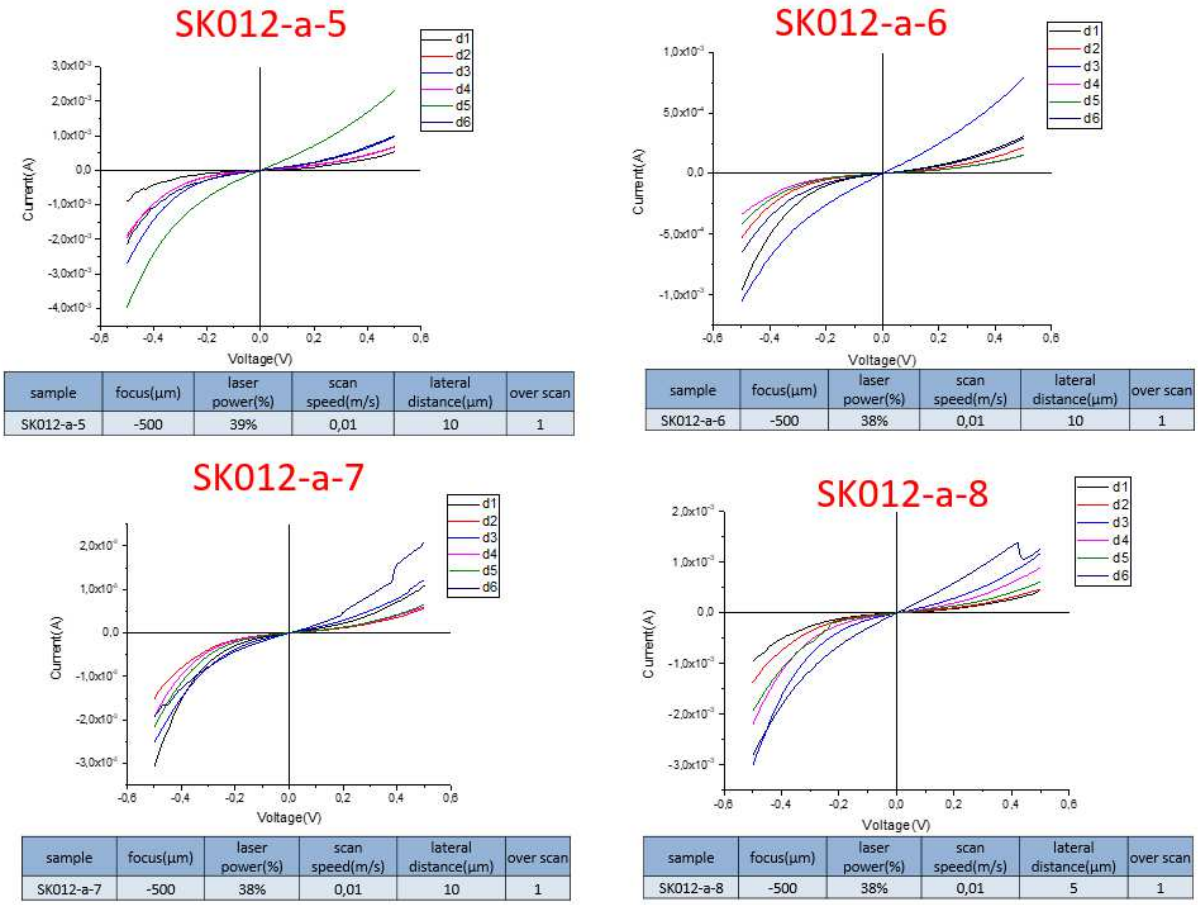

sample	focus(µm)	laser power(%)	scan speed(m/s)	lateral distance(µm)	over scan
SK012-a-5	-500	39%	0,01	10	1

sample	focus(µm)	laser power(%)	scan speed(m/s)	lateral distance(µm)	over scan
SK012-a-6	-500	38%	0,01	10	1

sample	focus(µm)	laser power(%)	scan speed(m/s)	lateral distance(µm)	over scan
SK012-a-7	-500	38%	0,01	10	1

sample	focus(µm)	laser power(%)	scan speed(m/s)	lateral distance(µm)	over scan
SK012-a-8	-500	38%	0,01	5	1

Fig.4.40. IV-curves of low doped wafer from pattern 5 till 8

As illustrated in Fig.4.40. although in these patterns were sintered with high laser power by defocusing the laser beam (500µm under the best focus), there is no ohmic contact. Since wafers with low doping concentration create high barrier junctions, the probability of ohmic behavior is decreased.

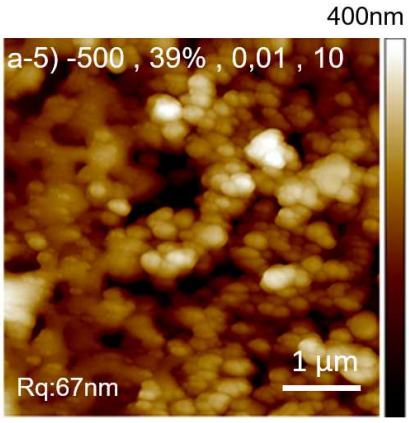

Fig.4.41. Morphological image of sintered copper on low doped GaAs wafer (Freiberger)

All devices from this pattern seem ablated and burned. In AFM image (Fig.4.41.), it is observed that, the particles are well merged (left side of AFM picture) but in some parts the film is damaged and different morphology is obtained (right side of AFM picture). This sample did not show any ohmic behavior. The merging of Cu NPs is necessary but it isn't enough to get ohmic contact and it can be a sign of burnt sample. It is also significant, that the sintering is not uniform across the laser irradiance.

Azur GaAs Wafer:

As listed in previous table (page 95), the first sample was damaged due to use high laser power (40%). The electrical characterizations of the second sample of the high doped wafer are as below:

(Sample:SK012-b-2)

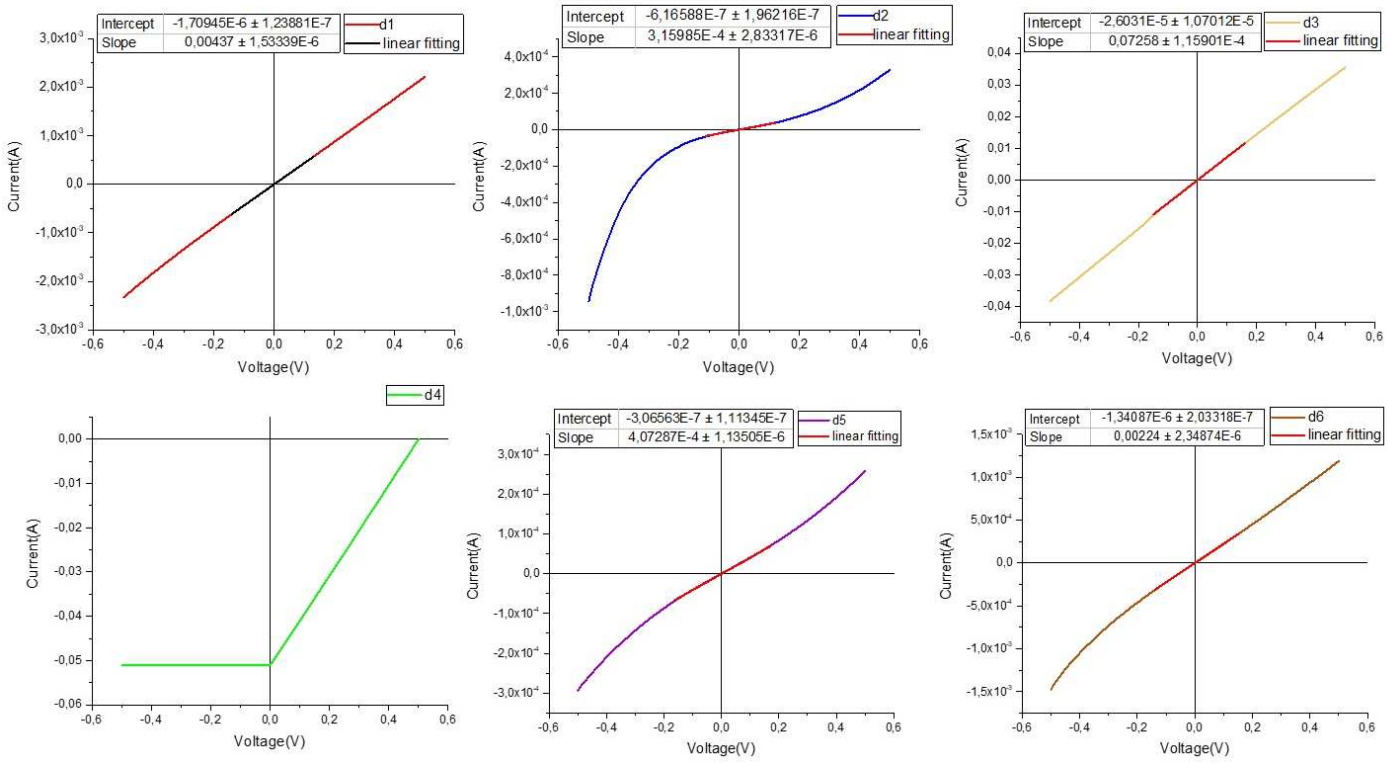

Fig.4.42. IV- curves of patterns on high doped wafer (39%laser power, 0.01m/s scan speed, 10µm lateral distance and one over scan).

As is shown in Fig. 4.42. four devices of this pattern indicate ohmic behavior, but the amount of resistance is very high and current flow is very low (in ranging from 0.3 to 3 mA).

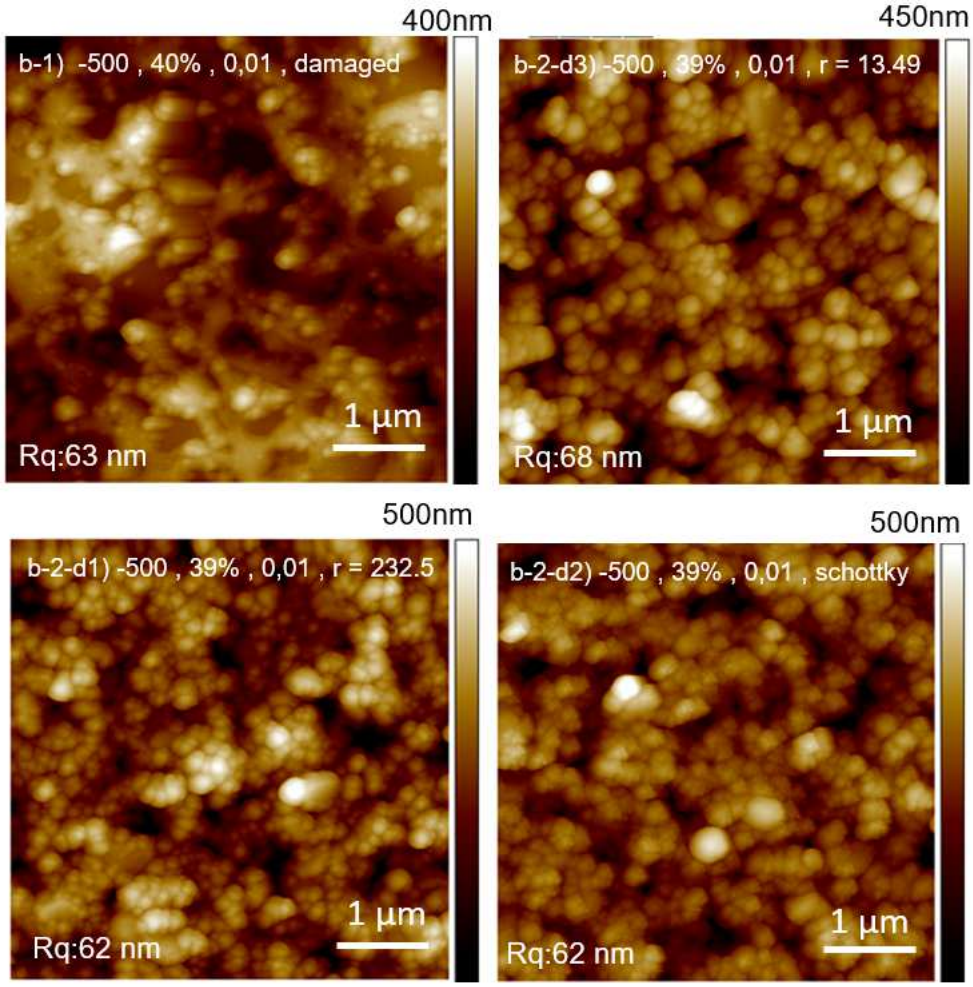

Fig.4.43. Morphological image of sintered copper on high doped GaAs wafer

With respect to AFM image, Fig.4.43. b-1) represents a burnt pattern, with very similar morphology to the burned pattern on low doped wafer and even the burned sample of inkjet samples. Fig.4.43. b-2-d3) shows the best result of the measured slope with a resistance of 13.49Ω. Although the morphology of Fig.4.43. b-2-d1) is like the best result, the measured resistance is about 17 times higher (232.5Ω). Fig.4.43. b-2-d2) indicates a pattern with schottky behavior but morphology is also like that of the best result pattern.

In general, according to the AFM images it could be concluded that:

- For samples which are burned similar morphology is obtained regardless of low or high doped GaAs wafer.
- The different electrical behaviour of devices, which are sintered with the same laser parameters is probably refer to non-uniform thickness of printed thin layer of copper NPs.

- The high resistance of sintered copper NPs refers to a thin layer of copper ink with low loading percentage of the used metal nanoparticle ink (26wt% solid content), in other words this ink has a low concentration of conductive material on the deposited area.

- Similar agglomerated particles are observed in all morphology images of the devices of one pattern but the electrical characteristics obtained are very different.

To verify more about the dissipation of copper NPs on the wafer with spin-coating and this type of Cu-ink another experiment was suggested, in which the same patterns were sintered in different places of GaAs with the same laser parameters (see Fig.4.44.). This can provide a good overview about the reproducibility of this work and give some evidence, that the dispersion of copper NPs is nonhomogeneous.

The high doped wafer was printed with the same conditions (thickness ranges from 200 to 280 nm) and patterned with the same electrodes in 6 steps with the parameters as listed in table below:

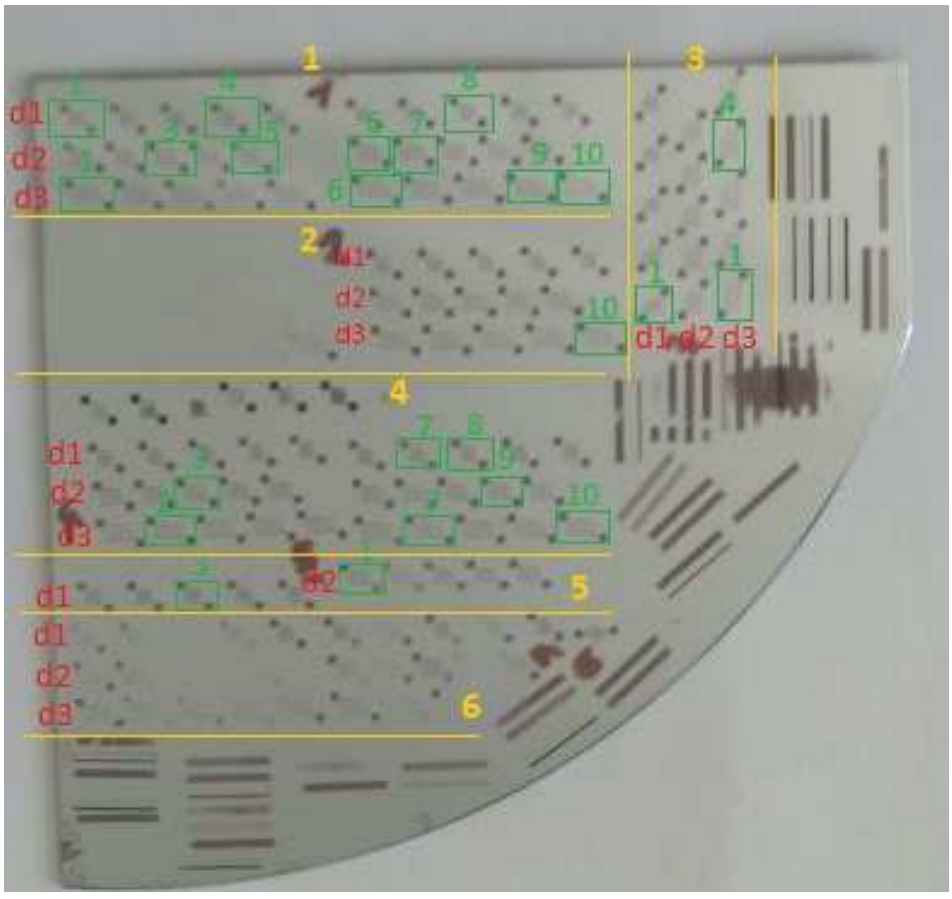

Fig.4.44. Same patterns on different places on high doped wafer in 6 steps of laser sintering

Six steps of laser sintering of same patterns on different places are listed in the table below:

steps	repetition rate (MHz)	laser power (%)	Galvo Scanner Speed(m/s)	jump speed (m/s)	lateral distance (µm)	focus (over the optic table)(µm)	optic lens(mm)	over scan	result
1	50	33	0.01	0.05	10	with best focuse	100	1	metallic color of sintered copper
2	50	35	0.05	0.05	10	+ 500	100	1	no metallic color of sintered copper
3	50	36	0.05	0.05	10	+ 500	100	1	metallic color of sintered copper
4	50	38	0.01	0.05	10	- 500	100	1	metallic color of sintered copper
5	50	33	0.01	0.05	10	with best focuse	100	1	metallic color of sintered copper(only d1 and d2)
6	50	38	0.01	0.05	10	- 500	100	2	metallic color of sintered copper, but some spots like ablation were visible

As displayed in Fig.4.44. just the devices d1, d2, and d3 were sintered. The points, which are marked with green and red colours represent an ohmic and a schottky behavior (curve) respectively.

According to Fig.4.44. it can be observed, that the laser power in step 2 was probably too low because some patterns were removed completely from the GaAs surface after rinsing and also the laser power in step 6 was too high or two times over scans effected ablation or burned some parts of each pattern.

It must be noted, since the laser irradiance isn't the same in each experiment, in this experiment at 39% laser power, the copper thin film was damaged (burned).

The summary of measured slope (resistance) and thickness after sintering are listed in the table below.

Step	electrode type	electrode No.	contact type	slope(Ω)	Thickness(nm)
1	d1	1	ohmic	3778,5	204.03
	d1	4	ohmic	4344,82	198,28
	d1	8	ohmic	1409,29	223,96
	d1	7	schottky	----	211,12
	d2	3	ohmic	13893,3	204,21
	d2	5	ohmic	6248	162,18
	d2	6	ohmic	11113,6	203,85
	d2	7	ohmic	1821,81	196,,06
	d2	8	schottky	----	221,3
	d3	1	ohmic	3132	178,87
	d3	6	ohmic	15377,3	202,65
	d3	9	ohmic	3227,8	210,74
	d3	10	ohmic	3701,6	193,92
	d3	7	schottky	----	206,73
2	d3	10	ohmic	13341,6	158,82
	d3	2	schottky	----	200,76
3	d1	1	ohmic	**265,61**	229,71
	d1	7	schottky	----	174,17
	d3	1	ohmic	3921,56	215,47
	d3	4	ohmic	**127,63**	202,26
	d3	9	schottky	----	225,79
4	d1	4	ohmic	2033,2	236,31
	d1	8	ohmic	2125,42	211,61
	d1	3	schottky	----	204,44
	d2	3	ohmic	1961,8	200,76
	d2	9	ohmic	951,9	231,8
	d2	6	schottky	----	215,38
	d3	2	ohmic	688,8	183,27
	d3	7	ohmic	1004,6	206,53
	d3	10	ohmic	4554,7	211,68
	d3	8	schottky	----	201,5
5	d1	3	ohmic	578,9	189,97
	d1	6	ohmic	2507,5	201,16
	d1	7	schottky	----	193,75

Summary of results of same patterns in different places on high doped GaAs wafer

The results demonstrate that:

- The dispersion of copper NPs on the substrate is nonhomogeneous, because the solid content of ink is only 26%, in other words the ink contains copper NPs less than 26% in various regions of the pattern and this is very low conductive material.

- The resistance of sintered copper depends on laser parameters, ink type (ink with higher metal content provides lower resistance) and also thickness of the printed copper film (for thicker film, lower resistance is expected). This shows good agreement of the results with the previously reported values of inkjet printing samples.

- By spin-coating the uniformity of thin film's thickness and adhesion of sintered copper NPs is improved but the resistance is enhanced due to the thinner deposited layer and consequently lower conductive NPs.

In order to explore the behaviour of copper and silver on low and high doped GaAs wafers, it was proposed to deposit pure copper and silver on wafers by e-beam PVD. In the next section the result of this parallel study will be discussed.

Si Substrate

On Si wafer copper NPs ink was printed by spin-coating and then sintered with pico-second laser. These experiments were performed in order to get more experience for laser sintering and spin-coating.

4.3. Investigation of Evaporated Copper and Silver on GaAs Wafer (Azur and Freiberger)

Copper and silver were deposited on both types of GaAs by EBPVD (electron-beam physical vapour deposition) techniques with rotating substrate holder. This experiment was conducted to investigate the behavior of pure copper and silver on both types of GaAs wafers. First, the copper deposited sample is described:

4.3.1 Deposited Copper:

Copper was deposited on the wafers in a vacuum chamber (1.2×10^{-7} mBar) with a rate of deposition of 3.2 – 4.8 A/s and a requested thickness of 100nm. Deposited samples on high and low doped GaAs are shown in Fig.4.45. a) and Fig.4.45. b) respectively.

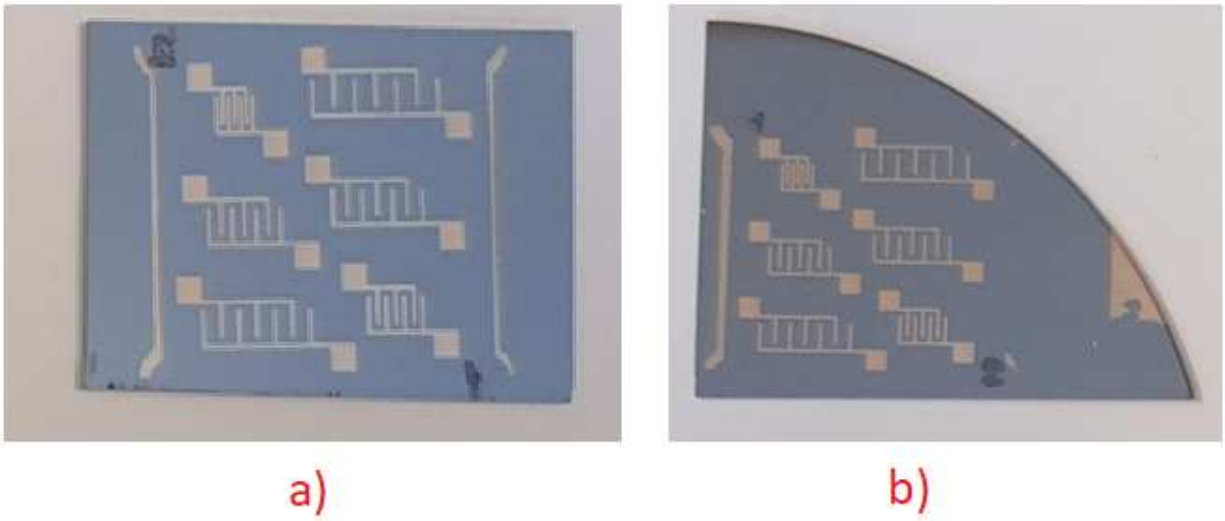

Fig.4.45. Deposited copper on a) high (Azur) and b) low (Freiberger) doped GaAs

The thickness of evaporated copper is depicted in Fig.4.46. and Fig.4.47. Although the evaporating conditions of both Wafers are the same, the ASH (average step height) of Azur is higher than Freiberger.

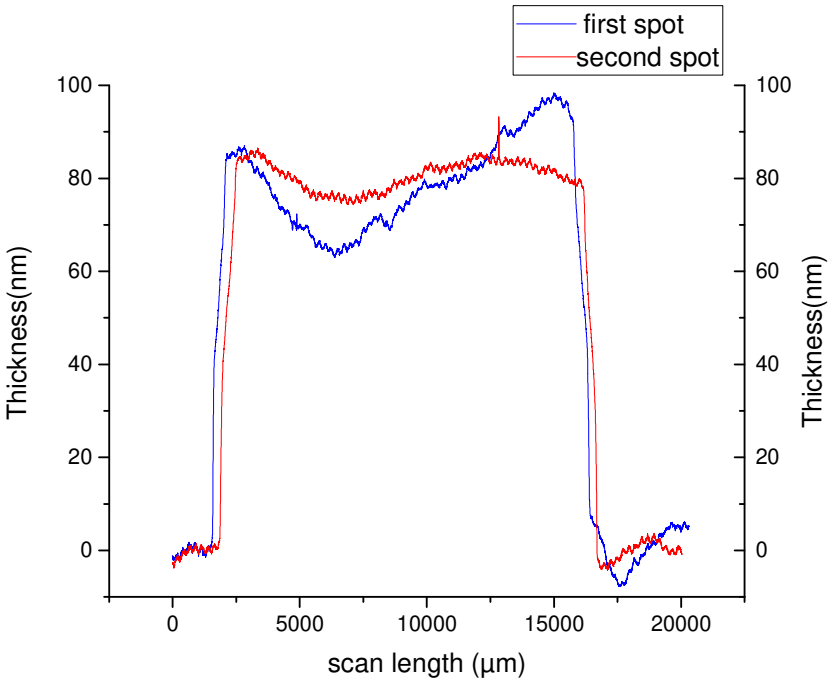

Fig.4.46. Thickness of deposited copper on the high doped GaAs wafer (Azur)

The thickness of copper on the Azur GaAs ranges from 70 to 100 nm.

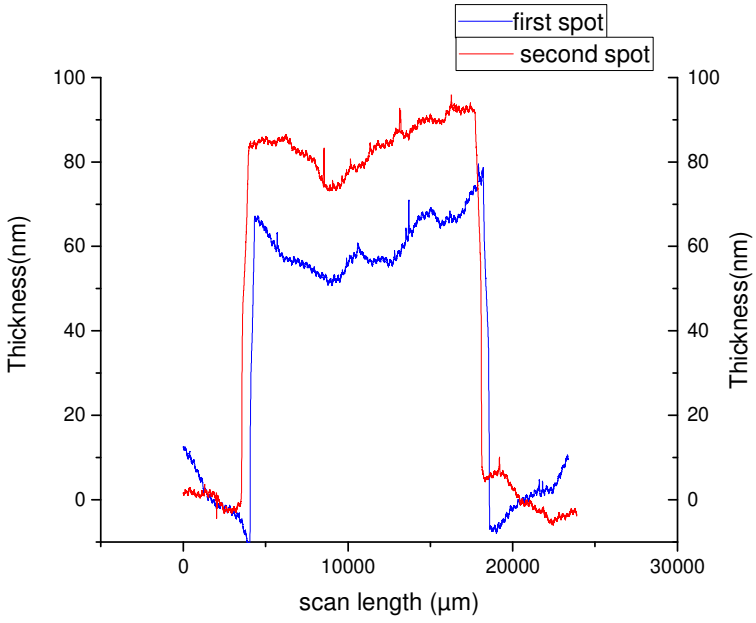

Fig.4.47. Thickness of deposited copper on the low doped GaAs wafer (Freiberge)

The thickness of copper on the Freiberger GaAs ranges from 60 to 90 nm.

The morphology of deposited copper on the Azur and Freiberger wafers is not the same. It is because of the difference in morphology of two types wafers. (see Fig.4.48.)

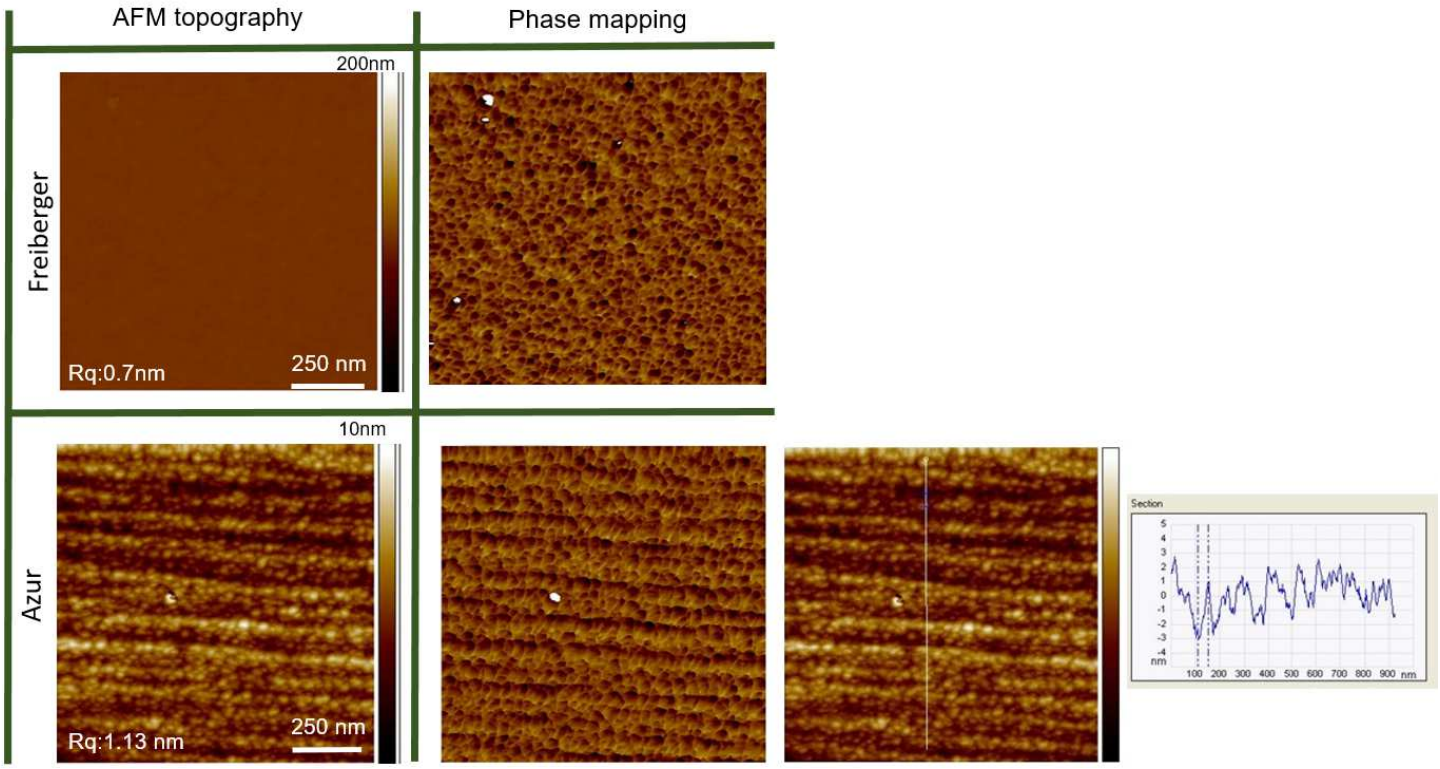

Fig.4.48. Morphological characterization of wafers after Cu deposition by EBPDV

On the Azur sample, a repetitive patterns of deposited copper are observed, due to the surface pattern of wafer before deposition (as mentioned previously on page 52). By Freiberger samples, there is a smooth deposition of copper on the substrate because of smooth surface of wafer itself. (see Fig.4.48.)

The distance between fingers in different devices and effective length of them are listed in the table below:

Divice	1	2	3	4	5	6
Distance(L)(µm)	136	305.14	480.8	654.5	850.7	1030.8
effectiv lenght(W)(µm)	1563.29	1566.1	1562.4	1563.52	1563.5	1564.7

The average of effective length was considered about 1565 µm. It must be noted, to calculate the contact resistance, only the values between +0.5 volt and -0.5 of voltage have been used.

The electrical characteristics of pure copper on the high doped GaAs wafer is very different from the sintered copper. All devices have an ohmic contact and the current flow was obtained from 0.3 to 0.4 A. (see Fig.4.49.)

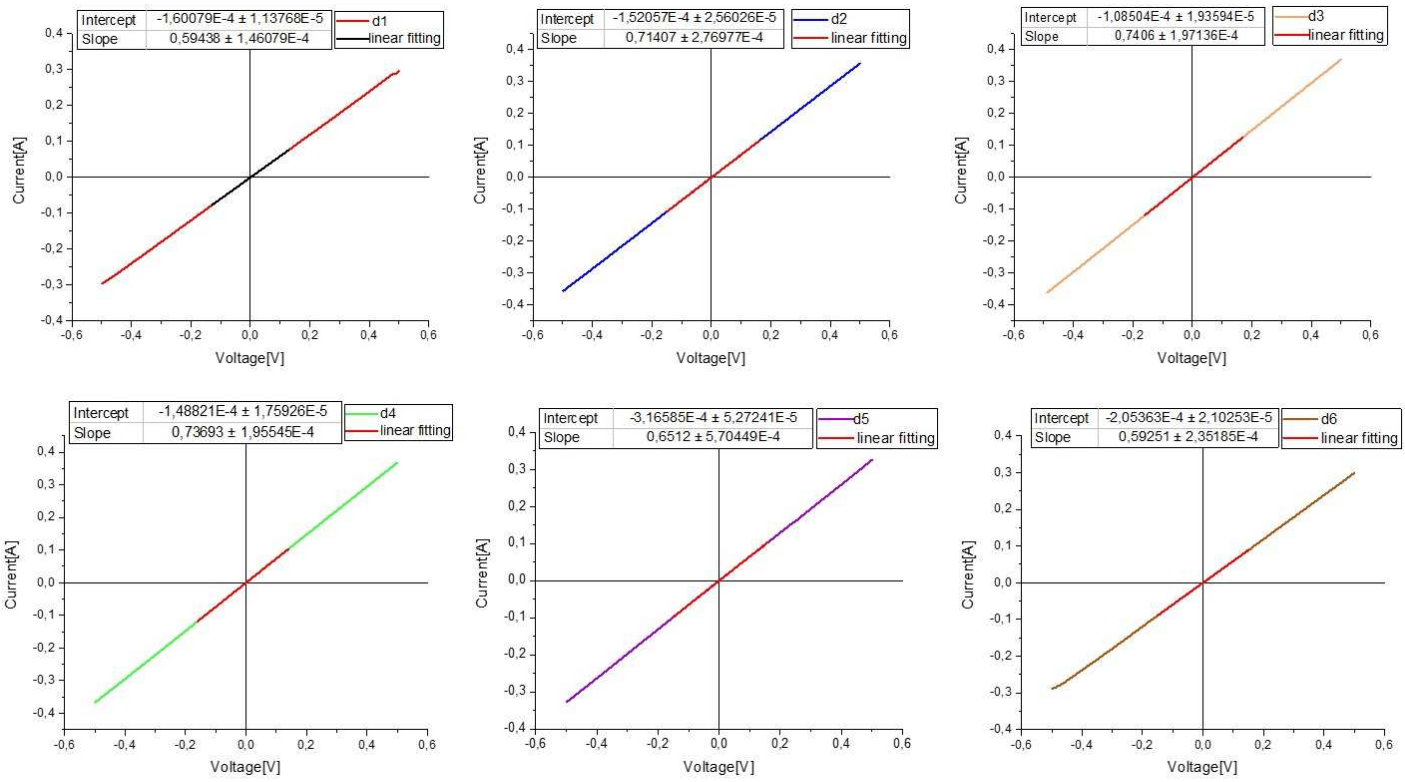

Fig.4.49. IV-curves of six devices of evaporated copper on the high doped GaAs wafer (Azur)

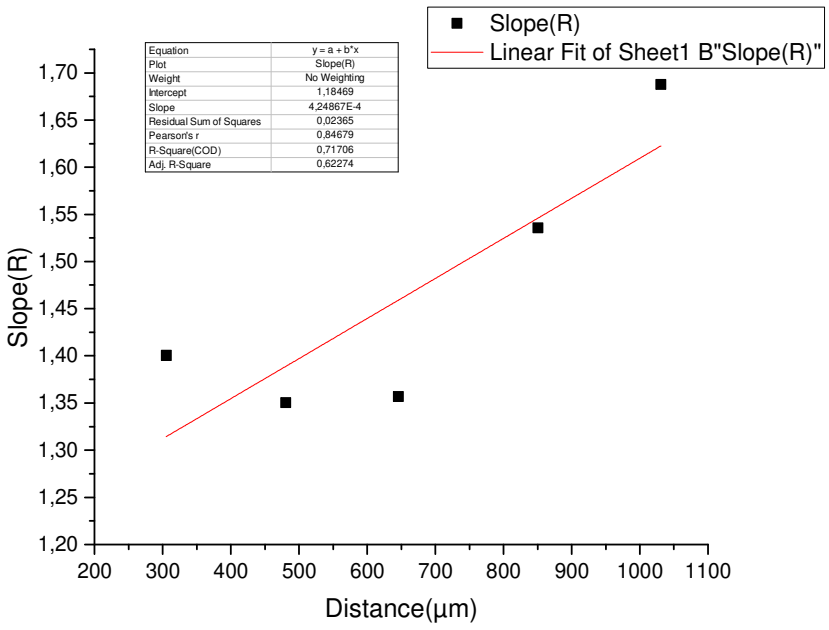

Fig.4.50. Fitting the plot of measured resistance versus distance of six devices on the high doped GaAs wafer (Azur)

After plotting the measured resistance versus different distance of six devices, the contact resistance and subsequently specific contact resistance(ρ_c) (resistivity) were calculated.

Contact resistance: 0.59 ± 0.05 Ω

Transfer length (the X-axis intercept/2): 1394 µm

specific contact resistance(ρc) (resistivity): 12×10^{-3} Ω cm^2

Fig.4.51. depicts that, the IV-curves of all devices on the low doped GaAs wafer are symmetric but have a nonlinear behavior of a double barrier in opposing directions. In other words, a rather unclean interface between metal and semiconductor.

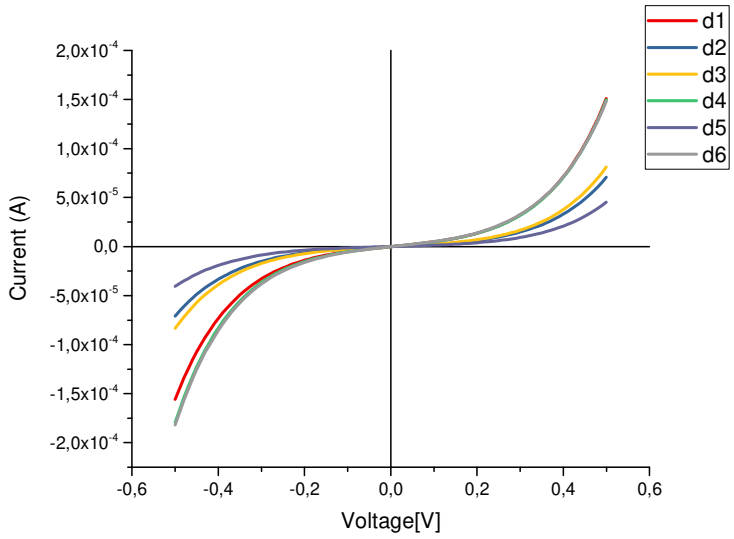

Fig.4.51. IV-curves of six devices of evaporated copper on the low doped GaAs wafer (Freiberger)

Adhesion test:

After applying sticky tape on the evaporated copper on both types of wafers and then pulling off, almost all the deposited copper thin films was removed from the substrate.

Post Processing:

In order to further study of pure copper on the two types of wafers, the post processing was carried out. The post annealing was performed in several duration times, 15 min, 1-hour and 15-hours. For 15 min and 1-hour annealing, the samples were kept on hotplate at 280 °C in glovebox under Argon atmosphere, after that the hotplate was switched off and the samples were left for 5 min to cool down in glovebox to avoid the oxidization. For 15-hours annealing the samples were placed in the oven under vacuum.

Post Annealing for15 Minutes:

Before annealing the ASH of Azur GaAs was around 80 nm and after annealing it stayed still in 80 nm therefore, it might be concluded that, the copper diffusion in GaAs was not occurred during the 15 min annealing.

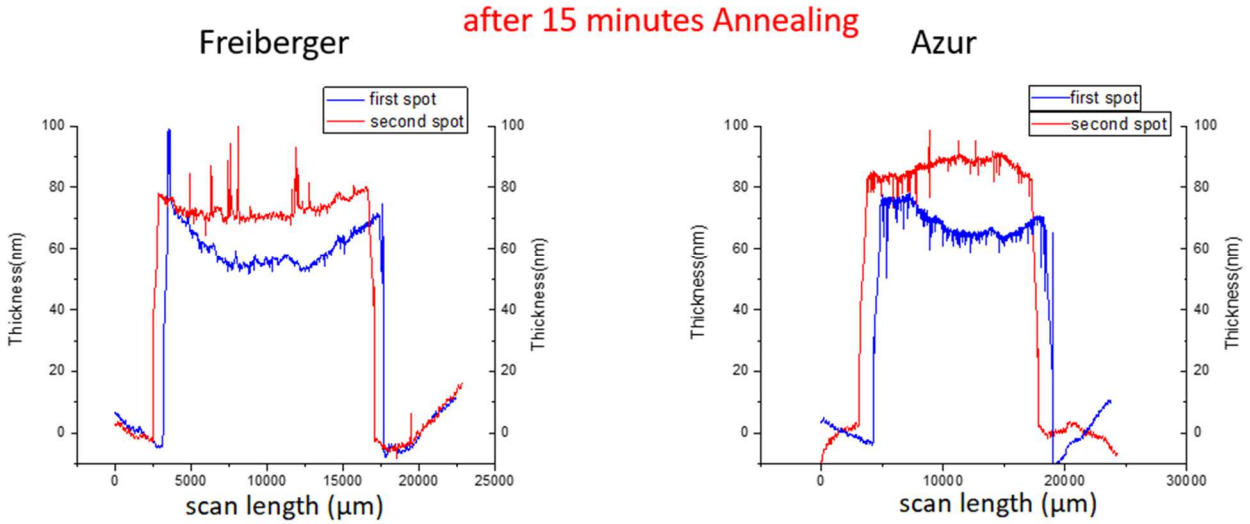

Fig.4.52. Thickness variation of evaporated copper on both types of GaAs wafer after 15 min post annealing

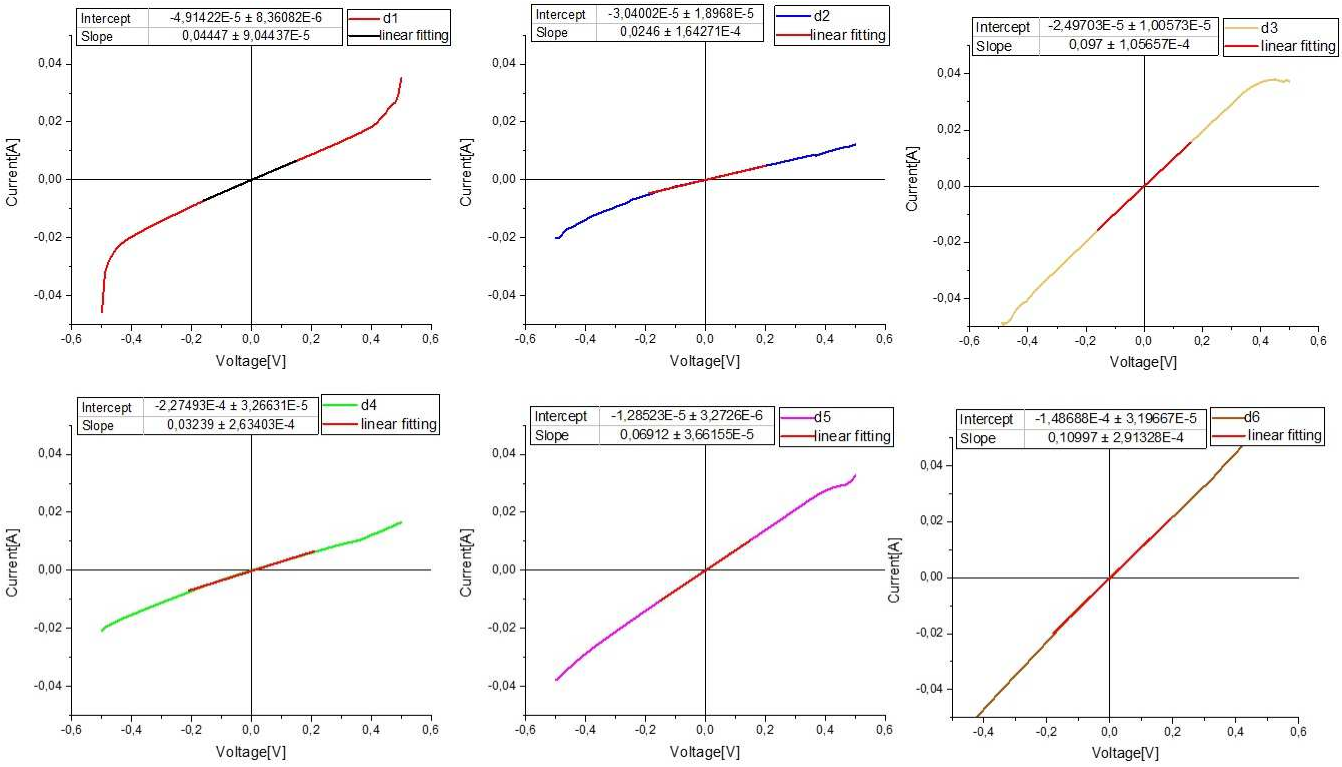

Fig.4.53. IV-curves of six devices of evaporated copper on the high doped GaAs wafer(Azur) after 15min post annealing

To evaluate the effect of post annealing, the IV-curves were measured. The outcomes are shown in Fig.4.53. Some deviation from the ohmic contact were seen and the current flow was reduced from 0.02 to 0.06 A. It is obvious that, the post annealing for 15 minutes couldn't improve the electrical characteristic of Azur wafer.

Afterward the contact resistance is extrapolated:

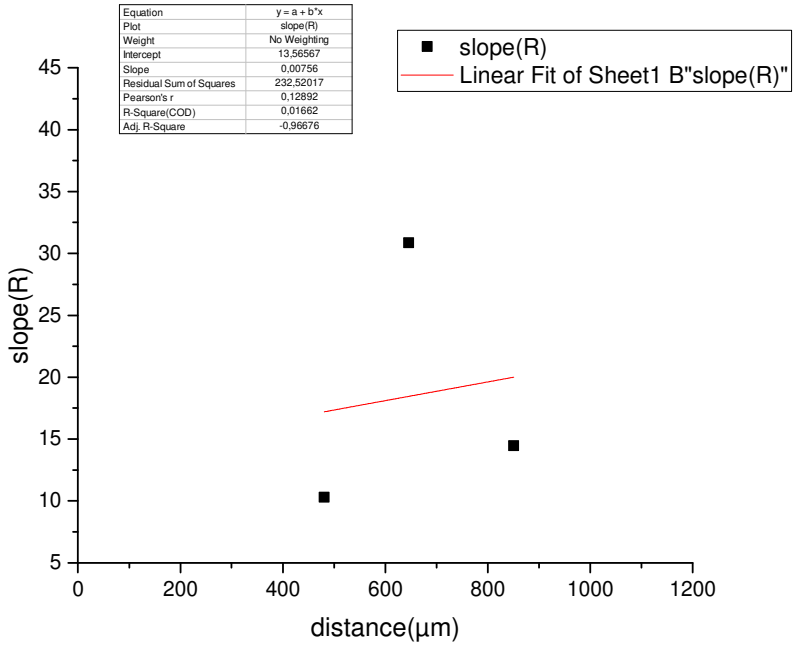

Fig.4.54. Fitting the plot of measured resistance versus distance of three devices of evaporated copper on the high doped wafer (Azur) after 15 min annealing

Contact resistance (the Y-axis intercept/2): 6.78 ± 5.44 Ω

Transfer length (the X-axis intercept/2): 896 µm

specific contact resistance(ρ_c) (resistivity): $95 \times 10^{-3}\ \Omega\ cm^2$

it is necessary to note, to calculate the contact resistance, only three points were used, on the otherwise the fitting will have a negative slope.

Before Annealing the ASH of Freiberger GaAs was in range of 60 to 90 nm and after the annealing it became in range of 50 to 75 nm. The roughness of the surface was changed and increased. It is not easy to talk about the amount of diffusion of copper in GaAs, but the sample surface was really smoother before annealing. After 15-minutes post annealing the electrical characteristic of Freiberger was changed and five of six devices have almost an ohmic contact but the current flow was still too low (in range of milliampere).

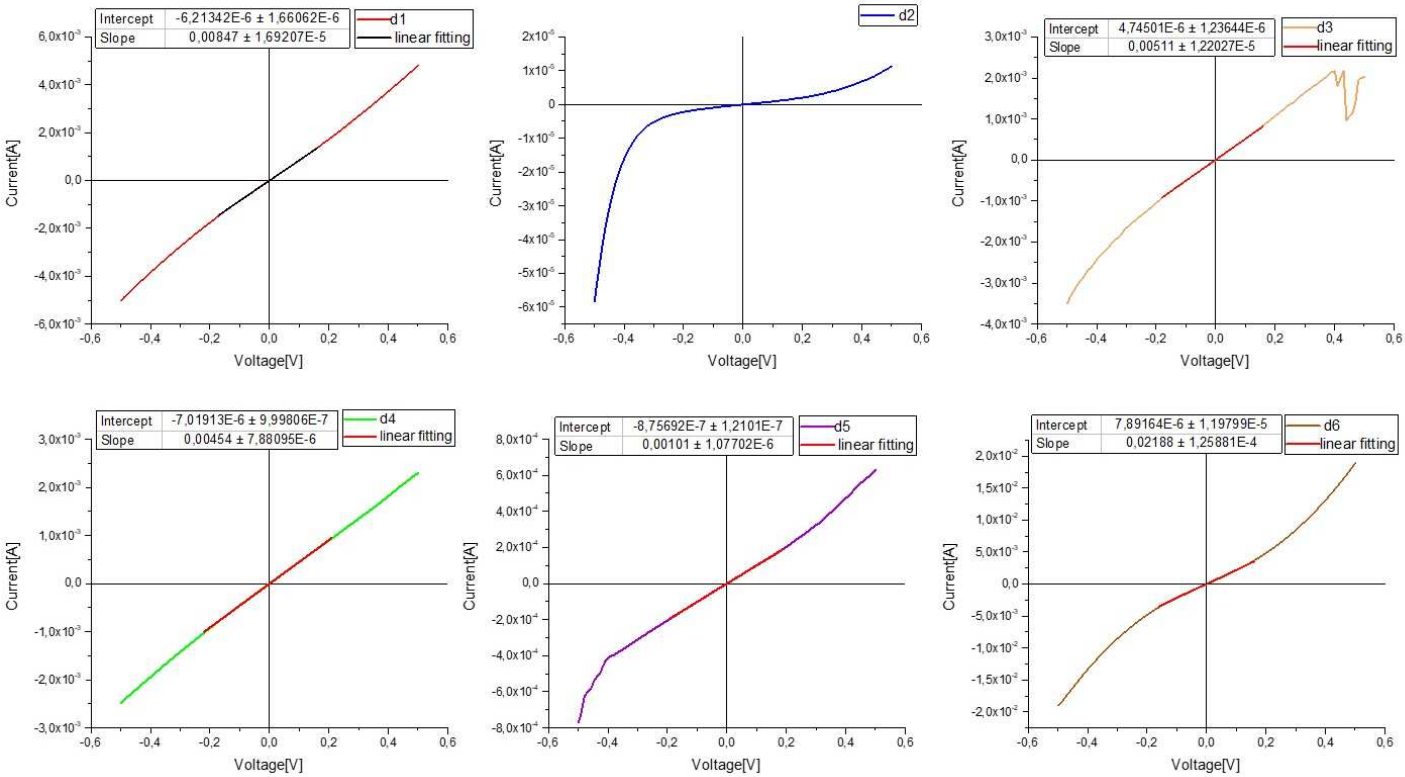

Fig.4.55 IV-curves of six devices of evaporated copper on the low doped GaAs wafer(Freiberger) after 15min post annealing

Then the contact resistance was extrapolated:

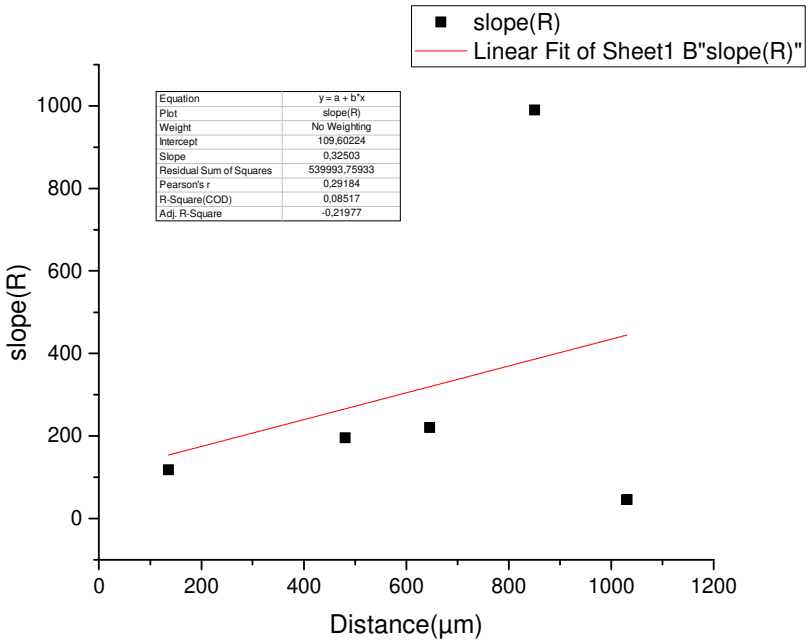

Fig.4.56. Fitting the plot of measured resistance versus distance of three devices of evaporated copper on the low doped wafer (Freiberger) after 15 min annealing

Contact resistance (the Y-axis intercept/2): 54.8 ± 215.35 Ohm

Transfer length (the X-axis intercept/2): 168.6 µm

specific contact resistance(ρ_c) (resistivity): $144 \times 10^{-3}\ \Omega\ cm^2$

the summary of results is listed in the tables below:

Azur	befor Annealing				
	ASH(nm)	Rq(nm)	contact type	R contact (Ω)	contact resistivity (Ω cm²)
	77.25	9.21	ohmic	0.59 ± 0.05	12×10^{-3}
	after 15 min Annealing				
	ASH(nm)	Rq(nm)	contact type	R contact (Ω)	contact resistivity (Ω cm²)
	75.35	10.91	ohmic	6.78 ± 5.44	95×10^{-3}

Freiberger	befor Annealing				
	ASH(nm)	Rq(nm)	contact type	R contact (Ω)	contact resistivity (Ω cm²)
	72.27	8.79	schottky	N	N
	after 15 min Annealing				
	ASH(nm)	Rq(nm)	contact type	R contact (Ω)	contact resistivity (Ω cm²)
	65.40	19.72	ohmic	54.8 ± 185.87	144×10^{-3}

this experiment was repeated for the second time and samples were annealed for 1 and 15 hours. The summary of second experiment are displayed bellow:

Azur	befor Annealing				
	ASH(nm)	Rq(nm)	contact type	RContact (Ω)	contact resistivity (Ω cm2)
	97,84	0,9	ohmic	0.58±0.14	1.07 × 10 -3
	after 1 hour Annealing				
	ASH(nm)	Rq(nm)	contact type	RContact (Ω)	contact resistivity (Ω cm2)
	90,68	2,63	almost ohmic	12.78±2.25	28.6 × 10 -3
	after 15 hours Annealing				
	ASH(nm)	Rq(nm)	contact type	RContact (Ω)	contact resistivity (Ω cm2)
	92,81	3,61	almost ohmic	N	N

Freiberger					
	befor Annealing				
	ASH(nm)	Rq(nm)	contact type	RContact (Ω)	contact resistivity (Ω cm2)
	76,51	3,59	schottky	N	N
	after 1 hour Annealing				
	ASH(nm)	Rq(nm)	contact type	RContact (Ω)	contact resistivity (Ω cm2)
	132,4	70,76	ohmic	10.52±2.61	9.8 × 10 -3
	after 15 hours Annealing				
	ASH(nm)	Rq(nm)	contact type	RContact (Ω)	contact resistivity (Ω cm2)
	159,15	46,57	ohmic	18.9±10.67	47.4 × 10 -3

From the compiled outcomes of all samples before and after post annealing, it is evident that:

- The contact resistance between pure copper and the high doped GaAs wafer(Azur) before annealing is much lower in comparison to those after the post annealing.
- Before annealing, the samples of the low doped wafer didn't have any ohmic behavior, it might be due to higher junction barrier of metal semiconductor contact. Post annealing could be optimized results. The samples with 1-hour post annealing have the lowest contact resistance, however it is still much higher than intended contact resistance (smaller than 1Ω).
- By increasing the duration time of post annealing to 15 hours enhanced the contact resistance and subsequently resistivity in both types of GaAs wafers.

Fig.4.57. shows the thickness of second experiment of before and after annealing. In samples of the low doped GaAs wafer, the reaction of copper thin film with wafer was very intense, it might be hints at more diffusion of copper in this type of GaAs crystal.

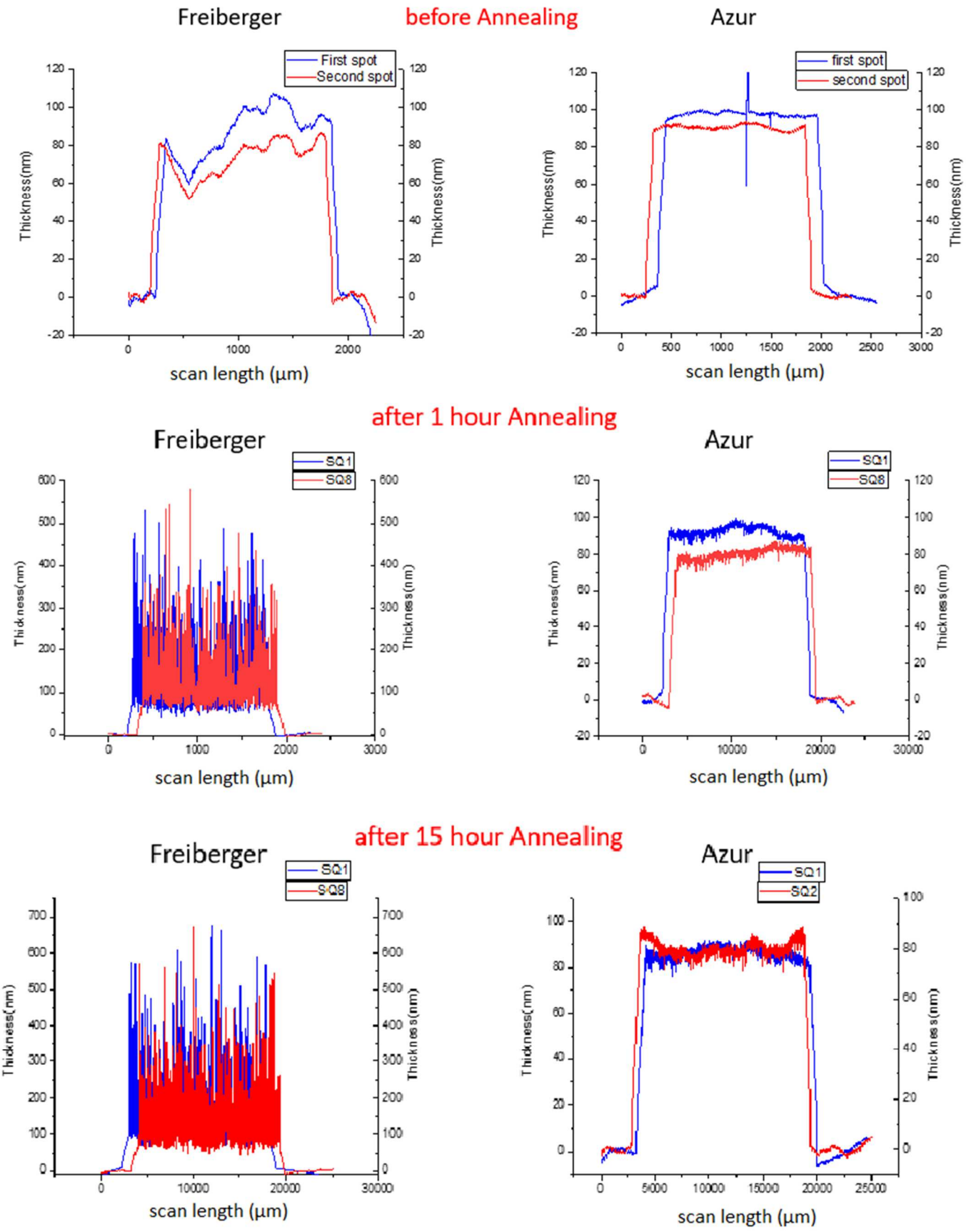

Fig.4.57. Variation of thickness of copper thin film before and after post annealing for 1 and 15 hours

To study the effect of post annealing on thin film structure, the morphology images and phase mapping were utilized. The variation of thickness was measured too to compare and obtain more accurate analysis of results.

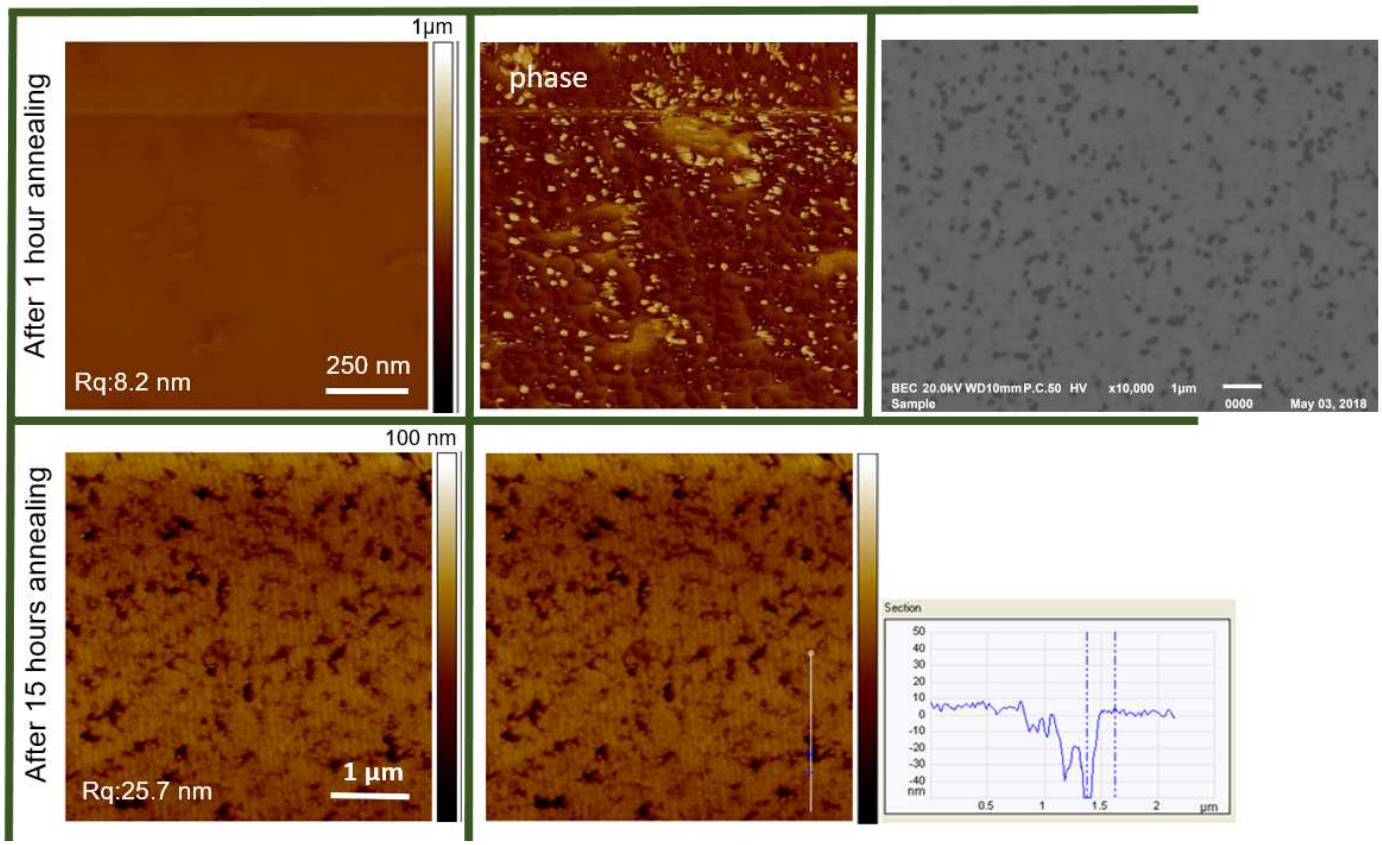

Fig.4.58. Morphological characterization of deposited copper on the high doped GaAs wafer (Azur).

The sample of the high doped GaAs wafer (Azur) have a smoother surface after annealing in comparison to Freiberger wafer.

After 15 hours annealing was formed some cracks on the surface. From the phase image it could be concluded that, there is an extra phase in the cracked part.

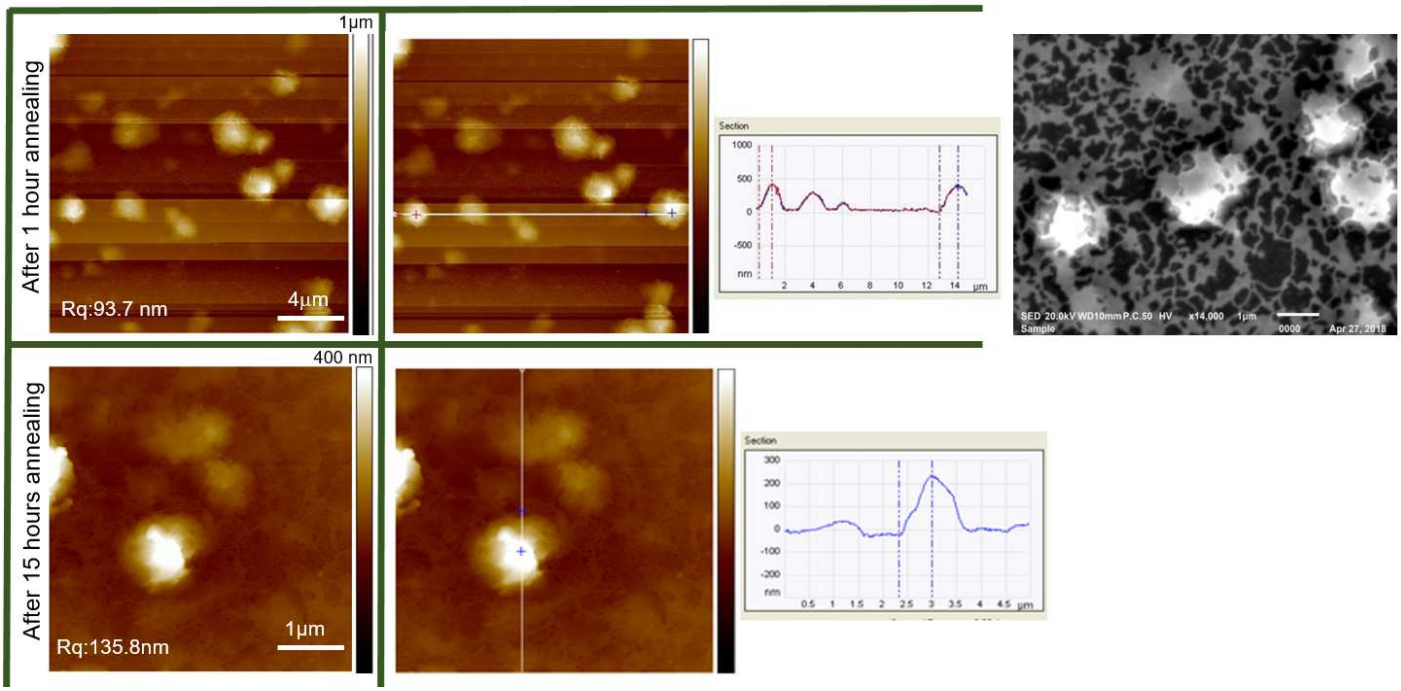

Fig.4.59. Morphological characterization of deposited copper on low doped GaAs wafer (Freiberger).

After annealing the samples of the low doped GaAs wafer (Freibeger) was seen some heterogeneous distribution of big Copper particles on the surface (like islands of copper on substrate), due to agglomeration of thin films during the annealing process. Therefore, adjusting the time and temperature of annealing is important to reduce this phenomenon. The height of these islands could be till 400 nm high. These results are supported by the results of profilometer (thickness of islands). After 15-hours annealing, the bigger particles (islands) were observed so that, some of these have a width of around 1-2 micron.

4.3.2 Deposited Silver:

The silver was deposited on both types of GaAs wafers under the same condition as the copper. Fig.4.60. a) and Fig.4.60. b) shows the evaporated silver on the high and low doped GaAs wafer respectively.

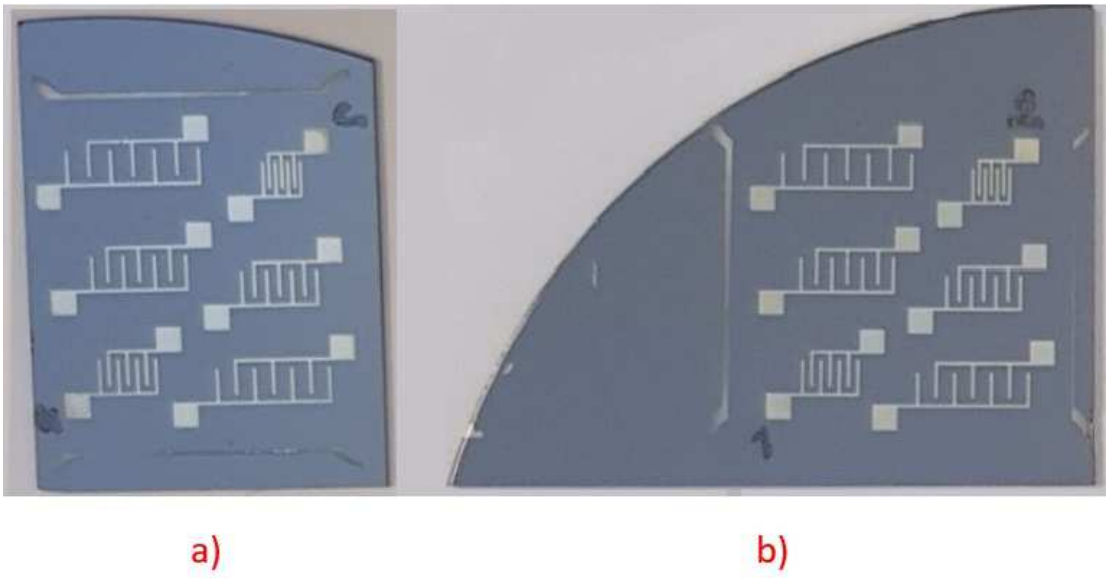

Fig.4.60. Deposited silver on a) the high (Azur) and b) low (Freiberger) doped GaAs

The thickness of evaporated silver is depicted in Fig.4.61. and Fig.4.62.

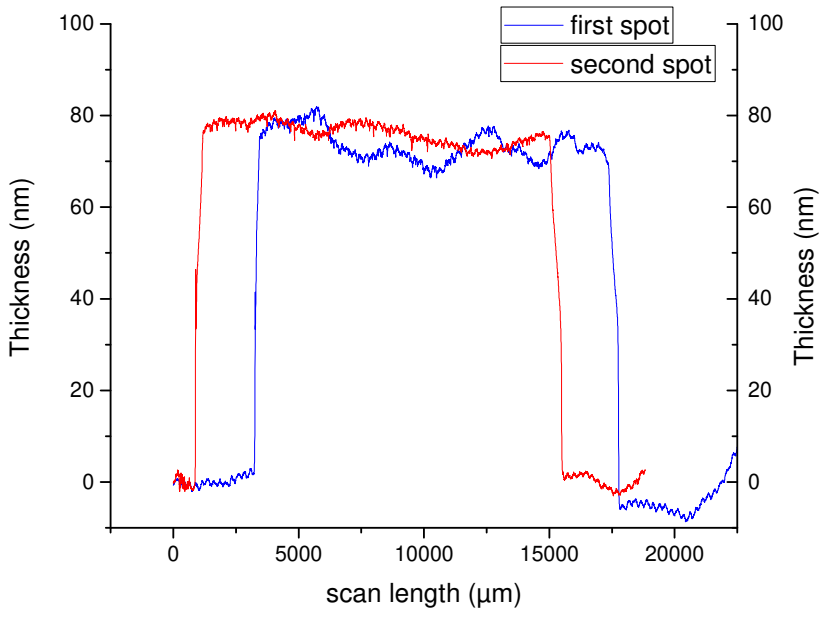

Fig.4.61. Thickness of deposited silver on the high doped GaAs wafer (Azur)

Thickness of Silver on Azur GaAs ranges from 70 to 80 nm.

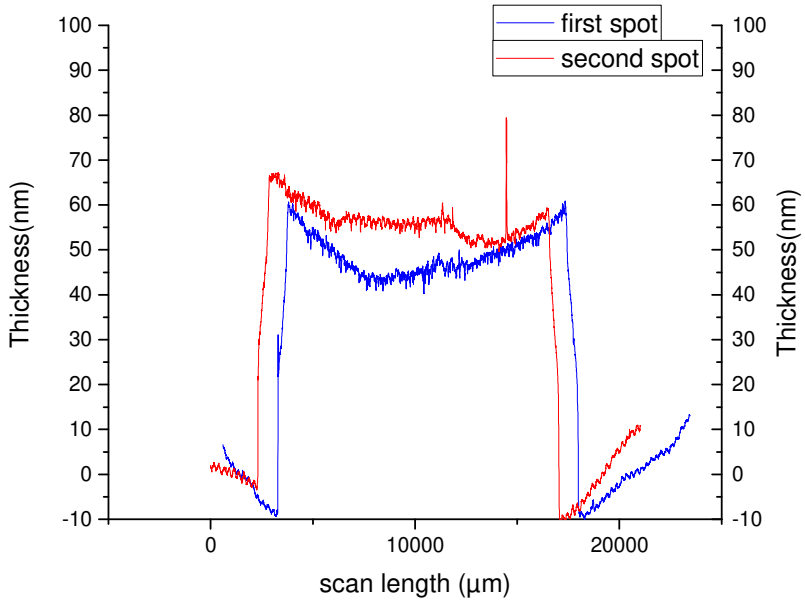

Fig.4.62. Thickness of deposited silver on the low doped GaAs wafer (Freiberger)

Thickness of Silver thin film on Freiberger GaAs ranges from 50 to 65 nm.

Although the evaporating conditions of both Wafers were the same but the ASH (average step height) of Azur is higher than Freiberger similar to copper deposited samples.

The distance between fingers in different devices and effective length of fingers are listed in the table below:

Divice	1	2	3	4	5	6
Distance(L)(µm)	163.6	316.2	493.15	663.6	855.72	1030.4
effectiv lenght(W)(µm)	1545.6	1546.5	1546.1	1551	1539.7	1547.6

The average of effective length was considered 1546 µm. It must be noted, to calculate the contact resistance, only the values between +0.5 volt and -0.5 of voltage have been used.

Fig.4.63. demonstrates that, all devices have nearly ohmic behavior except d5. The devices d1 and d2 have a comparable current to one in copper samples (in range of deciampere). It is unclear why the flow current in the d3 and d4 devices has dropped to one-twentieth. Since the slope of plot with six points or even five points would be negative hence, four points were considered for calculating the contact resistance.

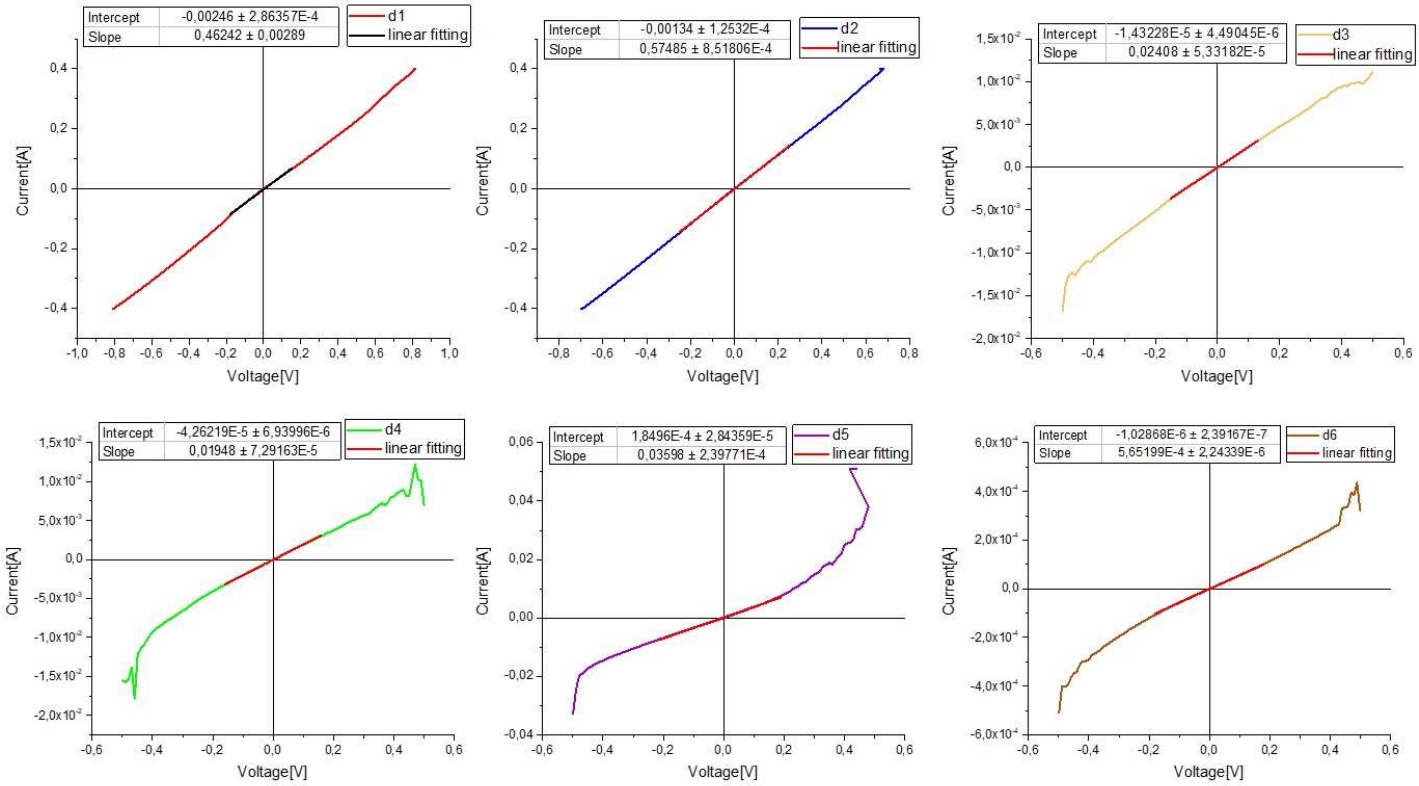

Fig.4.63. IV-curves of evaporated silver on the high doped GaAs wafer(Azur)

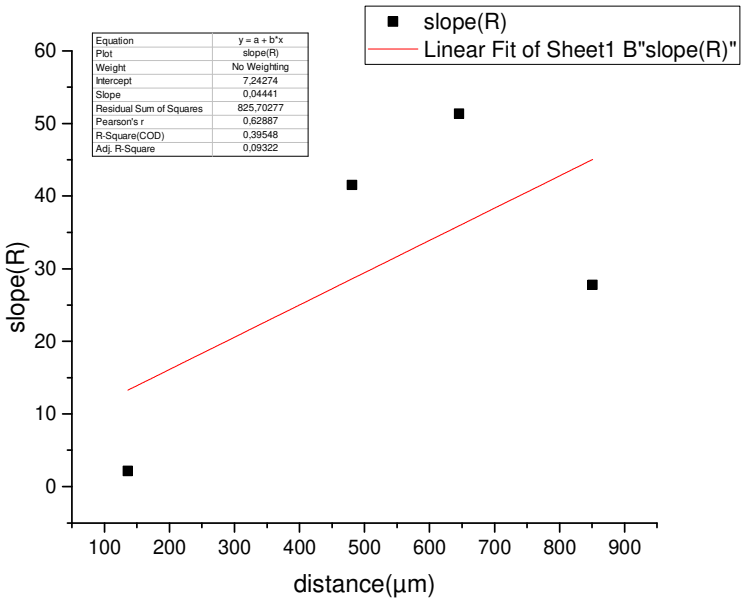

Fig.4.50. Fitting the plot of measured resistance versus distance of six devices on the high doped GaAs wafer (Azur)

Contact resistance (the Y-axis intercept/2): 3.62± 11.44 Ohm

Transfer length (the X-axis intercept/2): 81.5 µm

specific contact resistance(ρ_c) (resistivity): 45× 10^{-3} Ω cm^2

IV-curves of all devices on the low doped GaAs wafer (Freiberger) are shown in Fig.4.64. They tend to have a barrier in both directions, where in one direction it is higher than in the other.

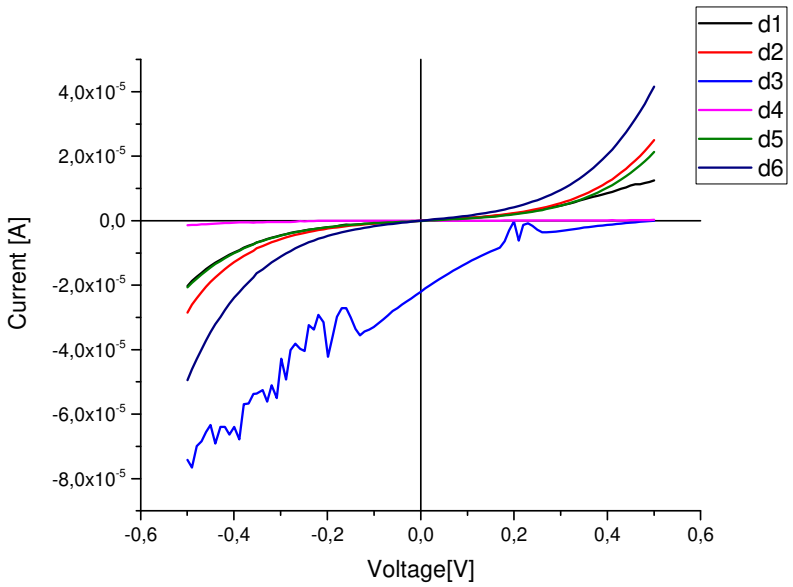

Fig.4.64. IV-curves of devices of evaporated silver on the low doped GaAs wafer (Freiberger)

Adhesion Test:

After applying sticky tape on the evaporated silver on both types of GaAs wafers and then pulling off, almost all the deposited thin films were removed from substrate easily.

Post Processing:

In order to further study of pure silver on the two types of wafers, the post processing was carried out. The post annealing was performed in several duration times, 15 min, 1-hour and 15-hours. For 15 min and 1-hour annealing, the samples were kept on hotplate at 280 °C in glovebox under Argon atmosphere, after that the hotplate was switched off and the samples were left for 5 min to cool down in glovebox to avoid the oxidization. For 15-hours annealing the samples were placed in the oven under vacuum.

Post Annealing for 15 Minutes:

Fig.4.65. illustrates, the thickness after 15 minutes annealing of both types of GaAs wafers. The variation of thickness by samples of deposited silver is much higher than one of deposited copper, especially on borders of devices.

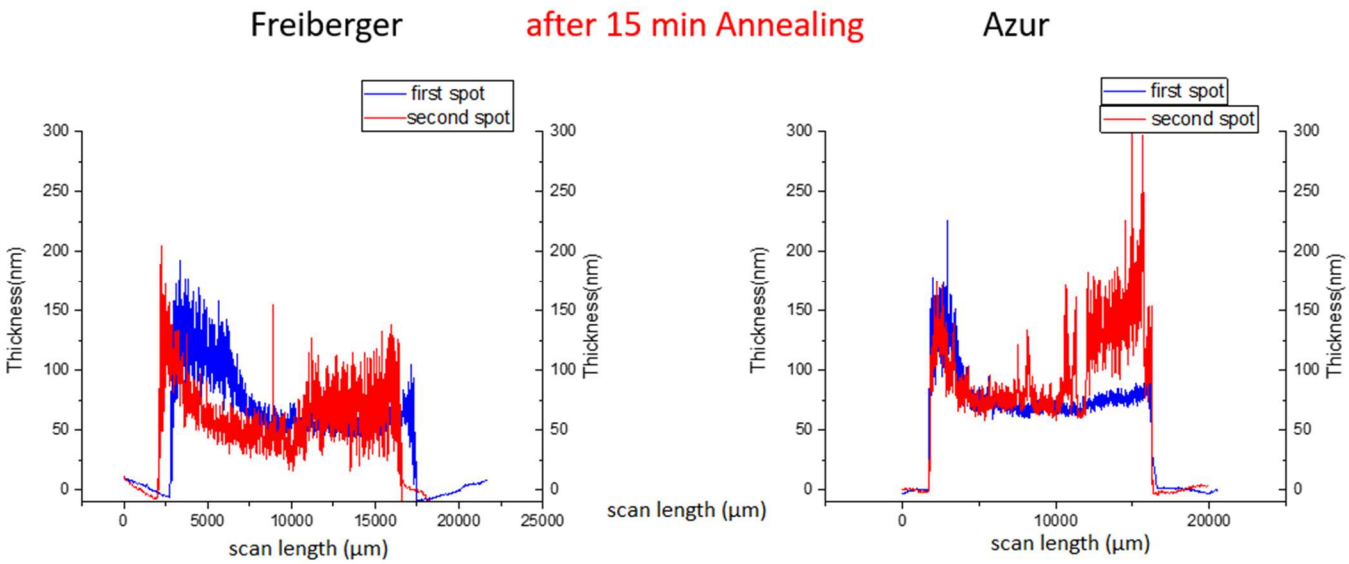

Fig.4.65. Thickness variation of evaporated silver on both type GaAs wafer after 15 min post annealing

Post annealing couldn't optimize electrical characteristic of Azur samples. As Fig.4.66. is shown, the current flow of devices became much lower than before annealing and three of devices don't have ohmic contact. Therefore, the acceptable accuracy in calculating the contact resistance of samples is hard. The contact resistance with considering only d1 and d2 is about 41.89 Ω and specific contact resistance(ρ_c) (resistivity): 122×10^{-3} Ω cm^2.

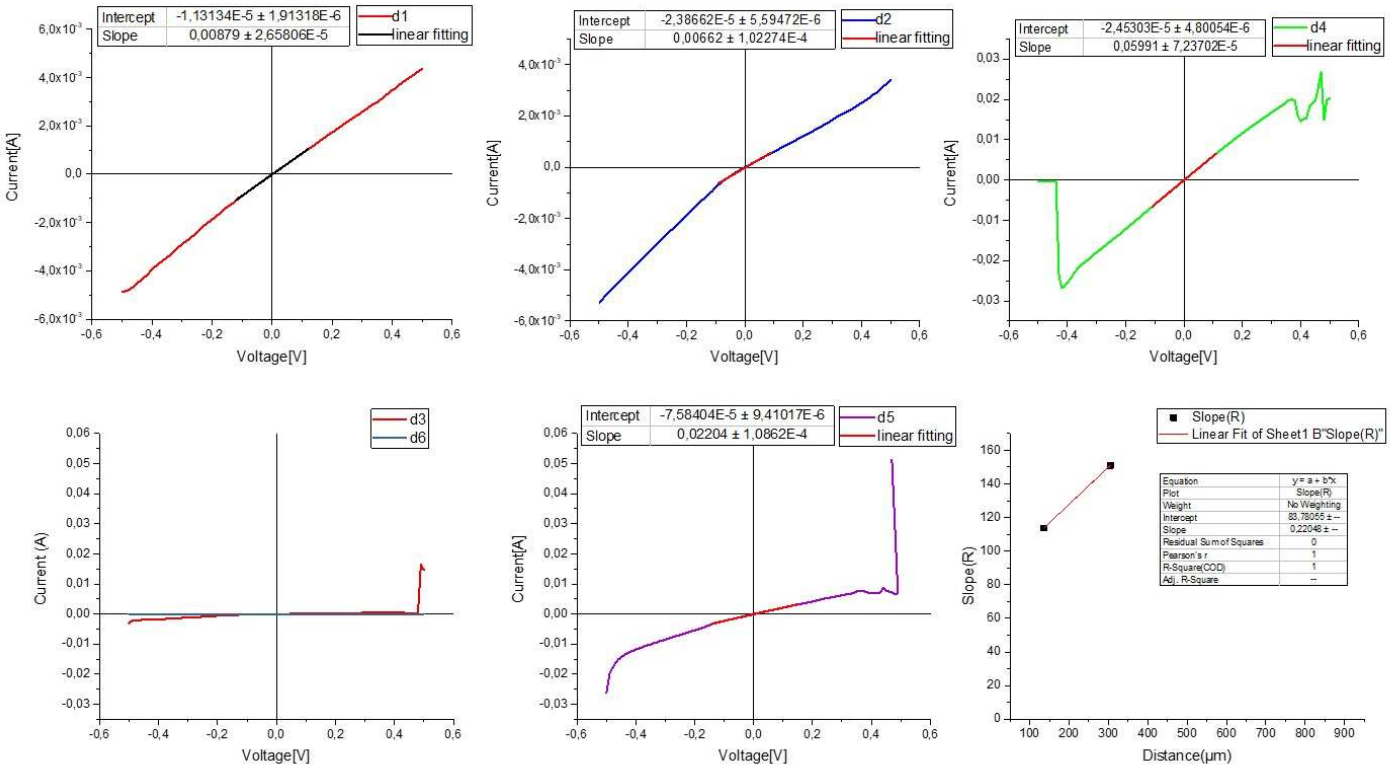

Fig.4.66. IV-curves of six devices of evaporated silver on the high doped wafer(Azur) after 15min post annealing

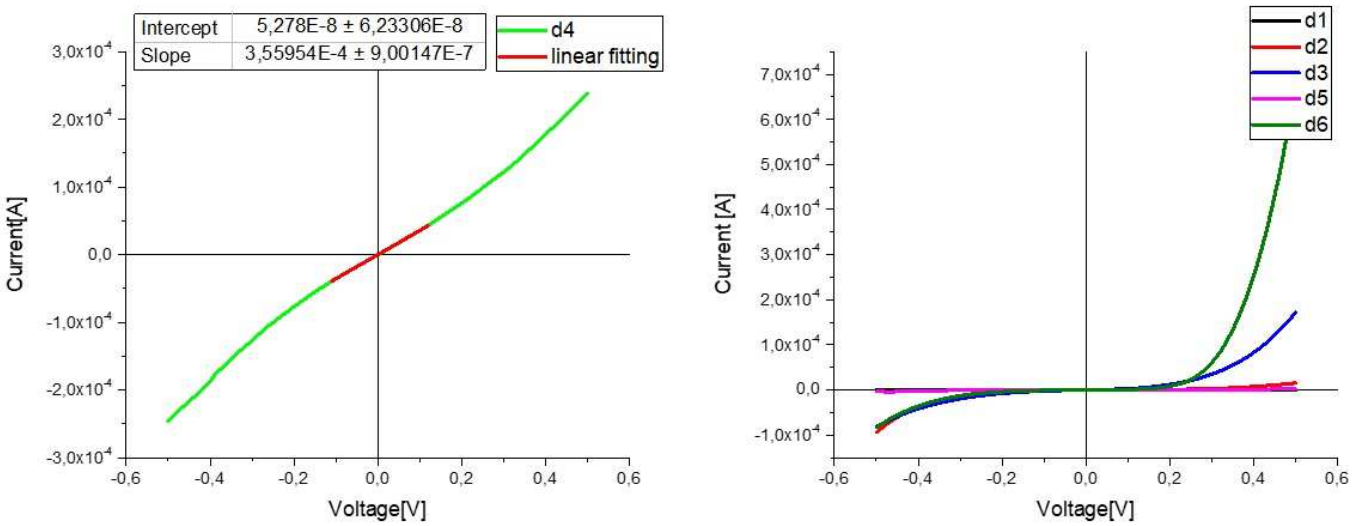

Fig.4.67. IV-curves of devices of evaporated silver on the low doped wafer(Freiberger) after 15min post annealing

Post annealing of samples with evaporated silver on Freiberger and Azur wafers couldn't improve the outcomes. The comparison of current flow in both types of wafers indicates that, the current in the low doped samples is ten times lower than ones in high doped samples. This hints at the difference of junction barrier of them.

the summary of result is listed in the tables below:

Azur	befor Annealing				
	ASH(nm)	Rq(nm)	contact type	RContact (Ω)	contact resistivity (Ω cm²)
	75.23	8.87	ohmic	3.62 ± 11.44	$45{,}3 \times 10^{-3}$
	after 15 min Annealing				
	ASH(nm)	Rq(nm)	contact type	RContact (Ω)	contact resistivity (Ω cm²)
	106.62	30.87	Almost ohmic	41.89 ± 0	122.49×10^{-3}

Freiberger	befor Annealing				
	ASH(nm)	Rq(nm)	contact type	RContact (Ω)	contact resistivity (Ω cm²)
	54.48	3.15	schottky	N	N
	after 15 min Annealing				
	ASH(nm)	Rq(nm)	contact type	RContact (Ω)	contact resistivity (Ω cm²)
	75.03	23.42	schottky	N	N

As mentioned previously, this experiment was repeated for second time and samples were annealed for 1 hour and 15 hours. The summary of results of electrical characteristic and the variation of thickness in second experiment are displayed below:

Azur					
	befor Annealing				
	ASH(nm)	Rq(nm)	contact type	RContact (Ω)	contact resistivity (Ω cm2)
	72	1,88	ohmic	3.47± 12.4	44.78×10^{-3}
	after 1 hour Annealing				
	ASH(nm)	Rq(nm)	contact type	RContact (Ω)	contact resistivity (Ω cm2)
	41,91	2,63	ohmic	3,85±2,68	46.4×10^{-3}
	after 15 hours Annealing				
	ASH(nm)	Rq(nm)	contact type	RContact (Ω)	contact resistivity (Ω cm2)
	148,5	30,05	schottky	N	N

Freiberger					
	befor Annealing				
	ASH(nm)	Rq(nm)	contact type	RContact (Ω)	contact resistivity (Ω cm²)
	62,27	1,88	schottky	N	N
	after 1 hour Annealing				
	ASH(nm)	Rq(nm)	contact type	RContact (Ω)	contact resistivity (Ω cm²)
	44,04	68.57	schottky	N	N
	after 15 hours Annealing				
	ASH(nm)	Rq(nm)	contact type	RContact (Ω)	contact resistivity (Ω cm²)
	139,88	154.88	schottky	N	N

From the gathered data of all samples before and after post annealing, it could be said, that the lowest contact resistance between pure silver and high doped GaAs wafer was gained without post-annealing, however it is still higher than intended contact resistance (smaller than 1Ω). Since the results were obtained with minimum points, the results might be not trustable and the measurements should be repeated.

The samples of the low doped wafer didn't have any ohmic contact before and after post annealing. It might be due to higher junction barrier between silver and GaAs. In addition, the post annealing doesn't seem to improve the contact resistance in this experiment.

Fig.4.68. represents the thickness of second experiment before and after annealing. After annealing, the reaction of silver thin film with both types of wafers was very intense especially on borders, so that the thickness of borders has been increased to more than 200 nm.

Also the colour of silver was changed by further annealing to 15 hours.

To study the effect of post annealing on silver thin film structure, the morphology images and phase mapping were utilized. The variation of thickness was measured to compare and to obtain more accurate analysis of results.

As illustrated in Fig.4.69.and Fig.4.70., after annealing were produced some agglomerated parts and by more annealing these became more and thicker especially on borders (see the SEM images). As indicated in section image, the thickness of thin films on agglomerated parts was varied sometimes to about 300nm. It could be referring to diffusion of silver in GaAs crystal and make a new phase of Ag-Ga-As.

In general, after the post annealing the reaction of silver with GaAs (both types of wafer) is much more in comparison to copper.

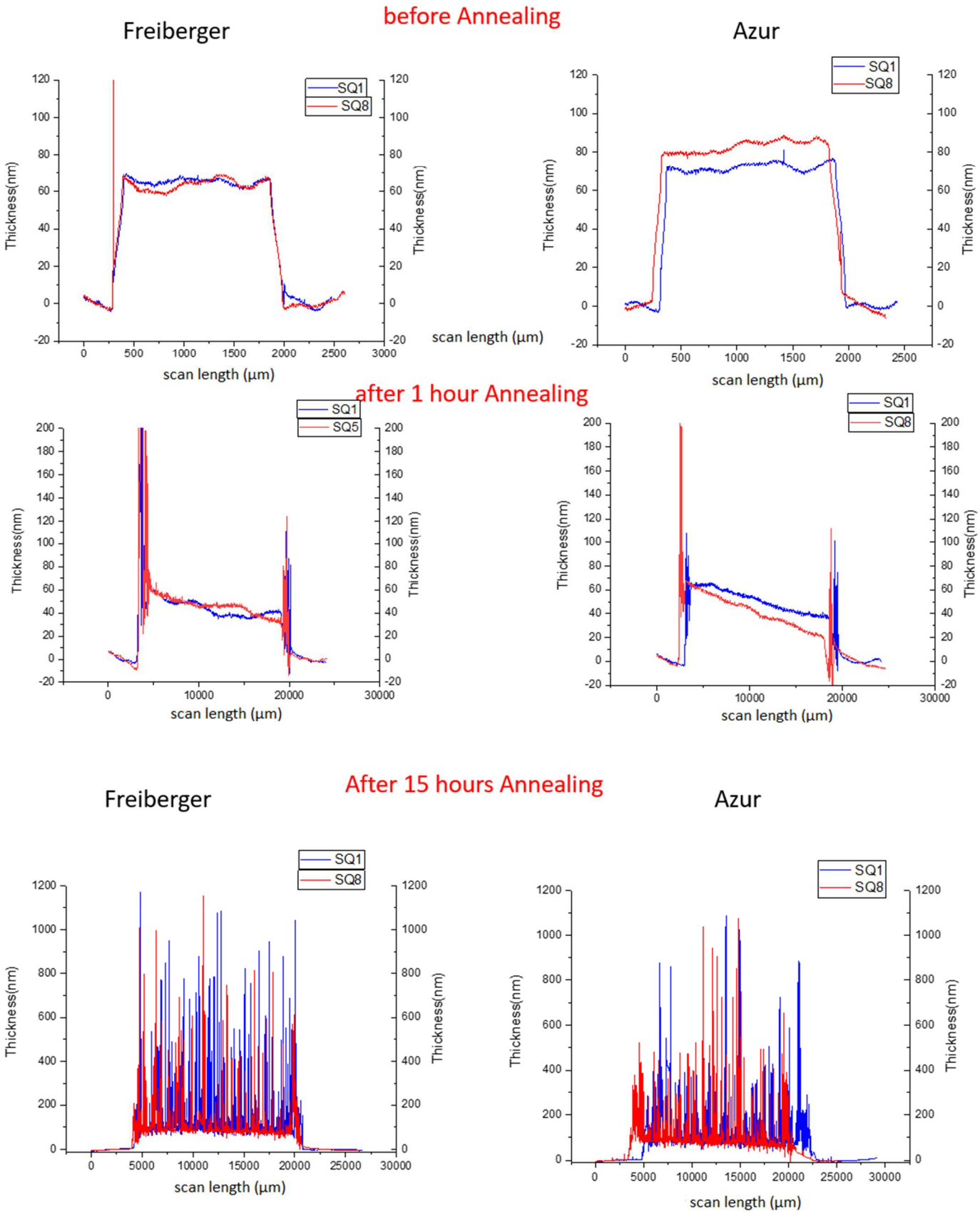

Fig.4.68. Variation of thickness of silver thin film before and after post annealing for 1 and 15 hours

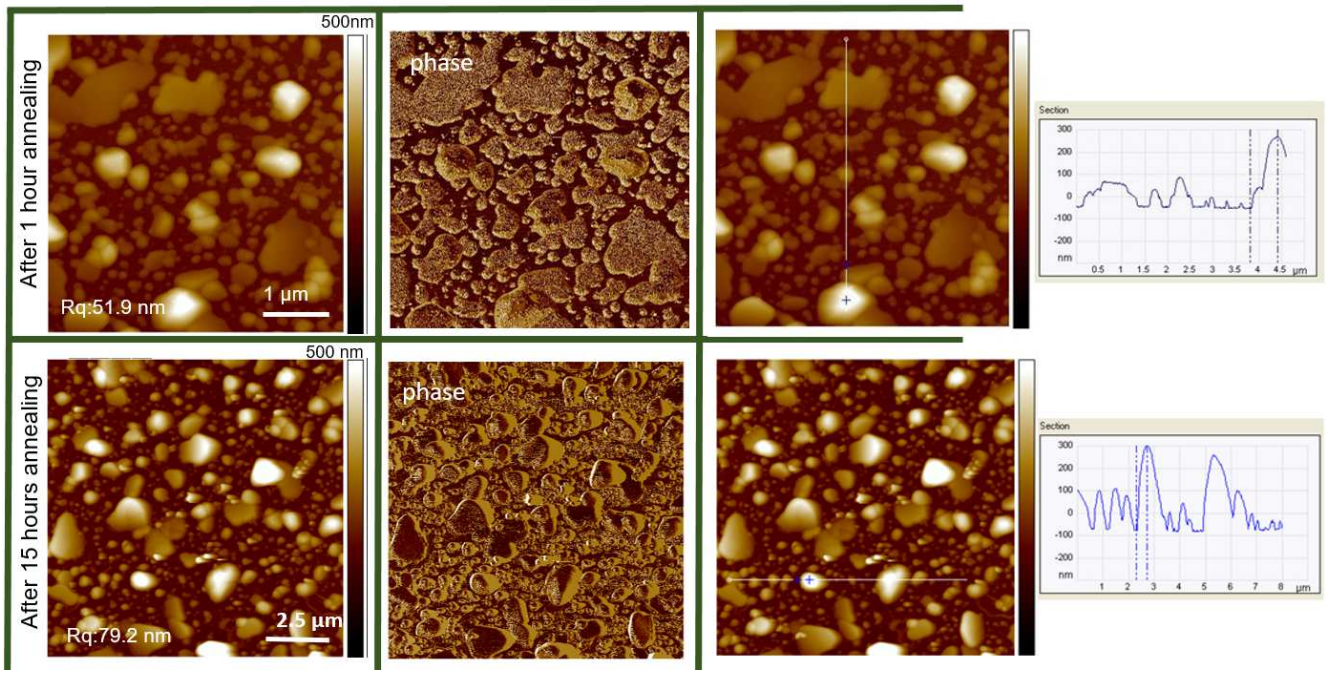

Fig.4.69. Morphological characterization of deposited silver on high doped GaAs wafer (Azur).

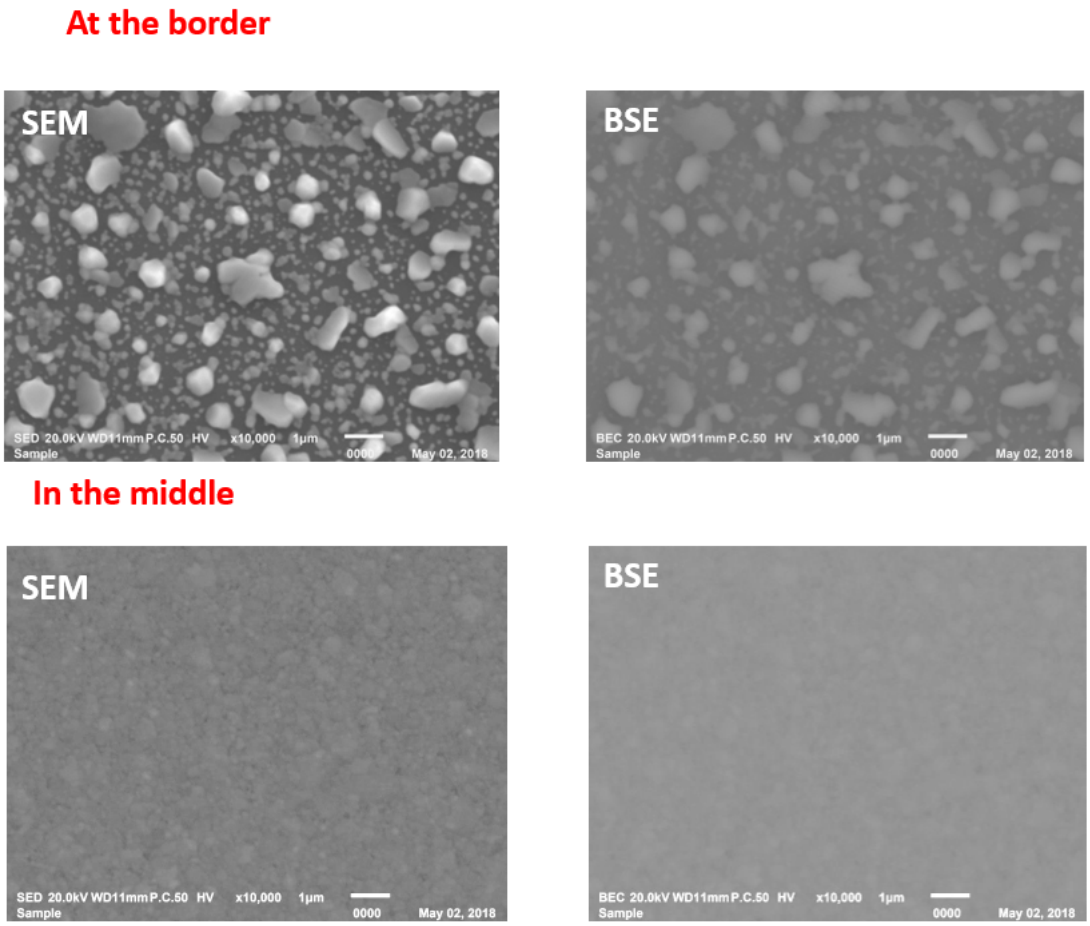

Fig.4.70. SEM and BSE images at the border and in the middle of samples on the high doped wafer (Azur)

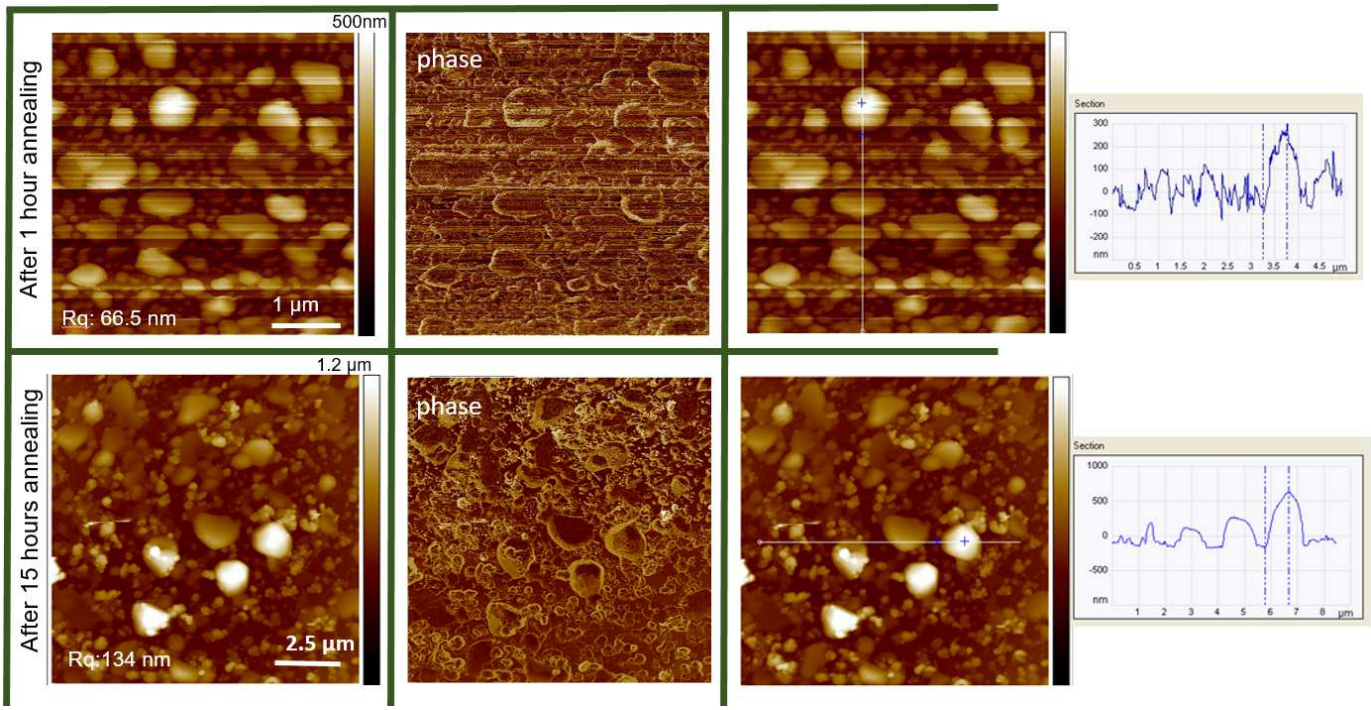

Fig.4.71. Morphological characterization of deposited silver on the low doped GaAs wafer (Freiberger).

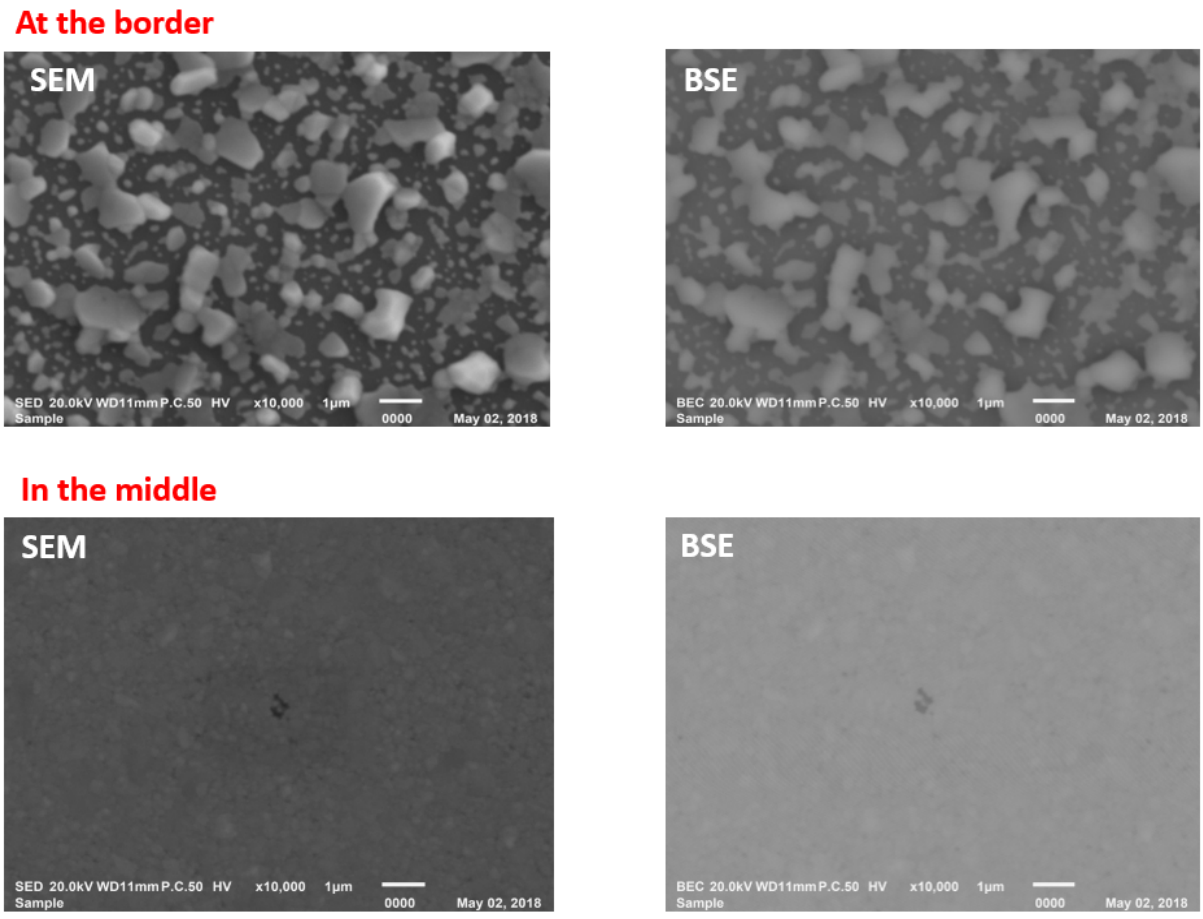

Fig.4.72. SEM and BSE images at the border and in the middle of samples on low doped wafer (Freiberger)

5. Summary

This work focuses on the optimization of the front contact grid on III-V/Si tandem solar cells by low cost process. To accomplish this, the printing process of Inkjet printing and spin-coating were presented and also the laser sintering process of commercial copper NPs ink by using pulsed pico-second Nd-YAG laser was reported. A comprehensive investigation was carried out for finding the best laser parameter windows on different substrates to gain the lowest contact resistance and consequently lowest resistivity between the metal and the semiconductor.

The variation of resistance with different thickness of printed copper NPs layers, exposure time and different parameters of the laser was studied. This study indicated that, a higher thickness of printed copper NPs enabled to obtain a lower contact resistance in terms of more conductive material but the adhesion of the sintered film became weaker and vice a versa.

Moreover, the contact resistance of sintered copper and the effect of the laser sintering conditions was compared and discussed. The sintering process under higher laser power with higher exposure time (lower scan speed) decreased the resistivity and caused superior outcomes. Sintering with more over scans didn't improve the results obviously and eventually, the resistivity of sintered copper varied slightly by variation of lateral distance of the scan lines of the laser. Also using another atmosphere in the sintering process couldn't influence dramatically the resistivity, however by applying an argon atmosphere better results were gained in comparison to nitrogen.

This survey demonstrated that, although the sintering via laser can provide high resolution patterns practically but the quality of sintering dramatically depended on the uniformity of the printed layer. On non-uniformly printed layers, the pulsed laser couldn't prepare a good quality of sintering across the sintering area. Post-annealing of sintered structures could modify their electrical properties and adhesion faintly.

The samples, which were printed by Inkjet printer resulted in non-homogeneous thickness and affected significantly the sintering quality, as the laser didn't have the same effect on the whole printed area, while on samples, which were printed by spin-coating and thus had more homogenous thickness, the laser provided better sintering quality. Therefore, spin-coating improved the uniformity of the thin film's thickness and adhesion of sintered copper NPs but enhanced the resistance due to the thinner deposited layer or lower conductive NPs. Also it was found that, in a thin coated layer, the dispersion of copper NPs on the substrate is non-homogeneous in terms of low copper NPs content in this type of ink.

In addition, this work provided depositing the pure copper and silver with about 100nm thickness on two types of GaAs wafers by EBPVD method to prove the possibility of ohmic contact and low contact resistance on GaAs wafers. The lowest contact resistance was achieved between pure deposited copper and high doped GaAs (Azur) without post annealing.

Post annealing was performed to investigate whether the contact resistance between metal and GaAs could be reduced. The post annealing couldn't improve the resistivity of samples on high doped GaAs (copper and silver). The samples of deposited copper and silver on the low doped GaAs didn't have any ohmic IV-curves before annealing, but by post-annealing for 1-hour just the results of deposited copper samples could be optimized, however these were higher than the expected result.

Finally, from the gathered data for all samples before and after post annealing, it is obvious that the copper seems to be a better candidate for these types of GaAs wafers to gain ohmic contact with low resistivity. The lowest contact resistivity of pure copper on highly doped GaAs was found to be 1.2×10^{-2} Ohm.cm^2, while for pure silver only 4.5×10^{-2} Ohm.cm^2 was obtained.

References

[1] A. James, "Global market Outlook for solar cell 2017-2021", https://irishsolarenergy.org/news-docs/GMO_2017.pdf, Downloaded on 11. 09.2018.

[2] N. Lewis and G. Crabtree (eds.), "Basic Research Needs for Solar Energy Utilization", report on the Basic Energy Sciences Workshop on Solar Energy Utilization, (18.04.2005), https://www.osti.gov/servlets/purl/899136, Downloaded on 11. 09.2018.

[3] L. Frantzis, E. Jones, C. Lee, M. Wood, and P. Wormser, "Opportunities for cost reductions in photovoltaic modules", in Proceedings of the 16th European Photovoltaic Solar Energy conference, Glasgow, UK, pp. 2100- 2103 (2000), https://www.researchgate.net/.../228969634, Downloaded on 17. 09.2018.

[4] Abasifreke Ebong, Senior Member, IEEE, and Nian Chen, " Metallization of crystalline silicon solar cells",https://ieeexplore.ieee.org/iel5/6410664/6421421/06421444.pdf, " Downloaded on 13. 03 2018.

[5] Nelson, J. "The Physics of Solar Cells", Imperial College Press, WC2H 9HE, U.K., 2003, 363 pages, ISBN: 1860943497, 1860943403.

[6] Ansgar Mette, Dissertation Thesis, " New Concepts for Front Side Metallization of Industrial Silicon Solar Cells " Albert-Ludwigs-University, Freiburg in Breisgau, Germany (2004), https://www.freidok.uni-freiburg.de/fedora/objects/freidok:3782/datastreams/, Downloaded on 23. 07 2018.

[7] "Photovoltaic System in Progress: A Survey of Recent Development". Pdf article, https://www.researchgate.net/publication/265692927_Photovoltaic_System_in_Progress_A_Survey_of_Recent_Development, Downloaded on 15. 10.2018

[8] Solarpraxis AG , "Engineering the Solar Age: Suppliers for Photovoltaics", pp. 18–25, Report, (2012–2013).http://www.suppliers-pv.com/fileadmin/userupload/2012/pdf/esa1GW-ES-Screen.pdf , Downloaded on 12.6.2018

[9] Edited by Carlos Algora, Ignacio Rey-Stolle, " Handbook of concentrator photovoltaic technology", DOI:10.1002/9781118755655, 2016

[10] Shockley, W. and Queisser, H.J. (1961) "Detailed balance limit of efficiency of p-n junction solar cells". Journal of Applied Physics, 32, 510–519. doi: 10.1063/1.1736034, Downloaded on 21.10.2018

[11] J.N.Roy, D.N.Bose, "Photovoltaic Science and Technology", Cambridge university press, 2018. https://doi.org/10.1017/9781108231718.

[12] A. Willoughby, P. Capper, S. Kasap, "Solar Cell Materials, Developing Technologies", Wiley press, ISBN-13: 978-0470065518, 2014

[13] Hector Cotal, Chris Fetzer, Joseph Boisvert, Geoffrey Kinsey, Richard King, Peter Hebert, Hojun Yoon and Nasser Karam, "III–V multijunction solar cells for concentrating photovoltaics", Published on 10 December 2008. DOI:10.1039/B809257E, Downloaded on 19/10/2017

[14] G. Segev, G. Mittelman, A. Kribus, "Equivalent circuit models for triple-junction concentrator solar cells", Solar Energy Materials & Solar Cells 98, 2012, DOI: 10.1016/j.solmat.2011.10.013, Downloaded on 9/10/2017

[15] Ya-Ju Lee, Yung-Chi Yao, Meng-Tsan Tsai, An-Fan Liu, Min-De Yang, and Jiun- Tsuen Lai, "Current matching using CdSe quantum dots to enhance the power conversion efficiency of InGaP/GaAs/Ge tandem solar cells", 2013, https://www.ncbi.nlm.nih.gov/pubmed/24514936 Downloaded on 11/10/2017

[16] Karen Derendorf, Stephanie Essig, Eduard Oliva, Vera Klinger, Tobias Roesener, Simon P. Philipps, Jan Benick, Martin Hermle, Michael Schachtner, Gerald Siefer, Wolfgang J¨ager, and Frank Dimroth, "Fabrication of GaInP/GaAs//Si Solar Cells by Surface Activated Direct Wafer Bonding", 2013, DOI: 10.1109/JPHOTOV.2013.2273097, Downloaded on 18/03/2018

[17] Romain Cariou, Jan Benick, Paul Beutel, Nasser Razek, Christoph Fl¨otgen, Martin Hermle, David Lackner, Stefan W. Glunz, Senior Member, IEEE, Andreas W. Bett, Member, IEEE, Markus Wimplinger, and Frank Dimroth, Member, IEEE, Monolithic "Two-Terminal III–V//Si Triple-Junction Solar Cells with 30.2% Efficiency Under 1-Sun AM1.5g", 2017, DOI: 10.1109/JPHOTOV.2016.2629840, Downloaded on 11/10/2018.

[18] J. R. Lang, J. Faucher, S. Tomasulo,K.N.Yaung, andM. L. Lee, "Comparison of GaAsP solar cells on GaP and GaP/Si", 2013, https://doi.org/10.1063/1.4959825, Downloaded on 18/10/2018.

[19] S. M. Sze, "Physics of Semiconductor Devices", 2nd ed., John Wiley & Sons press, New York (1981), ISBN: 978-0-471-14323-9.

[20] "Challenge of Applying Ohmic Contacts to Gallium Arsenide Devices", https://materion.com/-/media/files/.../me/challenge-of-applying-ohmic-contacts.pdf, Downloaded on 18/01/2018

[21] O. Pritchard and A. Skinner "The concept of electronegativity", 1954, DOI: 10.1021/cr50004a005, Downloaded on 30/10/2018.

[22] S. Magdassi, A. Kamyshny, "Nanomaterials for 2D and 3D Printing", Wiley press, 2017, DOI:10.1002/9783527685790

[23] M. Grouchko, A. Kamyshny, S. Magdassi," Formation of air-stable copper-silver core-shell nanoparticles for inkjet printing ", 2009, DOI:10.1039/B821327E, Downloaded on 28/04/2018

[24] Hans J. Scheel, Peter Capper, "Crystal Growth Technology: From Fundamentals and Simulation to Large-scale Production", 2011, DOI:10.1002/9783527623440, Downloaded on 28/04/2018

[25] https://freiberger.com/en/technology/#crystal-growth, Downloaded on 28/01/2018

[26] https://www.alineason.com/en/knowhow/crystal-growth/, Downloaded on 13/10/2018

[27] http://www.str-soft.com/products/CGSim/VGF_growth_of_GaAs/index.htm, Downloaded on 28/04/2018

[28] M. Y. Ghannam, J. Poortmans, and J. F. Nijs, "Quantitative comparison between the performance of buried contact and of screenprinted contact industrial silicon solar cells", Kuwait Journal of Science and Engineering, 1998, https://www.researchgate.net/.../263455092 Downloaded on 19/11/2018

[29] A.Kamyshny, S.Magdassi, "Conductive nanomaterials for printed electronics", Wiley press , , DOI: 10.1002/smll.201303000, 2014, Downloaded on 17/8/2018

[30] A. Lee, K. Sudau, K. Hyun Ahn, S. Jong Lee, N. Willenbacher, "Optimization of Experimental Parameters to Suppress Nozzle Clogging in Inkjet Printing", 2012, DOI: 10.1021/ie301403g, Downloaded on 18/2/2018.

[31] John C. Miers, Wenchao Zhou, "Inkjet Printing at Megahertz Frequency",2015,

sffsymposium.engr.utexas.edu/sites/default/files/2015/2015-103-Miers.pdf, Downloaded on 18/2/2018.

[32] S. Jung, "Fluid characterisation and drop impact in inkjet printing for organic semiconductor devices", 2014, https://doi.org/10.17863/CAM.14014, Downloaded on 21/5/2018.

[33] https://www.ossila.com/pages/spin-coating, Downloaded on 21/09/2018

[34] Yan Zhang, David Christopher Whalley, "Influence of etching solvent evaporation on the size of micro-via holes in PVP thin films", 2012, https://www.researchgate.net/.../272819477, Downloaded on 05/09/2018.

[35] http://hivatec.ca/consulting-design/thin-film-deposition/, Downloaded on 15/08/2018.

[36] M. Zenou1, O. Ermak, A. Saar, and Z Kotler, "Laser sintering of copper nanoparticles", 2014, https://www.researchgate.net/.../262986740 , Downloaded on 18/09/2018.

[37] http://www.amadamiyachi.com/glossary/glosspulserepetitionrate, Downloaded on 18/09/2018.

[38] https://www.news-medical.net/life-sciences/What-is-Optical-Microscopy.aspx, Downloaded on 18/09/2018.

[39] https://www.nanoscience.com/techniques/optical-profilometry/ ,Downloaded on 18/09/2018.

[40]https://www.nanoscience.com/techniques/atomic-force-microscopy/

[41] Daniel Abou-Ras, Thomas Kirchartz, Uwe Rau, "Advanced Characterization Techniques for Thin Film Solar Cells", Wiley press, 2016, DOI:10.1002/9783527699025

[42] https://www.mdpi.com/1424-8220/17/4/938

[43] http://confocal-manawatu.pbworks.com/w/page/34607861/Force%20Curve%20AFM

[44] James Seyforth, " Scanning Electron Microscopy (SEM): An Introduction to the use of SEM for character- ising the Surface Topology and Composition of Matter with Further Applications " ,2015, https://www.researchgate.net/.../304247407 , Downloaded on 18/2/2018.

[45] B.J.Inkson, "Scanning electron microscopy (SEM) and transmission electron microscopy (TEM) for materials characterization", 2016, https://doi.org/10.1016/B978-0-08-100040-3.00002-X , Downloaded on 18/2/2018.

[46] https://www.nanoscience.com/techniques/scanning-electron-microscopy/

[47] https://www.ossila.com/pages/sheet-resistance-measurements-thin-films

[48] Freedman, "Contact resistance and TLM measurements",

tuttle.merc.iastate.edu/ee432/topics/metals/tlm_measurements.pdf , Downloaded on 18/12/2017.

symbol	description	unit
I_{sc}	short circuit current	A
V_{oc}	open circuit voltage	V
$I_{sc,l}$	short circuit current of low band gap	A
$I_{sc,h}$	short circuit current of high band gap	A
$E_{g\ window}$	energy band gap of window layer	eV
$E_{g\ emitter}$	energy band gap of emitter layer	eV
k_B	Boltzmann's constant (1.38×10^{-23})	J/K
T	absolute temperature	°C or K
A	area	cm^2
q	elementary charge	C
J_{sc}	short circuit current density	$A\ m^{-2}$
J_0	saturation current density	$A\ m^{-2}$
J_L	load current density	$A\ m^{-2}$
Rs	series resistances	Ω
Rsh	shunt resistances	Ω
E_g	energy band gap	eV
Jm	current density at the maximum power point	$A\ m^{-2}$
R_{Sem}	Resistance in the semiconductor layers	Ω
R_c	Contact resistance	Ω
R_m	metal Resistance	Ω
V_{bi}	built-in potential	V
Φ_B	potential barrier to n-doped semiconductor	
Φ_M	potential barrier of metal	
χ_s	electron affinity	eV
P *AVG*	average power	W
F *REP*	repetition frequency	Hz
E *PULSE*	Pulse Energy	J
R_s	sheet resistance	Ω/□
ρ	resistivity	Ω.cm²
t	thickness	m
L_1	smallest distance between fingers	m
W	Effective length	m
λ	wavelength	m
ASH	average step height	m

acronym	description
PV	Photovoltaic
EBPVD	E-beam physical vapour deposition
CPV	concentrating photovoltaics
MOVPE	metal organic vapour phase epitaxy
BSF	back surface field
MPP	maximum power point
MJSC	multijunction solar cells
TFE	thermionic field emission
TE	thermionic emission
FE	Field Emission
M-S	metal -semiconductor
PVD	physical vapour deposition
NPs	nanoparticles
LEC	Liquid Encapsulated Czochralski
VGF	Vertical Gradient Freeze
pBN	pyrolytic boron nitride
IJP	Ink-jet printing
PIJ	piezoelectric inkjet
PRR	Pulse Repetition Rate
SFD	seeder frequency divider mode
PPD	Pulse to Pulse Distance
AFM	Atomic Force Microscopy
SEM	Sample-Electron Interaction
BSE	backscattered electrons
EBSD	electron backscatter diffraction
CL	cathode-luminescence
CI	commercial ink
TLM	transmission line measurement